University of Nevada, Reno

Cloud Dynamics and Microphysics during CAMPS: A Comparison between Airborne and Mountaintop Cloud Microphysics

A thesis submitted in partial fulfillment of the
requirements for the degree of Master of Science in
Atmospheric Science

by

Robert O. David

Dr. Douglas H. Lowenthal/Thesis Advisor

May, 2015

THE GRADUATE SCHOOL

We recommend that the thesis
prepared under our supervision by

ROBERT O. DAVID

Entitled

Cloud Dynamics and Microphysics during CAMPS: A Comparison between Airborne and Mountaintop Cloud Microphysics

be accepted in partial fulfillment of the
requirements for the degree of

MASTER OF SCIENCE

Douglas H. Lowenthal, Ph.D., Advisor

A. Gannet Hallar, Ph.D., Committee Member

Mike L. Kaplan, Ph.D., Committee Member

Daniel C. Obrist, Ph.D, Graduate School Representative

David W. Zeh, Ph. D., Dean, Graduate School

May, 2015

Abstract:

Orographically-enhanced clouds are essential for global hydrological cycles. To better understand the structure and microphysics of orographically-enhanced clouds, an airborne study, the Colorado Airborne Mixed-Phase Cloud Study (CAMPS), and a ground-based field campaign, the Storm Peak Lab (SPL) Cloud Property Validation Experiment (StormVEx) were conducted in the Park Range of the Colorado Rockies. The CAMPS study utilized the University of Wyoming King Air (UWKA) to provide airborne cloud microphysical and meteorological data on 29 flights totaling 98 flight hours over the Park Range from December 15, 2010 to February 28, 2011. The UWKA was equipped with instruments that measured cloud droplet and ice crystal size distributions, liquid water content, and 3-dimensional wind speed and direction. The Wyoming Cloud Radar and LiDAR were also deployed during the campaign. These measurements are used to characterize cloud structure upwind and above the Park Range. StormVEx measured temperature and cloud droplet and ice crystal size distributions at SPL. The observations from SPL are used to determine mountain top cloud microphysical properties at elevations lower than the UWKA was able to sample *in-situ*. To assess terrain flow effects on cloud microphysics and structure, vertical profiles of temperature, humidity and wind were obtained from balloon borne soundings and verified with high resolution modeling. Comparisons showed that cloud microphysics aloft and at the surface were consistent with respect to snow growth processes and previous studies on terrain flow effects. Small ice crystal concentrations were routinely higher at the surface and a relationship between small ice crystal concentrations, large cloud droplet concentrations and temperature was observed, suggesting liquid-dependent ice nucleation near cloud base.

Acknowledgements:

I would first like to acknowledge my advisor, Doug Lowenthal, for all of his time, support, patience and guidance during the past two years. Without his help, my achievement of this advanced degree would not have been possible. I would also like to thank my committee members, Gannet Hallar, Mike Kaplan and Daniel Obrist for all of their insightful knowledge and support while researching and writing. I would also like to thank my family and friends for their support over the past two years. This research was made possible by funding provided by National Science Foundation grants AGS-0964811 and AGS-1260462. Data for this research was obtained from the Atmospheric Radiation Measurement (ARM) Program sponsored by the U.S. Department of Energy, Office of Science, Office of Biological and Environmental Research, Climate and Environmental Sciences Division. Research was carried out at the Desert Research Institute, Storm Peak Lab and the University of Nevada Reno.

Table of Contents

List of Figures

Chapter 1: Introduction

Mountain based snowfall is essential for hydrological cycles globally (Smith et al. 2005) and provides water to 60 million people in the Western U.S. (Barnett et al. 2005; Bales et al. 2006). The Colorado River, whose headwaters and tributaries originate as high elevation snowfall, helps irrigate 5.7 million acres of land across seven states (Cohen et al., 2013) at an annual worth of 1.41 trillion dollars (James et al., 2014). Due to the importance of municipal water supplies and the economic value of irrigation across the Western U.S. alone, understanding and forecasting precipitation amounts and distributions in complex terrain is essential. In the last 30 years, several studies have focused on furthering the knowledge of mountain-based precipitation (orographic precipitation) mechanisms, such as latent heat release (heat released during the phase change of water) on the windward slope (e.g., Hill, 1983; Pandley et al., 1999; Doyle and Smith, 2003; Jiang, 2003; Zängl, 2007, Kaplan et al., 2012), upstream static instability and flow blocking (e.g., Grosman and Durran, 1984; Sinclair et al., 1997; Colle, 2004; Rotunno and Houze, 2007) and microphysical processes (e.g., Bergeron, 1965; Browning, 1980; Borys et al., 2003; Rosenfeld and Givati, 2006; Lowenthal et al., 2011; Saleeby et al., 2012). The culmination of many of these studies is the importance of cross-mountain wind speed, upstream static stability, barrier shape and height and freezing level on orographic precipitation distribution (e.g, Sinclair et al., 1997; Jiang, 2003; Colle, 2004; Zängl, 2007; Rotunno and Houze, 2007).

Sinclair et al. (1997) found that precipitation distribution increased on the leeward slope (spillover) when cross-barrier wind speed increased and upwind stability decreased. The changes in stability and wind speed explained up to 93% of the observed spillover variations during a major storm in the Southern Alps. Jiang (2003) showed that latent heat release on the windward slope can double the height at which low level air is lifted over a mountain barrier compared to that of dry air and that

warmer upstream surface air delayed flow splitting, blocking and mountain wave breaking. Several modeling sensitivity tests done by Colle (2004) showed that increasing cross-mountain wind speed for narrow mountain barriers and reducing static stability increased the spillover and lowered the precipitation efficiency (the difference between precipitation aloft and precipitation that reaches the ground) on the windward slope to below 60%. Further, sensitivity tests showed that lower freezing levels allowed for stronger winds to advect frozen hydrometeors farther onto the leeward slope of the mountain. Zängl (2007) and Rotunno and Houze (2007) showed that upwind latent heat release played a major role in orographic blocking and precipitation distribution during the Mesoscale Alpine Programme in the Alps. The moist nondimensional mountain height number (M_m) has been used as an objective measure of the likelihood of precipitation around and over a mountain barrier in several studies and combines upwind static stability, barrier height and cross mountain wind speed (e.g., Sinclair et al., 1997; Jiang, 2003; Colle, 2004). It is defined as:

$$\mathbf{M_m = N_m h_m / U} \qquad \mathbf{(1)}$$

or the inverse Froude number, where N_m is the moist Brunt-Vaisala Frequency, a measure of stability (Durran and Klemp, 1982; Barcilon and Fitzjarald, 1985), h_m is the maximum mountain height and U is cross-mountain wind speed.

In addition to the dynamical processes mentioned above, aerosols and microphysical properties have been shown to alter precipitation formation and distribution over complex terrain (e.g., Pruppacher and Klett, 1997; Borys et al., 2003; Rosenfeld and Givati, 2006; Lowenthal et al., 2011; Saleeby et al., 2012). Higher concentrations of cloud condensation nuclei (CCN) produce more numerous but smaller cloud droplets (Twomey et al., 1984; Peng et al., 2002; Lowenthal et al., 2002). As cloud droplet size decreases below around 10 µm, riming efficiency approaches zero due to aerodynamic

effects (Pruppacher and Klett, 1997). Decreasing riming efficiency has been observed to decrease precipitation efficiency on the windward slope (Borys et al., 2000, 2003) and has been shown to redistribute precipitation over mountain barriers in modeling studies (Saleeby et al., 2009,2012). Secondary ice formation processes such as rime-splintering (Hallett-Mossop Process) and free falling droplet freezing are also related to droplet size. The Hallett-Mossop Process occurs when cloud droplets larger than 16 μm (preferably around 24 μm) rime and splinter as they freeze symmetrically inwards when temperatures range between -3 and -8^{o}C (e.g. Hallett and Mossop,1974; Mossop, 1985). The ice splinters can continue to grow rapidly through vapor deposition. Free falling droplets larger than 50 μm have also been observed to shatter during the freezing process (e.g. Pruppacher and Klett, 1997; Rangno and Hobbs, 2001). Several studies have shown a link between cloud droplet size and ice particle concentrations under and outside of secondary ice formation conditions (e.g. Hobbs and Rangno, 1985; Rangno and Hobbs, 2001; Ansmann et al., 2009; Lance et al. 2011; de Boer et al., 2011). Hobbs and Rangno (1985) found a strong relationship between the width of cloud droplet spectra and ice particle concentrations in both cumuliform and stratiform type clouds where cloud top temperature ranged between -36 and -6^{o}C. Similar results were observed in mixed-phase clouds in the Arctic by Rangno and Hobbs (2001). Lance et al. (2011) found higher ice crystal concentrations in cleaner Arctic clouds with larger drop sizes than in polluted Arctic clouds with smaller, more numerous drops. These results suggested that the width of the cloud droplet spectra in Arctic clouds may be more important for ice production than the concentration of ice nuclei (IN). In mixed-phase clouds, a small fraction of aerosols can act as heterogeneous IN and produce ice through four known freezing modes: deposition, immersion, condensation, and contact freezing (e.g. Ladino et al., 2013). Deposition freezing occurs when water vapor deposits directly onto an IN and generally occurs at temperatures below other heterogeneous freezing modes (Lohmann and Diehl, 2006). Contact freezing occurs when an IN comes into contact with a supercooled cloud droplet and initiates freezing. Contact freezing is the most

efficient freezing mechanism in slightly supercooled environments (e.g. Lohmann and Diehl, 2006). Immersion freezing and condensation freezing are much more difficult to differentiate. Immersion freezing occurs when a supercooled cloud droplet nucleates and grows on an IN and then freezes once a certain temperature threshold is met. Meanwhile, condensation freezing occurs when water vapor condenses onto an IN and forms a haze a droplet that then nucleates into ice. However, recent work in Arctic mixed-phase clouds showed that ice was observed only after a liquid cloud layer had developed and found no evidence of condensation freezing (de Boer et al. 2011).

The majority of microphysical studies on ice nucleation have been based on chamber and laboratory experiments (e.g.,Fukuta and Takahashi, 1999; Hoose and Mohler, 2012). Meanwhile, many airborne studies have been used to examine snow growth processes based on temperature, supersaturation and vertical motions (e.g., Lo and Passarelli, 1982; Hobbs and Rangno, 1985; Field et al., 1999; Field et al., 2000; Korolev et al., 2000; Rangno and Hobbs, 2001; Lance et al., 2011;). More recently, airborne studies of terrain-induced wave clouds have allowed for examination of both snow growth and ice nucleation due to their laboratory like environment (e.g., Field et al., 2001; Baker and Lawson, 2006; Eidhammer et al., 2010; Field et al., 2012). For example, evaporation freezing has been observed in regions of evaporating droplets (e.g., Field et al., 2001; Baker and Lawson, 2006). Shaw et al. (2005) were able to recreate the observed nucleation mechanism in a laboratory setting and described it as inside-out contact nucleation. The majority of these studies omitted dynamical analysis with the exception of Baker and Lawson (2006), who were able to gain additional information about the structure of an unusual wave cloud by utilizing the ratio of static stability to cross mountain wind speed. Meanwhile, airborne studies in complex terrain that focus on orographic precipitation tend to incorporate dynamical processes (e.g., Woods et al., 2005; Garvert et., al 2007; Geerts et al., 2011; Yang et al., under review). Woods et al. (2005) and Garvert et al. (2007) used data from the Improvement of

Microphysical Parameterization through Observational Verification Experiment (IMPROVE) which incorporated airborne *in-situ* and remotely sensed cloud microphysical properties and dynamics to further enhance the ability of models to predict precipitation in complex terrain (e.g., Garvert et al., 2007). Garvert et al. (2007) used static stability and inverse Froude number to validate the modeled vertical structure of a passing storm to ensure that the predicted precipitation biases were primarily induced by microphysical processes and not dynamical processes. Meanwhile, Woods et al. (2005) examined the evolution of ice crystal and snow growth as a storm crossed the Oregon Cascades and found that interactions between frontal and orographic precipitation increased the scavenging of cloud liquid water and enhanced precipitation by up to 1 mm per hour. Geerts et al. (2011) used the airborne University of Wyoming Cloud Radar (WCR) to observe the role of boundary layer (BL) turbulence on snow growth processes in orographic cloud and showed that BL turbulence enhanced snow growth. Geerts et al. (2011) were unable to identify the growth mechanism due to the lack of *in-situ* microphysical observations within the BL. Yang et al. (under review) used the airborne WCR to examine cloud structures over the Medicine Bow Range in Wyoming and reaffirmed the importance of mountain-induced waves on upwind precipitation and the role of increased static instability and wind speed on spillover.

All of the aforementioned studies have greatly furthered the understanding of precipitation processes and distributions in complex terrain from dynamical and microphysical perspectives but due to the lack of data, were unable to sample the evolution of the cloud microphysics from aloft to the mountaintop. Rogers and Vali (1987) observed cloud microphysics at both the Elk Mountain Observatory (EMO) located in the Medicine Bow Mountains of Southern Wyoming and from the University of Wyoming Queen Air (UWQA) aircraft. Comparisons between crystal concentrations at EMO and on the UWQA routinely showed higher crystal concentrations at EMO. The authors attributed

the higher surface crystal concentrations to an unknown process of ice crystal generation in supercooled orographic clouds in contact with snow-covered mountain surfaces. However, blowing snow can introduce the potential for serious errors in observed ice crystal concentrations at mountaintop locations (Roger and Vali, 1987). Above a threshold wind speed, blowing snow is lofted from the surface and then advected downstream before eventually being redeposited to the snow surface. The height to which crystals are lofted depends on their size and the wind speed. Smaller crystals are more easily lofted to higher distances above the snow surface and can be advected farther downstream (e.g. Schmidt, 1982). In order to account for blowing snow, Rogers and Vali (1987) performed modeling studies to determine if the "anomalously" high ice crystal concentrations were due to the lofting of snow from the surface and although the results suggested that some contamination was possible, it was concluded that the majority of the "anomalous" crystals were not artifacts.

During the winter of 2011, two simultaneous field campaigns, the Storm Peak Laboratory Cloud Property Validation Experiment (StormVEx) and the Colorado Airborne Multi-Phase Cloud Study (CAMPS) were conducted in the Park Range of the Colorado Rockies with the mutual goal of observing cloud microphysical properties during orographic snow events. This study will utilize data from both field campaigns to better understand the evolution of hydrometeors as they fall through orographically enhanced cloud under varying stability regimes. The principal goals of this study are to gain a fundamental understanding of the interactions among dynamics, cloud structure, and cloud microphysics in wintertime orographic clouds and to examine ice nucleation processes during the CAMPS and StormVEx field programs. In addition to furthering the general understanding of orographic precipitation, this study will explore several previously unanswered questions including: 1) what are the microphysical pathways responsible for producing enhanced crystal concentrations and reflectivity at mountain top compared to airborne observations (Rogers and Vali, 1987; Geerts et al., 2011)?; 2) can a

meaningful comparison between upwind aircraft and mountaintop microphysical properties be made?; and 3) what role does the nondimensional mountain height number have on mountain top and lee slope cloud droplet and ice crystal concentrations? To better address goal number 1, data from the Isotopic Fractionation of Snow (IFRACS) field campaign, which occurred during the winter of 2014, will also be incorporated into the analysis. This study is the first comprehensive descriptive meteorological and microphysical analysis of the CAMPS and StormVEx campaigns.

Chapter 2: Methods

Section 2.1: Datasets

During the winter of 2010-2011, the Colorado Airborne Multi-Phase Cloud Study (CAMPS) and the Storm Peak Cloud Validation Experiment (StormVEx) were conducted simultaneously in the Park Range of the Colorado Rockies (see Figure 1 for the study area). Another field campaign, the Isotopic Fractionation in Snow (IFRACS) study, occurred at Storm Peak Lab during the winter of 2014.

CAMPS

CAMPS, a National Science Foundation (NSF) funded campaign, was designed to focus on the observation of wintertime mixed phase clouds using the University of Wyoming's King Air (UWKA) aircraft. The UWKA flew 29 research flights totaling 30 hours of in-cloud flight time over the Park Range of the Colorado Rockies and Muddy Mountain, Wyoming. CAMPS was planned to occur simultaneously with StormVEx (described below) in order to compare ground-based and airborne measurements. During CAMPS, the UWKA was equipped with remote and *in-situ* instruments to measure microphysical properties (see also Table 1). The Wyoming Cloud Radar (WCR) operates with a frequency of 94.2 GHz with an absolute estimated accuracy of 3dB (Wang et al. 2012). The downward and upward pointing antennas are used to characterize cloud and precipitation structure using the radar reflectivity factor (Z_e) and Doppler velocity (e.g., Pratt et al., 2009; Wood et al., 2011a; Yang et al., under review). The sensitivity of the WCR is high enough to detect cloud droplets in nonprecipitating water clouds, but since the signal is proportional to the sixth power of particle size, the largest particles dominate the signal. Therefore, in mixed-phase clouds, the WCR signal is dominated by the largest ice particles and little or no information can be obtained about the cloud droplets (Wang et al., 2012). The Wyoming Cloud Lidar (WCL) operates at a much shorter wavelength of 351nm compared to the WCR which allows the WCL signal to be dominated by cloud droplets and smaller particles in mixed-phase clouds. Using

both the WCR and WCL simultaneously allows for detailed microphysical information about both the ice and liquid structure within a mixed-phase cloud. However, in optically thick liquid cloud, the WCL becomes attenuated quickly, limiting the vertical penetration into cloud and information about the liquid structure of the cloud (Wang et al., 2012).

The UWKA was also equipped with several optical array and scattering cloud probes, including: a Particle Measuring System (PMS) Forward Scattering Spectrometer Probe (FSSP), a Gerber Scientific Particle Volume Monitor (PVM-100), and a Droplet Measurement Technologies (DMT) Cloud Imaging Probe (CIP) (Table 1). The FSSP measures single particle concentration and size between 2 and 47 µm in diameter using forward light scattering from a helium-neon laser (Knollenburg, 1981; Baumgardner, 1983; Cerni, 1983). The PVM-100 also uses light scattering but provides a bulk measure of liquid water content (LWC) and particle surface area (Gerber et al., 1994; Gerber et al., 1999) for particles between 3 and 50 µm in diameter (Wendisch, 2010). The CIP provides the two-dimensional structure of cloud particles using a linear array of diodes illuminated through the sample volume of the probe (Knollenburg, 1970). The size range for the CIP can be adjusted and was set to 25 to 1550 µm during CAMPS (see Table 1).

In addition to the scattering and optical array probes, a modified University of Colorado closed-path tunable-diode laser hygrometer (CLH), a Hot-Wire Liquid Water Sensor (LWC-100) and a LICOR 6262 (LICOR) were on board. The CLH uses tunable diode laser spectroscopy to measure total water concentration, including water vapor, liquid water, and ice (Hallar et al., 2004; Davis et al., 2007; Dorsi, 2013). The LICOR is a differential, non-dispersive, infrared gas analyzer that uses samples of known water vapor concentration as a reference for comparison and calculation of ambient water vapor concentrations (LICOR-6262 Manual, ftp://ftp.licor.com/perm/env/LI-6262/Manual/LI-6262_Manual.pdf). The LWC-100 is a latent heat-based probe that measures the liquid content of the

air based on the amount of energy required to maintain the probe at a constant temperature and can sample a liquid water content up to 3 g/m^3 with an accuracy of 0.02g/m^3 (King, 1978). CAMPS data were obtained from the University of Wyoming (at http://flights.uwyo.edu/projects/camps11/).

StormVEx

StormVEx was supported by the United States Department of Energy's Atmospheric Radiation Measurement (DOE ARM) Program and focused on collecting concurrent remote and *in-situ* measurements of cloud microphysical processes (e.g., Matrosov et al., 2012). Several of the *in-situ* measurements occurred at Storm Peak Laboratory (SPL). SPL is located on the western summit of Mt. Werner at an elevation of 3220m in the Park Range of the Colorado Rockies. The Park Range is a north-south oriented mountain range which is orthogonal to the predominant westerly flow experienced in the mid-latitudes. The lab's elevation and exposure to westerly flow makes it an excellent location for sampling mixed-phase clouds during wintertime storms (e.g., Borys et al., 2003; Saleeby et al., 2012). As a part of StormVEx, a DMT SSP100 (modified FSSP), a DMT Cloud Imaging Probe (CIP), and a DMT Precipitation Imaging Probe (PIP) (specifications of the probes are given in Table 1) were installed on a wind vane and collected data while the lab was in cloud. In addition to the cloud probes, images of snowflakes were taken on certain days with a digital camera to further document the observed microphysics. Another aspect of StormVEx was the deployment of a Balloon-Bourne Sounding System (BBSS), which used the Vaisala RS92-SGP with GPS wind finding to acquire vertical profiles of atmospheric temperature, pressure, wind speed and direction, and relative humidity (RH). The BBSS was deployed in the valley 6km upwind of SPL at an elevation of 2078m. A minimum of two soundings were launched per day and additional soundings were launched every four hours during intensive observation periods. Data collected during StormVEx were obtained from DOE ARM (at http://www.arm.gov/campaigns/amf2010valclradar).

IFRACS

IFRACS, an NSF-funded field campaign, was designed to further the understanding of snow growth processes in mixed-phase clouds and to evaluate the role that aerosols have on those processes. Samples of cloud water and snow were collected when SPL was in cloud and analyzed for stable water isotopic composition. While these samples were being collected, the SPP100, CIP and PIP were used to obtain information about the cloud droplet and crystal size distributions. The probes were run in the same manner as during StormVEx. Balloon-borne soundings were launched every two hours during intensive operating periods. The soundings were equipped with a Vaisala RS 92G radiosonde with GPS wind finding in order to acquire vertical profiles of thermodynamic variables and wind.

Section 2.2: Case Selection and Stability Assignment

The UWKA flew several different flight patterns over the Park Range in the Colorado Rockies including cross barrier flight legs, spirals, and ladders. Cross barrier flight legs were identified to determine the variability of the microphysics over the barrier. Although spiral flight patterns have frequently been used to assess the vertical development of cloud microphysics (e.g. Lo and Passarelli, 1982), they are omitted from this analysis due to their non-Lagrangian nature during CAMPS. The cross barrier WCR and WCL data were plotted to identify flights and legs of interest based on cloud structure above and below the aircraft. The WCR was also used to identify cases when the UWKA and SPL were sampling the same cloud. To ensure that the WCR signal was truly representative of the cloud and not biased by artifacts in the noise field, 99% of the noise was removed using a statistical approach. The criteria for selecting the case studies of interest were cloud depth (thickness of the cloud), distribution

over the barrier (the upwind and downwind extent of the cloud), and structure (reflectivity pattern inside the cloud). Case studies were categorized into three classifications: 1) hybrid (see Figure 2.a), clouds that were relatively deep with various inhomogeneities within the cloud structure; 2) convective (see Figure 2.b), clouds that were cellular in nature; and 3) wave (see Figure 2.c), clouds that displayed wave like structures over the barrier. For each case study, the BBSS data were used to calculate vertical profiles of $\mathbf{M_m}$, moisture, theta and potential instability. The BBSS data were interpolated to 10m intervals and then smoothed such that the minimum resolved wavelength was 500m (Yang et al., under review). A comparison of each sounding profile for each of the three cloud types was made in order to identify any systematic dynamical processes responsible for producing the observed cloud structures. Due to the proximity of the sounding location to the mountain barrier, model-derived soundings from the Weather Research and Forecasting model (WRF) accompany the observed soundings (WRF setup details are described in Section 2.5). Additionally, WRF provides high resolution 4-dimensional parcel trajectories for additional airmass and dynamical analyses.

Section 2.3: Calculation of Cloud Microphysics

The optical array probes and the FSSP are used to compare the upwind UWKA cloud particle size distributions (PSDs) to the SPL PSDs. Although PSDs provide an enormous amount of information about microphysical properties, their retrieval from optical cloud scattering and imaging probes is challenging due to complexities in determining the depth of field (DOF), the effective sample area, and the overestimation of particle concentration due to particle shattering. The DOF and effective sample area depend on the particle velocity through the optical path (Baumgardner and Korolev, 1997), the particle displacement from the center of focus (Knollenburg, 1970; Joe and List, 1987) and the effective

photodiode array width (Knollenburg, 1970). Shattered or splashed particle contamination has been an area of concern for quite some time (e.g., Cooper, 1978; Gardiner and Hallet, 1985; Korolev et al., 2011) and recent modifications to probe arms (anti-shattering tips) and post-processing algorithms (the use of inter-arrival times) have been developed in an attempt to mitigate contamination (e.g., Field et al., 2003, 2006; Korolev et al., 2011). Shattering contamination is believed to have a higher impact at aircraft speeds (Gardiner and Hallet, 1985) but ground based studies using an FSSP measured ice concentrations between 300 and 3000 times higher than actual ice concentrations in a simulated cloud (Vali et al., 1980, 1981). In addition to sample area and shattering errors, coincidence errors occur when multiple particles enter the sample volume simultaneously, which can lead to over-sizing or rejection of particles by quality control checks (Dorsi, 2013). However, coincidence errors are greatly reduced in optical array probes compared to scattering probes due to a relatively small viewing volume compared to the sample area (Knollenberg, 1970).

With the above challenges in mind, the PSDs from the UWKA CIP were calculated to a one-second resolution using image analysis post processing software (provided by the National Center for Atmosphere Research Mesoscale and Microscale Meteorology Division, NCAR/MMM) which applies corrections for DOF and inter-arrival times. DOF corrections are essential for particles with small diameters relative to the probe resolution and at high particle velocities (e.g., Baumgardner and Korolev, 1997; Korolev et al., 1998; Strapp et al., 2001). Inter-arrival time corrections remove shattered particles by identifying particles that pass through the DOF more closely spaced than Poisson counting statistics would predict (e.g., Field et al., 2003,2006; Dorsi, 2013). The software uses an approximate maximum diameter to size the particles by finding the diameter of the smallest circle that completely encompassed the 2D projected particle (Heymsfield et al., 2013). In order to be consistent, the SPL CIP and PIP PSDs were calculated to one-second resolution using the same corrections even though it has

been shown that the DOF correction is smaller at low wind speeds (Strapp et al., 2001) and the likelihood of shattering is much lower at relatively slow wind speeds at the surface.

Section 2.4: Microphysics Comparisons

In order to assess the ability of the $\mathbf{M_m}$ to predict the distribution of microphysics over the barrier, the cross-barrier flight legs were averaged based on altitude and case type. Averaging was limited to periods when the UWKA was determined to be in cloud based on the presence of ice or liquid water from the *in-situ* probes. Upwind and downwind cloud droplet and ice PSD's (methods for calculating the PSD's are listed below) were compared in order to identify systematic relationships between cloud microphysical properties at flight level and $\mathbf{M_m}$.

A comparison was also done between the upwind UWKA and SPL microphysics. Comparisons were limited to periods when the WCR indicated relatively homogeneous cloud along the cross-barrier flight leg. An approximate hydrometeor trajectory was calculated to estimate the upwind region for the comparison and the lag time, or the time for the particles observed from the UWKA to reach the lab. The trajectories were calculated using aircraft altitude, aircraft to mountain top mean layer U-wind and an assumed hydrometeor fall speed of 1 m/s (Figure 3). Due to the mountain top location of SPL, the possible contamination from blowing snow was assessed by comparing wind speed and crystal concentration. Previous research on blowing snow shows a decrease in crystal size with an increase in distance above the snow surface during blowing snow (Schmidt, 1982). Therefore a comparison between wind speed and small and large crystal concentrations was done. Additionally, previous work has shown that gustiness leads to an increase in blowing snow due to the increase in shear stress on the snow surface. To evaluate this issue, a comparison between small ice crystal concentration and gustiness was calculated. Gustiness was assessed by using the swinging nature of the wind vane the

cloud probes are mounted on. When a gust of wind hits the wind vane, the increase in shear forces it to swing off the axis of the wind. Thus the ratio of the u-component and the v-component of the wind can be used as a metric for gustiness.

Section 2.5: Modeling Setup

High resolution numerical modeling was done using the Weather Research and Forecasting version 3.6.1 model (WRF) in order to augment and validate the measured vertical profiles for each case study type. The model domain consists of three, two-way nested grids, with the outer and innermost domains centered over SPL as can be seen in Figure 4. The outer domain contains 341 X 166 horizontal grid points with spacing of 10km. Grid 2 consists of 286 X 280 horizontal grid points with a spacing of 3.33km and the innermost grid, grid 3, has 280 X 406 horizontal grid points and a spacing of 1.11km. All three grids contain 41 vertical levels. The model was initialized using North American Regional Reanalysis (NARR) 32-km, 3-hour data. The long wave and shortwave radiation physics are handled with the NCAR Community Atmospheric Model Radiation Scheme (Collins et al. 2004). The Monin-Obukhov (Janjic Eta) scheme is used for the surface layer physics and the Noah Land Surface Model is used for the land surface option due to upwind wintertime snow cover (e.g., Skamarock et al., 2008). The planetary boundary layer physics used the Mellor-Yamda-Janjic (Eta) TKE scheme (Janjic, 1994) due to the use of the Monin-Obukhov (Janjic-Eta) scheme (Monin and Obhukhov, 1954; Janjic, 1996, 2002) for the surface layer physics. The microphysics scheme explicitly predicts the mixing ratios of five liquid and ice species and the number concentration of cloud droplets, making it a single moment scheme except for cloud droplets, which is two moment (Thompson et al. 2008). Model-derived cross-barrier profiles of vertical velocity, theta and liquid water content are compared to WCR reflectivity and flight level observations of liquid water content and vertical velocity in order to evaluate the model's

performance. Upwind model-derived atmospheric profiles are compared to the observed BBSS data in order to gain a better understanding of the hydrostatic meso-scale upwind environment.

Chapter 3: Data Analysis

Section 3.1: Cloud Probe Image Processing

In order to obtain reliable and consistent PSD's, the UWKA and SPL CIP were processed using image analysis software provided by NCAR/MMM. The software uses a circle-fit method to size the particles by fitting the smallest possible circle around a particle image and then uses the diameter of that circle as the diameter of the particle. This sizing method allows for use of the "area-ratio" or the ratio of occluded diodes to the area of the circle for particle rejection. Particles are rejected when they have a low area ratio (less than 0.1) and are larger than the size-bin range possible. Particles are also rejected based on their inter-arrival time in an attempt to correct for particles that splash or shatter on the probe arms. The inter-arrival time rejection (ITR) follows the technique described in Field et al. (2006). Partially imaged particles that touch either or both ends of the diode arrays are processed. To account for this, the sample area is calculated using the "reconstruction" method outlined in Equation 17 of Heymsfield and Parrish (1978).

Shattering has been shown to drastically impact the PSD for particles up to several 100 μm in diameter at aircraft speeds (e.g. Field et al., 2006). Figure 5 shows the average UWKA CIP PSD with and without the ITR for the seven flights analyzed limited to seconds when particles were present. Consistent with previous studies, the ITR affects the PSD for particles 300 μm and smaller. When all channels of the CIP are used, the ITR reduces the mean particle number concentration by 42.7%. If the first two channels of the CIP are omitted (only 75-1550 μm particles are considered) due to possible miss-sizing and undercounting (e.g. Strapp et al., 2001), the average ITR reduction in mean particle number becomes 35.9%.

The ITR was also applied to the SPL CIP in order to determine the impact of shattering at much lower wind speeds. A much smaller impact was observed with a 6.11% reduction in average crystal concentrations when all sizes are included and a 14.32% reduction was observed when the first two channels were omitted. The increase in percent difference when the first two channels are omitted is due to the ITR having a maximum effect for 75 and 100 μm crystals. Figure 6 shows the difference in the SPL CIP PSD with and without the ITR.

Section 3.2: UWKA Liquid Water Probe Comparison

The liquid water content (LWC) measurements on the UWKA using three different probes, the PVM, the FSSP and the LWC-100 hotwire, were compared to determine the most reliable measurement for this study. Of the three, the PVM and the FSSP were consistently the closest to each other when all three sensors reported LWC concentrations of 0.01 g/m^3 or greater (see Figures 7, 8 and 9). The FSSP LWC was routinely higher than the PVM LWC but this is believed to be primarily due to ice particle shattering on the FSSP inlet, as can be seen in Figure 10. The FSSP's bimodal PSD, when shattering is identified on the CIP, is evidence of shattering on the FSSP. However, when the PVM and FSSP are compared when no crystals are present and both probes have LWC of 0.01 g/m^3 or greater, the FSSP still reported higher LWCs than the PVM (see Figure 11). Ground-based studies done by Wendisch (1998) and Wendisch et al. (1998) showed an underestimate in LWC by the PVM when cloud droplets grew in size. Contrary to Wendisch (1998) and Wendisch et al. (1998) a comparison between the LWC from the FSSP and PVM based on effective diameter shows no dependence on particle size when shattering was not observed on the CIP (see Figure 12). When shattering was observed on the CIP, the FSSP significantly overestimated the LWC for particles with an effective diameter of 30 to 40 μm (see Figure 12), indicating that the majority of particles shattered by the FSSP arms fall in the 30-40 μm range, which is at the lower size limit for the CIP. Due to the observed impact of shattering on the FSSP inlet

and the potential for shattered particles to be at the lowest detection limit of the CIP, the PVM was chosen as the LWC measurement for this study.

Section 3.3: Colorado Laser Hygrometer

Ice water content (IWC) was calculated from a modified University of Colorado closed-path tunable-diode laser hygrometer (CLH). In order to retrieve IWC, the total water measurement from the CLH was reduced by the water vapor concentration (from the Licor) and the LWC from the PVM. The CLH collected data during 6 out of 7 flights examined in this study. A comparison between the CLH-derived IWC and the concentration of crystals between 800 and 1550 μm obtained from the UWKA CIP for the six flights when the CLH was operational is shown in Figure 13. The smaller crystals are excluded because IWC is dominated by the larger crystals. The CLH-derived IWC corresponds well with the large crystal concentrations until the start of research flight 12 (represented by the green line). Large negative values of IWC are observed during research flight 12 and the subsequent 2 flights. In order to ensure that the PVM was functioning properly during these three flights and was not the cause of the negative values of the CLH-derived IWC, a comparison between the UWKA FSSP and PVM was done (Figure 14). The relationship between the PVM and FSSP LWC during this period is consistent with that seen for all seven flights examined in this study (Figure 8). It can therefore be inferred that the negative values of the CLH IWC during this period were not due to over-estimation of LWC by the PVM. Due to this inconsistency in the CLH-derived IWC, it is omitted from the following analysis.

Section 3.4: Ground Based Probes

PSD's from the three cloud probes at SPL were averaged for all seconds when crystals were present at SPL. A comparison among the three PSD's shows that the probes were in good agreement during the seven flights examined (Figure 15).

Chapter 4: Results and Discussion

Of the 29 research flights (RF), seven were chosen for this analysis based on their observed cloud structure, meteorological characteristics, and proximity to SPL. The flights were binned into 3 categories as follows, three convective (RF# 12, 26 and 28), two wave (RF#3 and RF#5) and two hybrid cases (RF#1 and RF#9). The categories were assigned based on the observed cloud structure from the WCR. Each category is broken into sections that compare and contrast the WCR radar images, the balloon-borne soundings, the average UWKA observed microphysics, and the comparison between the UWKA and SPL microphysics for each flight within the category. A comparison between modeling results and one of the flights in each category is also included. Lastly, a separate section is dedicated to the discussion of the relationship between cloud droplet concentrations and crystal concentrations at SPL.

Section 4.1: Convective Cases

WCR:

The WCR retrievals show the convective nature of the low-level cloud structure for RF#12 and RF#26. During RF# 28, the normally downward pointing antenna of the WCR was disabled so that the side antenna could be operated. Therefore, RF#28 was identified as convective based on the upward pointing antenna of the WCR and the downward pointing WCL. An example of the structure from all three cases is shown in Figure 16. A comparison between the WCR images from RF#12 and RF#26 shows some significant structural differences, mainly that during RF#12, only a single convective cloud deck was observed from the WCR for the entire flight while the convective cloud appeared to be developing throughout RF#26. RF#26 also featured an upper-level laminar cloud above the developing convection, as can be seen in Figure 16b. Even with the convective nature of the low level clouds, form drag is

evident in all three cases, comparable to water flowing over a rock, resulting in lowering the cloud top heights to the lee of the barrier (e.g., Lin, 2007) (e.g. Figure 16a and 16b). During RF#12, the convection appeared to intensify on the windward slope of the barrier, associated with strong updrafts, as derived from the WCR (Figure 17). This is likely due to the release of potential instability as the air is lifted over the barrier. Meanwhile, during RF#26, the convective nature of the clouds was much less pronounced and cloud base was routed closer to mountain top. This is likely due to low-level blocking and the reduced lifting of the low-level air over the barrier (sounding measurements support this and are described in the following section).

BBSS:

Vertical profiles of U-wind speed, static stability and the nondimensional mountain height number ($\mathbf{M_m}$) are calculated from the balloon-borne soundings taken during each flight (see Figure 18). Vertical profiles of $\mathbf{M_m}$ can explain the major differences between RF#12 and RF#26. For RF#26, the low-level $\mathbf{M_m}$ predicts strong low-level blocking between the 2000m (the surface) and 2500m ASL and a second layer of blocking that straddles the mountain top from 3200m up to 3500m ASL. The low-level easterly flow and the stagnation point observed in the sounding is a product of flow blocking and the ensuing flow splitting (e.g., Hunt and Snyder, 1980; Smith, 1989; Smolarkiewicz and Rotunno, 1990; Baines and Smith, 1993). The low-level counter flow and the stagnation point are known as the dynamically induced secondary circulation. Jiang (2003) found an enhanced updraft upstream of the barrier associated with the dynamically induced secondary circulation as the reversed flow met with the background flow, producing a region of enhanced convergence (see Figure 11 in Jiang, 2003). In this case, no evidence of an enhanced updraft or associated precipitation is observed upstream of the barrier from the WCR (Figure 16b). The WCR does, however, show an elevated layer of convection consistent with and above a low-level stable layer and blocked flow. The profile of static stability supports this with a transition from positive to negative stability at 2600 meters (Figure 18b).

During RF#12, the $\mathbf{M_m}$ is below unity from the surface up to 6 km, indicative of spillover and air freely flowing up and over the mountain barrier. WCR vertical velocity observations support this with abundant turbulence observed near the surface, indicative of a well-mixed boundary layer and no evidence of low-level blocking, as shallow water theory predicts (e.g. Long, 1953; Durran, 1990; Geerts et. al, 2011). Without the downward pointing radar during RF#28, it is difficult to determine the effectiveness of $\mathbf{M_m}$ at predicting the low-level cloud structure. However, based on the convective nature of the liquid water (observed from the WCL, not shown), the $\mathbf{M_m}$ appears to be a good predictor of the flow over the barrier with no blocking expected above 3km.

The strong upward vertical velocities noted from the WCR on the windward slope of the Park Range during RF#12 are supported by a deep layer of potential instability from 2500 to 3500 meters (Figure 18d). The other two convective cases have much less potential instability along the mountain barrier, and as such, the vertical velocities are expected to be lower (WCR confirms this for RF#26). On the leeward slope, the WCR vertical velocities support the presence of form drag, consistent with shallow water theory and the findings of Lilly and Klemp (1974), who showed the presence of drag when the $\mathbf{M_m}$ was 0.6 or below.

Modeling Results

Modeling was done for RF#12, as it was the most convective of the three cases observed. An analysis of the 700 hPa temperature, height and relative humidity fields show strong cold air advection and high relative humidity over the Park Range (Figure 19). Unfortunately, the 700 hPa field intersects the terrain over the higher elevations of the Rocky Mountains, making the interpretation of the contour analysis challenging. The 700 hPa vertical velocities are conducive for the development of precipitation with widespread and orographically enhanced ascent located over the Park Range (Figure 20). The 500

hPa absolute vorticity field supports the 700 hPa ascent with positive vorticity advection and vorticity values in the 15 to 18 $x10^{-5}$ s^{-1} range (Figure 21).

With the large-scale dynamics supporting precipitation over the region, a closer comparison between the balloon-borne sounding and the model-derived sounding reveal very similar features. Figure 22 shows very similar profiles of static stability and $\mathbf{M_m}$ above 2.5 km between the two soundings. The model over predicts the U-component of the wind below approximately 3700 meters and then under predicts above that altitude (Figure 22a). It is difficult to determine if above that altitude, the model-derived sounding or the observed sounding is more representative of the actual upwind profile due to the downstream drift of the observed sounding. Even with the slight discrepancies between the model-derived sounding and the observed sounding, the vertical profiles support the presence of spillover, as predicted from theory with $\mathbf{M_m}$ at or below unity from the mountaintop and above (e.g. Sinclair et al. 1997).

A comparison between the UWKA average cross-barrier flight legs and the model-derived average cross-barrier LWC and vertical velocity fields at the same altitude further validate the model. Figure 23 shows the model and observed cross-barrier flight level vertical velocity and LWC for RF#12. The model is generally in good agreement with the observations with upward motion observed upwind of SPL and descent downwind of the crest. However, the maximum ascent is displaced 7km upwind of the observed maximum and the descending motion occurs closer to SPL in the model than in reality. On the leeward slope, the model under predicts the maximum downward motion by 1 m/s but is in generally good phase with the location of the maximum. The model-derived LWC responds to the vertical motion field with an upwind displacement of the LWC compared to observed values (Figure 23b). The differences between the observed and model-derived values are likely due to the convective nature of the observations and the 1 km resolution of the model versus the 100 meter resolution of the

aircraft. Another possible explanation could be due to the timing difference between the model-output and the observed data.

Model-derived vertical cross-sections of theta, vertical velocity, LWC and IWC fields (Figure 24) support the distribution of reflectivity and vertical velocity shown in Figure 17. The model captures the development of convective cells just upwind of the barrier in a region of enhanced vertical motion and the continued development of the cells as they ascend the windward slope of the Park Range. To the lee of the barrier, the model-derived LWC drops off more rapidly than the observations from the WCL show but the model-derived IWC is consistent with the cellular structure of the cloud observed on the WCR (Figure 17). The release of potential instability as latent heating is also observed in the model with a stretching of the theta surfaces over the windward slope of the Park Range. Overall, the model confirms the relationship between the observed cloud structure and $\mathbf{M_m}$, which is consistent with previous observations and theory (e.g., Sinclair et al., 1997; Colle, 2004).

UWKA Average Microphysics:

In-situ aircraft microphysical measurements were averaged for the cross barrier flight legs for all three of the convective flights to obtain an understanding of how the microphysics varied over the barrier for each convective case. The altitude and number of cross-barrier flight legs used to compute the averages for each flight are listed in Table 2. For the three convective cases, the average flight altitudes closest to the barrier used in the averages varied between 4300 and 4500 meters and contained between three and five cross-barrier legs.

For all three convective cases, the average cross-barrier profiles of vertical velocity are consistent, as shown in Figure 25a. These flight level observations support the vertical velocity

measurements from the WCR with form drag on the lee of the barrier (e.g. Figure 17b). Weak upward vertical motion is observed upwind of the crest that generally ranges between 0 and 1 m/s. To the lee of the crest, vertical velocity quickly becomes negative and bottoms out at -2 m/s before recovering to approximately 0 m/s. This type of plunging flow and recovery is predicted in cases where $\mathbf{M_m}$ is less than 1 (Lilly and Klemp, 1974). RF#12 and RF#28 are the quickest to recover on the leeward slope and generally trace each other. RF#26 is much slower to recover on the leeward slope and this may be due to weaker convection at the beginning of the flight and a higher $\mathbf{M_m}$ near mountain top (Figure 18d).

The average LWC over the barrier is rather consistent between all 3 convective flights (Figure 25b.). There is generally an increase in LWC as the aircraft approaches the barrier with a maximum observed just upwind of the crest. Then the LWC decreases to the lee of the barrier, as expected, in response to subsidence. The pattern of the LWC over the barrier is consistent with the updraft-based hypotheses for mixed-phase cloud persistence (e.g. Korolev and Mazin, 2003). However, the maximum in aircraft-observed upward vertical velocities are not co-located with maximum in the LWC. This is likely due to the strong mixing associated with the convective nature of the clouds.

There is much less consistency between the distributions of crystal concentration observed by the UWKA CIP over the barrier. Ice crystal concentrations are an order of magnitude higher in RF#28 than during the other two convective flights (not shown). However, when the first two channels of the CIP are omitted from the analysis (due to sampling issues at aircraft speed (Strapp et al., 2001) and the inability to determine particle phase), the concentrations are all on the same order of magnitude (see Figure 25c). This suggests that during RF#28, the UWKA was flying through a region of newly formed ice or large supercooled cloud droplets near cloud top. Based on the observations from the upward pointing WCR, this is likely the case as the UWKA was located just below cloud top (see Figure 16) where enhanced ice nucleation may be occurring due to colder temperatures at that altitude.

Even with the first two channels of the CIP removed from the total concentration, the distribution of ice over the barrier is much less consistent than the vertical velocities or the LWC. In general though, there is an increase in ice concentrations to the lee of the crest (see Figure 25c.) The increase is consistent with theory, which predicts enhanced spillover when upstream conditions are unstable (e.g., Sinclair et al. 1997; Yang et al., under review). To further determine the evolution of snow over the barrier at flight level, upwind and downwind averages of particle size distributions from the CIP were calculated. For all three convective cases, the crystal concentrations increased to the lee of the barrier. Figure 26 shows the percent difference between the upwind and downwind particle size distributions. Of the three convective flights, the largest difference was observed during RF#28, as there was very little cloud sampled on the windward slope of the barrier.

UWKA and SPL comparisons

A direct comparison between CIP particle size distributions between the upwind UWKA and SPL was only possible for RF#12. During the other 2 convective cases, cloud was not observed far enough upwind for the trajectory model to work. Comparisons for RF #12 show much higher ice concentrations observed at the lab at all but the largest sizes of the distribution (Figure 27). Due to the lack of trajectory comparisons available for RF#26 and 28, average particle size distributions were computed for seconds when the UWKA was upwind of SPL, in cloud, and lower than 4700m. The results show no real consistency among the convective cases but do show a sharp increase in concentrations of particles less than 200 μm for RF# 26 and 28 (see Figure 28). RF#12 shows a slight increase in the difference for crystals less than 200 μm but this difference is much less exaggerated than the increase observed in the other two cases. The smaller difference in RF#12 may be due to enhanced updrafts and is examined further in section 4.4. This is consistent with the majority of the trajectory comparisons during RF#12. However, the comparison in Figure 27 is consistent with the general observations in Figure 28.

Discussion

The three convective fights were identified based on the convective nature of the cloud structure obtained from the WCR and then intercompared to determine the ability of the $\mathbf{M_m}$ and potential instability to predict the observed cloud structures, the flight level microphysics and the feasibility of comparing upwind airborne microphysics to mountaintop microphysics. Consistent with previous work, (e.g., Sinclair et al., 1997), $\mathbf{M_m}$ was an effective predictor of the distribution of the cloud over the barrier during the three convective flights. When $\mathbf{M_m}$ was less than unity from the surface up to mountaintop (RF#12), the airmass was able to ascend the barrier uninhibited. When $\mathbf{M_m}$ was larger than unity below mountaintop (RF#26 and 28), low level blocking was observed, increasing the altitude of cloud base and reducing windward precipitation (based on the strength of the WCR reflectivity reaching the surface). Above mountaintop, the ability of $\mathbf{M_m}$ to predict the cloud structure was much less robust and became more of a function of the static stability. Potential instability played an important role in determining the strength of the vertical motions observed on the windward barrier. During RF#12, a deep layer of potential instability was responsible for producing much stronger updrafts and convective cells on the windward slope of the barrier than during the other two convective flights.

Unlike previous ground based studies (e.g., Sinclair et al., 1997), the UWKA was able to determine the distribution of vertical velocity and cloud microphysics over the barrier. For all three convective flights, the vertical velocity measurements were surprisingly consistent considering the convective nature of the cloud structure. The maximum flight level upward motion was consistently observed over the windward slope of the barrier and form drag was present to the lee of the crest. The profiles of LWC over the barrier were relatively consistent with the vertical velocity field but maximum in LWC were not collocated with maxima in vertical velocity. This is mainly due to the response of LWC to the vertical motion throughout a column of air rather than just at a single slice. The distribution of ice

over the barrier was independent of the flight level vertical velocity and LWC. However, consistent with previous ground-based observations of spillover, higher concentrations of ice were observed downwind of the crest during all three convective flights (e.g., Sinclair et al., 1997; Kaplan et al., 2012).

A direct comparison between upwind and mountaintop microphysics using a simple hydrometeor trajectory was only possible during RF#12. To account for this, the percent difference between the average upwind and the average mountaintop crystal size distributions was calculated. There was no consistency among the percent differences for the three convective cases except at crystal sizes smaller than 200μm (Figure 28). The consistent increase in the percent difference of these small crystals confirms the observations of Roger and Vali, (1987).

Based on the observations from these three flights, $\mathbf{M_m}$ and potential instability are effective predictors of the distribution of cloud over the mountain barrier. All three convective cases had higher flight-level crystal concentrations to the lee of the barrier consistent with previous ground based measurements and further supporting the ability of $\mathbf{M_m}$ to predict the distribution of precipitation over a mountain barrier (e.g., Sinclair et al., 1997; Kaplan et al., 2012). The feasibility of comparing upwind and mountaintop microphysics was inconclusive in this case but a consistent enhancement in crystals smaller than 200μm was observed at mountaintop, consistent with previous observations (Rogers and Vali, 1987).

Section 4.2: Wave Cases

WCR

Research flight number 3 (RF#3) is highlighted by trapped lee waves. The WCR shows two distinct levels of trapped waves downwind of the crest (see Figure 29a.). Radar-derived vertical velocities show an elevated zone of weak turbulence close to mountaintop on the windward slope and strong turbulent mixing to the surface on the leeward slope, as is expected under lee wave conditions (Figure 29b., e.g., Ralph et al., 1997; Geerts et al., 2011). The WCR-derived vertical velocities also support the presence of trapped lee waves versus vertically propagating waves, as the sign of the wave-induced vertical motion does not change with height (e.g., Ralph et al., 1997). The WCR shows a much more typical orographically-induced cap cloud with weak waves observed to the lee of the barrier during RF#5, as can be seen in Figure 30a. A persistent updraft is observed upwind of the barrier directly below a region of high reflectivity (see Figure 30b). This feature is consistent throughout the flight and is due to upstream topography not shown in the WCR cross-section.

BBSS

During both wave cases, $\mathbf{M_m}$ predicted flow blocking at the mountaintop level, which is consistent with linear and shallow water theory for the presence of lee waves (e.g. Long 1953; Smith, 1989; Durran, 2003). During RF#3, a 500 meter layer of stagnant flow is observed from the surface up to 2.5 km ASL (Figure 31.a). This layer is indicative of strong blocking and produces a very high $\mathbf{M_m}$ up to 2.6 km ASL, while $\mathbf{M_m}$ slowly drops to near unity above the mountaintop (Figure 31c). Based on shallow water theory, an acceleration of the flow is expected as the air ascends the barrier when $\mathbf{M_m}$ is larger than unity at mountaintop (subcritical flow, e.g. Long 1953; Durran, 1990). The vertical profiles of the cross barrier wind speed support this with a rapid increase in flow as the balloon ascends towards

mountaintop (Figure 31a). This acceleration is due to the increase in the pressure gradient forces over the fluid depth as the fluid thins (e.g. Durran, 1990). Fluid thinning is observed by the WCR as the air ascends the barrier, supporting shallow water theory (Figure 29). However, the WCR also shows the presence of trapped lee waves, which are not predicted by shallow water theory and are associated with nonhydrostatic processes (e.g., Scorer 1949; Durran, 1990). Trapped lee waves arise when large vertical variations in static stability and cross-barrier wind speed occur and can be predicted with linear theory (Scorer, 1949). The sounding supports the presence of large variations in static stability with height, as can be seen in Figure 31b. Vertical variations in the Scorer Parameter also support the presence of trapped lee waves. In particular, Ralph et al. (1997) showed that sharp increases in the Scorer parameter collocated with relatively high static stability are conducive for trapped lee wave formation. Vertical profiles of the Scorer Parameter are consistent with the observations made by Ralph et al. (1997) and support theory (Figure 31d).

During RF#5, a large increase in $\mathbf{M_m}$ is observed at the mountaintop associated with a deceleration and a minimum in the cross barrier flow (Figure 31). Long (1953) proposed that a deceleration in the flow at mountaintop was observed when the acceleration on the flow acted in the same direction as gravity and considered it supercritical flow ($\mathbf{M_m} <1$) which is the opposite of the $\mathbf{M_m}$ observed (Figure 31c). Due to the proximity of the sounding site to mountain and the potential for drift, the sounding could have sampled the terrain-induced deceleration instead of the true upwind environment, ultimately producing an artificially high $\mathbf{M_m}$. To verify whether the $\mathbf{M_m}$ value was indicative of the upstream environment, model-derived soundings were calculated. Model-derived sounding were calculated for points 10, 30, 50 and 80 km upwind of the barrier and all supported the observed sounding with decelerating flow and a high $\mathbf{M_m}$ at the mountaintop the level. Additionally, during

supercritical flow, the fluid is predicted to thicken as it crosses the barrier and, as can be seen in Figure 29a, no change in cloud depth occurred over and upstream of the barrier (Durran, 1990).

Modeling Results:

Modeling was done for RF#3 and RF#5 but RF#3 was chosen for discussion due to the presence of strongly trapped lee waves. The model-derived synoptic scale features show SPL located underneath the right exit region of the jet in a region of weakening ageostrophic flow (Figure 32). This location is conducive for upper-level subsidence and warm air advection associated with the low-level return branch of the jet. The 700 hPa vertical velocities support this with weak subsidence or no vertical motion in the vicinity of the Park Range (Figure 33). Weak warm air advection is also present with warmer air observed upstream of SPL (Figure 34). Weak positive absolute vorticity (negative relative vorticity) advection is present at 500 hPa (Figure 35) further supporting subsidence throughout the column. The sinking motion coupled with warm air advection produces an environment favorable for lee wave trapping and strong stable layers.

Model-derived soundings also support the presence of trapped lee waves with strong static stability and $\mathbf{M_m}$ greater than unity from the surface up to 6km ASL (Figure 36). The model-derived soundings are in good agreement with the observed soundings but again show some discrepancies in the strength of the wind speed with the observed sounding stronger than the model (Figure 36a). As in RF#12, this is likely due to the advection of the observed sounding into a region of higher velocities downstream of SPL (based on model estimates).

Due to the lack of flight level LWC when the trapped lee waves were observed and model-derived LWC at flight level, a direct comparison was not done for this case. However, model-derived vertical cross-sections of theta, vertical velocity, LWC and IWC (Figure 37) are very consistent with

observations from the WCR and the WCL (Figure 29). Upwind of the barrier, the model produces a stratiform cloud consistent with the WCR. At SPL, the model produces a spike in LWC associated with orographic lifting, consistent with the WCL (Figure 29c). In the lee of the barrier, the model reduces the IWC and drops the LWC to zero, except in regions where strong updrafts are present, associated with the lee waves. The model-derived lee wave features are consistent in both location and magnitude with the observations made by the WCR and WCL. The only difference between the model and the observations is the lack of the secondary and tertiary cloud decks observed on the WCR (Figure 29). As with RF#12, the model confirms the relationship between the observed $\mathbf{M_m}$ and the distribution of microphysics over the barrier with remarkable consistency.

Average Microphysics

For both wave cases, the average cross-barrier flight legs show remarkable consistency in the aircraft observed vertical velocity (see Figure 38a). Upwind vertical velocities peak around 1 m/s, 13km upwind of the crest. The upwind displacement of maximum vertical velocity is consistent with flow blocking as it effectively moves the crest of the barrier upwind (e.g., Colle, 2004). For RF#5, the maximum upward vertical velocity is collocated with the dynamically-forced secondary circulation but is much weaker at flight level than observed on the WCR radar. To the lee of the crest, strong plunging motion is observed during RF#3. The descent to the lee of the crest is weaker on RF#5 and much slower to develop. As supported by linear theory and the WCR images, a rapid recovery in the flow is observed approximately 9km downwind of the crest for both flights. The period of the waves is almost identical for both flights with the only difference in the waves being their amplitude. The vertical motions in the lee waves are 2m/s stronger than in RF#5. This is likely due to stronger low-level stability and stronger cross-barrier wind above mountaintop during RF#3 (Figure 31).

Due to the relatively dry and shallow nature of the orographic wave clouds, observed LWC measurements are relatively low (see Figure 38b). For RF#3, 2 peaks in LWC are observed on the windward slope with the first occurring approximately 15km upwind of the crest and the second near the crest. The first peak is likely associated with upstream propagating gravity waves as theory would predict. During RF#5, LWC peaks upwind of the crest in the region downwind of the dynamically-forced secondary circulation. Downwind of this maximum, the LWC dissipates and drops off to zero just upwind of the crest. On RF#3, the LWC rapidly dissipates just to the lee of the crest before resurging downwind in association with the strong upward motion of the second lee wave. This resurgence/formation of LWC can also be observed at the 6000m flight level when the UWKA was sampling an upper-level trapped lee wave (Figure 29c).

Ice crystal concentrations peak upwind of the crest during RF#5 (see Figure 38c), which is consistent with observations from the WCR. Meanwhile, during RF#3, very little ice is present upwind of the crest at flight level, with significant ice only appearing downwind of the crest. A secondary maximum is also observed downwind of the crest during RF#5. The downwind maximum is in phase with a decrease in mean number weighted diameter (MWD), consistent with new ice formation or sublimating crystals mixing up from lower altitudes. Previous work done in orographic clouds has observed the rapid glaciation of lee wave clouds in regions where downdrafts cause evaporating droplets to freeze (e.g., Field et al., 2001; Baker and Lawson, 2006). This process is known as inside-out contact nucleation or "evaporative freezing" and has been recreated under laboratory conditions (Shaw et al. 2005). However, this mechanism is likely not responsible for the observed ice formation, especially since very little LWC is present, and the region of evaporating droplets is approximately 8 km upwind. More likely, and consistent with observations from the WCR, is the advection of partially sublimated crystals from lower levels of the cloud where initial crystal concentrations were higher than observed at flight level. During

RF#3 at 6000m, the UWKA observed a rapid increase in ice crystal concentration and MWD in the trough of a trapped lee wave (not shown). The WCR confirms the increase in crystal concentration and MWD with increasing reflectivity observed in this region. This is likely a region of evaporative freezing and the continued growth of ice through the Wegener-Bergeron-Findeisen Process. However, due to the lack of flight level observed LWC and the lack of the upward pointing Lidar, the presence of cloud water and therefore evaporative freezing cannot be confirmed.

Average percent differences between upwind and downwind flight-level CIP crystal size distributions are displayed in Figure 26. Higher crystal concentrations are observed at all sizes on the leeward slope of the barrier during RF#3. This is likely an artifact of the shallow nature of the clouds sampled during the flight rather than a signal of more crystals at all sizes on the leeward slope of the barrier. Similar sampling issues likely occurred during RF#5 due to the cloud type. However, much higher concentrations of large crystals were observed on the windward slope of the barrier but the noisiness of the signal is indicative of only a few large crystals present on either side of the barrier.

UWKA and SPL comparisons

Particle size distribution comparisons between the upwind UWKA and the SPL CIP during RF#3 show much higher concentrations at all sizes at SPL than on the UWKA. This is consistent with the WCR reflectivity observed over the barrier. No comparison was possible during RF#5, as the trajectory model predicted that the upwind crystals would reach the lab after sampling at SPL had ended. To further understand the comparison between upwind microphysics and mountaintop microphysics, the percent difference between the upwind UWKA CIP PSD and the SPL PSD was calculated. No consistent signal was identified for the two wave cases sampled from the UWKA and SPL, except for crystals smaller than

200 µm, where a strong increase in crystal concentration was observed at SPL during RF#5 and a much weaker increase was observed during RF#3 (see Figure28).

Discussion

Both of the wave cases examined in this study displayed values of $\mathbf{M_m}$ above unity at the mountaintop level, supporting the presence of blocked flow and the formation of waves on the leeward slope. However, the cloud structure observed by the WCR was significantly different between the two cases, with one case consisting of trapped lee waves and the other showing characteristics of a typical cap cloud. The differences in cloud structure resulted from nonhydrostatic processes, limiting the ability of $\mathbf{M_m}$ to predict the lee wave structure of the cloud. In order to better predict the lee wave structure, an understanding of the lee environment is necessary (e.g., Long, 1953). Additionally, incorporating other indices such as the Scorer Parameter (Scorer, 1949; Ralph et al., 1997) to compliment $\mathbf{M_m}$ can be helpful in predicting the presence of trapped lee waves.

Regardless of the observed lee wave structure, the profiles of vertical velocity over the barrier were remarkably consistent between the two wave cases with the major difference being the magnitude of the vertical motion in the lee waves. A comparison between the flight-level microphysics was almost impossible due to the UWKA sampling at cloud top. However, this is consistent with theory, as blocked flow is expected to produce shallow laminar flow upwind of the barrier. To the lee of the barrier, the microphysics are expected to be determined by the lee wave structure and this was the case in this study (e.g., Long, 1953). During RF#3 (flight with the trapped lee waves), ice formation and snow growth was observed by the WCR associated with regions of strong upward vertical motion (Figure 29). Meanwhile, during RF#5 (flight with the traditional cap cloud), no ice formation or snow growth was observed to the lee of the barrier due to the much weaker vertical velocities in the lee waves. A

comparison between upwind and downwind microphysics for both wave flights was inconclusive due to sampling occurring at cloud top and the varying lee wave structure.

Due to the UWKA sampling location at cloud top during both of the wave cases, a meaningful comparison between mountaintop and upwind microphysics is difficult to assess. However, consistent with the comparison between the convective cases, an increase in percent difference was observed for crystals smaller than 200μm. The increase in percent difference for small crystals supports the observations made by Rogers and Vali (1987) and shows that this phenomenon occurs for different cloud types.

Section 4.3: Hybrid Cases

WCR

Both hybrid cases are highlighted by very deep cloud decks and evidence of the seeder-feeder process (e.g., Bergeron 1965; Browning, 1980; Carruthers and Choularton, 1983; Reinking et al., 2000). During the seeder-feeder process, ice formed in the upper-level frontal cloud (seeder cloud) falls through the orographically-enhanced mixed-phase cloud (feeder cloud) where riming occurs and enhances the water content of the snow. For narrow mountain ranges like the Park Range, the seeder-feeder process has been identified as one of the most effective ways of orographically enhancing precipitation (e.g., Zängl, 2006). Figure 39a shows the seeder-feeder process as observed from the WCR during RF#1. Pockets of reflectivity above the aircraft can be seen falling into the liquid cloud at or just below the UWKA flight level. These fall-out streaks are more easily seen just downwind of the barrier where descending motion reduces the amount of liquid present in the cloud. The seeder-feeder process also appears to be occurring during RF#9 with ice forming at the highest levels of the clouds (see Figure

40a). However, unlike RF#1, much less liquid appears to be present in the cloud with a much weaker attenuation of the WCL (Figure 40c). Additionally, WCR-retrieved vertical velocities show a high elevation turbulent zone just below flight level and deep subsidence over the leeward slope (Figure 40b). There is also a very shallow cloud layer upwind of the barrier (Figure 40a). The cellular nature of this low-level cloud is consistent with observations of fog (e.g., Uematsu et al. 2005) and not an artifact of the radar.

BBSS

Soundings taken during both research flights are surprisingly consistent with profiles of $\mathbf{M_m}$ shown in Figure 41c. During RF#9, $\mathbf{M_m}$ is at or below unity from 2800 km and above. The low-level blocking and sharp increase in static stability (shown in Figure 41b) might be responsible for the shallow fog layer observed from the WCR in Figure27a. During RF#1, $\mathbf{M_m}$ predicts a deeper layer of blocking with unity achieved above the mountaintop level at 3500 meters. However, little blocking is observed in the WCR-calculated vertical velocities with only minimal form drag observed on the leeward slope of the barrier. It is likely that the blocking signal in the WCR reflectivity is overcome by the extremely efficient seeder-feeder process and the copious amount of moisture associated with this system. As previously mentioned, several studies have shown that moisture can drastically reduce the amplitude of lee wave formation (e.g., Smith, 1989).

Modeling Results:

Modeling was done for RF#1 due to its higher moisture content and more complicated cloud structure observed during the flight. A very strong jet streak at 300 hPa dropped south over the Park Range during the morning of the flight with SPL located underneath the center of the exit region by the middle of the flight (Figure 42). A 700 hPa trough began deepening over central Utah in response to the upper-level jet with increasing southwesterly flow impacting the Park Range before moving east and

producing a convergence zone upwind of SPL (Figure 43). Based on the location of the Park Range relative to the 700 hPa trough and the presence of a maximum in absolute vorticity at 500 hPa (Figure 44) just upwind of SPL, bands of embedded heavy precipitation are expected associated with enhanced lift. Coinciding WCR images support the model output with the presence of a narrow band of heavy precipitation crossing the Park Range (Figure 45). The model-derived 700 hPa vertical velocity fields also support the presence of banding with strong couplets of upward and downward motion (Figure 46).

The model-derived sounding supports the observed sounding but is faster with the U-component of the wind speed above 3km ASL (Figure 47a) and slightly stronger with the static stability between 3.3km and 4.6km ASL (Figure 47b). The result is a similar profile of $\mathbf{M_m}$ above 3.5 km ASL (Figure 47c) and a much stronger $\mathbf{M_m}$ in the model below 2.8 km ASL due to the low wind speed of the model below that level. The differences in the low-level wind speed are likely due to the model over-estimating the effect of shadowing of the Flat Tops upstream of Steamboat Springs during southwesterly flow. Meanwhile, the difference above 3km ASL is due to the drift of the actual sounding downstream as the model produces a sharp gradient in the magnitude of the southwesterly flow immediately northeast of the Park Range at and above the 700 hPa level (Figure 43).

The comparison between the UWKA average cross-barrier flight legs and the model-derived average cross-barrier LWC and vertical velocity fields at the same altitude help to validate the model (Figure 48). However, the model-derived vertical velocity field is slightly out of phase with the observations upwind of the barrier and much weaker to the lee of the barrier (Figure 48a). At the same time, the maxima in model-derived LWC are collocated just downwind of the maximum in the vertical velocity field (Figure 48b). The observed LWC shows much less dependence on the fluctuations of vertical velocity upwind of the barrier and has much less LWC to the lee of the barrier even with stronger ascent. The difference to the lee of the barrier is likely due to the conversion of LWC to ice due

to the enhanced ice mass falling from the seeder cloud observed in Figure 26a. Meanwhile, the coinciding cross-section of model-derived IWC shows no ice above the region of LWC, suggesting the lack of a seeder cloud (Figure 49). Even with the unrealistic distribution of ice over the Park Range, the model supports the observations of a deep synoptic system with ample spillover and minimal form drag consistent with $\mathbf{M_m}$.

Average Microphysics

Due to the depth of both of the hybrid systems, multiple flight level legs were averaged and compared. At the lowest flight level (4400 or 4600 meters) comparisons of leg-averaged vertical motion, liquid water content, ice crystal concentrations and ice crystal mean weighted diameter are shown in Figure 50 for both flights. Vertical motion is collocated during both flights with a maximum in vertical motion observed approximately 10 km upwind. A secondary collocated maximum is observed about 25km upwind but is much weaker during RF#9. Weak form drag is evident to the lee of the crest as predicted from $\mathbf{M_m}$ and observed by the WCR. The minimum in vertical velocity is collocated approximately 5 km downwind of the crest before the flow recovers to roughly 0.5m/s.

Unlike the consistent vertical velocities in both cases, the LWC is significantly different. RF#9 has almost no LWC observed at flight level and this is confirmed by the WCL. During RF#1, the LWC is much higher, also consistent with the WCL. A maximum of 0.25 g/m^3 is observed about 20km upwind of the crest and just downwind of the upwind maximum in vertical velocity. LWC slowly decreases from this maximum until just downwind of the crest when it plummets to 0 g/m^3 in the region of form drag. Farther downwind, the LWC recovers to approximately 0.06 g/m^3 before dropping off again. This resurgence of LWC is likely due to the recovery of weak upward motion in the region.

Large discrepancies exist between the 2 flights when ice crystal concentrations and MWD are compared. A 300% surge in ice concentration is observed far upwind of the crest during RF#1. This spike is likely associated with the precipitation rate of the seeder cloud as a similar spike in concentration is observed in the same region at the 5200 meter level (see Figure 51c). After the apparent spike, crystal concentrations level off at around 5 L^{-1}. MWD values continue to slowly increase towards the crest until they drop off in the region of form drag. This is likely due to smaller crystals from aloft being dragged to flight level or sublimation of those crystals. Downwind of the region of form drag, the MWD recovers, consistent with vertical mixing of the crystals rather than sublimation. During RF#9, a steady increase in crystal concentration and MWD is observed as the aircraft approaches the barrier. Over the leeward slope of the barrier, the crystal concentration and MWD slowly decrease. A slight recovery in crystal concentration is observed further downwind but no real change is observed in the MWD, which is surprising as the vertical motions in both cases are similar. This suggests that the sublimation rate is higher during this flight than during RF#1, which is supported by the lack of LWC.

To better understand the vertical structure of the cloud during each flight, the vertical motion, LWC, ice crystal concentration and MWD are plotted in Figure 51 for RF#1 and in Figure 52 for RF#9. Above the lowest flight level, a very similar story emerges during RF#1. Vertical velocities change very little with height, indicative of the lack of tilting associated within the terrain-induced waves (Figure 51a). The maximum in LWC is shifted downstream towards the crest as the altitude increases. Ice crystal concentrations generally decrease with height with the exception of downwind of the crest at the 5200m flight level. The decreasing crystal concentrations are counterintuitive as ice nucleation is expected to be more efficient at lower temperatures, and in this case, at higher locations in the cloud (e.g., Hoose and Mohler, 2012). However, this may be an artifact caused by removal of crystals smaller than 75 μm from the analysis. Freshly-nucleated crystals are expected to be small. Thus, relatively fewer

crystals larger than 75 µm are expected at higher levels in the cloud. The averages of MWD support this with a continuous decrease in MWD with height. The trend in MWD is consistent with snow growth mechanisms as crystals are expected to continue to grow as they fall through the cloud (e.g. Pruppacher and Klett, 1997).

For RF#9, a slight upwind tilt appears to occur at the 6000m flight level, but this could also simply be due to the evolution of the cloud system with time (Figure 52a). Very little LWC is present at all flight levels, with a general decrease with altitude and the maximum occurring near SPL. At the 6000m flight level, LWC appears to be higher than at the other levels, and this is likely due to small, freshly nucleated ice crystals (Figure 52b). Ice crystal concentrations increase with height while the MWD decreases, which is consistent with snow growth and ice nucleation processes (e.g., Lo and Passarelli, 1982).

Average upwind and downwind crystal size distribution comparisons between the two flights below 4700 meters show very little similarity, as shown in Figure 26. During RF#1, there are more crystals observed upwind of the crest than downwind at all sizes. Meanwhile, during RF#9, there are slightly more small crystals observed on the leeward slope and slightly more 500 to 1550 µm crystals observed on the windward slope. The relative increase in large crystals upwind of the crest is likely due to sublimation to the lee of the barrier.

UWKA and SPL comparisons

During both flights, there are instances when the trajectory model appears to work well but also when it doesn't. Figure 53 shows an example of when the trajectories worked well during RF#9. As shown in Figure 53, there were consistently more small crystals observed at SPL than aloft. These findings are inconsistent with ice nucleation theory and snow growth processes as more IN are activated

at colder temperatures which occur higher in the cloud. However, they are consistent with observations in the convective and wave cases and with observations by Rogers and Vali (1987), who found higher concentrations of small crystals at the mountaintop than aloft.

Discussion

Both of the hybrid cases were associated with synoptic scale systems and were enhanced by jet-induced banding and the seeder-feeder process. $\mathbf{M_m}$ is unable to predict the presence of banding or the seeder-feeder enhancement. However, it was capable of predicting the terrain-induced enhancement observed for these large scale systems. Both cases featured $\mathbf{M_m}$ values close to unity at mountaintop and above. Meanwhile, $\mathbf{M_m}$ predicted weak low-level blocking below mountaintop, consistent with the observed low-level fog during RF#9.

Consistent with the other case types, the profiles of vertical velocity were remarkably consistent between the hybrid cases. Both cases featured the presence of form drag to the lee of the barrier and lacked lee waves. In both cases, the mountaintop value of $\mathbf{M_m}$ near unity correctly predicted the presence of form drag. Meanwhile, the expected lee wave formation due to low-level blocking was likely reduced due to the abundant moisture present in both cases (e.g., Smith, 1989). Unlike the profiles of vertical velocity, the profiles of LWC varied dramatically between the two cases. During RF#1, LWC was observed throughout the cloud while during RF#9, no LWC was observed at flight-level. However, just below flight-level and collocated with a turbulent layer (apparent from the WCR-derived vertical velocities), the WCL indicated the presence of LWC during RF#9. The profiles of ice crystal concentrations were consistent during both flights except in a region 25 km upwind of the barrier during RF#1, where banding produced much higher crystal concentrations than elsewhere over the barrier.

The vertical profiles of crystal MWD support snow growth processes in both cases, with increasing MWD with decreasing altitude (Lo and Passarelli, 1982).

Comparisons between the upwind and downwind flight-level crystal concentrations showed higher crystal concentrations upwind of the barrier at all sizes during RF#1 and for crystals larger than 400 microns during RF#9. These results are consistent with previous studies that found enhanced precipitation upwind of a barrier when $\mathbf{M_m}$ was near or larger than unity (e.g., Sinclair et al., 1997; Colle, 2004). The feasibility of comparing upwind and mountaintop microphysics was inconclusive due to the complex structural features. However, consistent with the comparison between the convective and wave cases, an increase in percent difference was observed for crystals smaller than 200μm. The enhanced concentrations of small crystals in the hybrid case further support the observations of Rogers and Vali (1987).

Although the profiles of vertical velocity were remarkably consistent in the hybrid cases, the profiles of LWC and crystal concentrations differed drastically. The large differences in LWC and crystal concentrations between the hybrid cases stemmed from synoptic scale differences, jet enhanced banding and the seeder-feeder process, all of which $\mathbf{M_m}$ was incapable of predicting. However, due to the consistency in the vertical velocity and $\mathbf{M_m}$ in both cases, $\mathbf{M_m}$ appears to be a good predictor of the flow over complex terrain in deep synoptic-scale systems (e.g., Kaplan et al., 2012). Due to the complexities of banding and the varying efficiencies of the seeder-feeder process, comparing upwind and mountaintop microphysics was inconclusive. However, as in the convective and wave cloud cases, a consistent increase in small crystal concentration was observed at mountaintop. This suggests that the ice nucleation mechanism producing the small crystals at mountaintop is more efficient than the ice nucleation processes occurring in the seeder cloud.

Section 4.4: Enhanced Ice Crystal Concentrations at SPL

Due to the complexity of the upstream cloud structures between the UWKA and SPL, average crystal size distributions for each flight when the UWKA was below 4700 meters and upwind of SPL are compared to average PSDs at SPL for the same time periods. When comparing the convective, wave and hybrid flights, no real similarities arise except for a consistent spike in small crystal (75-200 μm) concentration at SPL, as is seen in Figure 28. This increase is consistent with the results of the trajectory analyses discussed previously and with the findings of Rogers and Vali (1987).

Due to SPL's location on a snow-covered surface, the potential for blowing snow could be large. Previous studies have shown a relationship between wind speed and crystal concentration (e.g., Schmidt, 1982). Figure 54 shows the relationship between wind speed at SPL and the concentration of crystals between 75 and 200 μm (Figure 54a) and for crystals between 225 and 1550 μm (Figure 54b). No relationship exists in either case, with r^2 values of 0.045 and 0.054, respectively. However, Schmidt (1982) and Gordon and Taylor (2009) found that blowing snow often traveled at the same velocity as the wind speed, making it difficult to discriminate blowing from falling snow and obscuring any relationship between crystal concentration and wind speed. Therefore, the swinging nature of the probe mount was used to identify periods when the flow was more turbulent (e.g., had rapid variations in both speed and direction) and when more crystals were likely to have been lofted from the snow surface. To determine the intensity of the gustiness, the ratio of the v- to u-component of the wind speed measured with the sonic anemometer on the probe vane were used. If there was a wind effect, small crystal concentrations should be higher for all measurements than for the subset of measurements with a low v/u ratio. Figure 55 shows that there is no consistent effect on the crystal size distributions when the v-

component is less than 30% of the u-component. This further supports the conclusion that the enhanced crystal concentrations observed at mountaintop were not an artifact of blowing snow, consistent with the findings of Rogers and Vali (1982).

Previous studies in mixed-phase clouds have identified a relationship between the width of the cloud droplet spectrum and ice crystal concentration (e.g., Hobbs and Rangno, 1985 hereafter referred to as HR85; Rangno and Hobbs, 2001; Lance et al., 2011). To quantify the broadness of the cloud droplet spectrum, HR85 defined a threshold diameter ($\mathbf{D_t}$) for a spectrum such that the cumulative concentration of droplets with diameters >= $\mathbf{D_t}$ is 3 cm^{-3}. To determine if such a relationship can explain the high small crystal concentrations at the surface, the average $\mathbf{D_t}$ is compared with the average small crystal concentration (75-200 μm) during the case study periods when the KA was over the Park range and when cloud droplet concentrations were higher than 3 cm^{-3}. To bolster the number of sample periods used in the comparison, sample periods from IFRACS are incorporated into the analysis. Each data point in the comparison represents between 30 and 120 minutes of measurements. The results shown in Figure 56 don't show much of a relationship until the ambient temperature during the sample periods is identified. Figure 56 suggests that there is a relationship between $\mathbf{D_t}$ and crystal concentration below -8^{o}C but that no such relationship exists at warmer temperatures. This temperature dependence suggests that the elevated crystal concentration at the surface is not a product of the Hallett-Mossop Process (HMP; e.g.,Hallett and Mossop, 1974), which has been shown to occur between -3 and -8^{o}C. In addition, enhancement of crystal concentration from the HMP would produce an increase in concentration on the order of 3 to 4 orders of magnitude, which is far greater than the observed difference between crystal concentrations at the surface and aloft. This is especially true since there is an abundance of potential riming sites near the mountain surface (e.g., the snow surface, trees, rocks).

Two other modes of ice multiplication, mechanical fracturing and droplet freezing (e.g., Pruppacher and Klett, 1997), are much harder to assess in this study. Mechanical fracturing is much more likely to occur when crystals form at temperatures between -12 and -18^{o}C (the dendritic growth region). HR85 estimated that mechanical fracturing could increase crystal concentrations by a factor of 5 in maritime stratus clouds, which is close to the observed enhancement of small crystals at SPL. However, the difference between the UWKA and SPL small crystal concentration is unrelated to whether the UWKA was sampling in the dendritic growth region or not. This suggests that mechanical fracturing is not responsible for the observed enhanced crystal concentrations at SPL. Droplet freezing has been observed to occur for drops larger than 50 µm (e.g., Mason and Maybank, 1960; Hobbs and Alkezweeny, 1968; Pruppacher and Klett, 1997; Rangno and Hobbs, 2001). Pruppacher and Klett (1997) reported that droplet freezing could multiply ice concentration by a factor of 2 and rarely by as much as 5. The observed difference in small crystal concentrations at the lab and on the UWKA falls within that range. The SPP100 at SPL sampled particles up to 47.5 µm in diameter, making it impossible to determine whether cloud droplets larger than 50 µm were present. Additionally, habit identification from the CIP at that size is impossible due to the resolution (25 µm) of the probe. However, droplets larger than 50 µm are only likely to occur in deep updrafts, yet a similar increase in small crystal concentration was observed in the shallow wave cases (RF#3 and 5) (see Figure 28). Therefore, large-droplet freezing is unlikely the cause of high concentrations of small crystals at the surface.

Another possible explanation for the relatively high surface small crystal concentrations is liquid-dependent ice nucleation such as immersion, condensation, and contact freezing. In the case of immersion freezing, small droplets have been shown to freeze less readily than larger drops due to higher solute concentrations and the smaller volume of the drops (e.g., Bertram et al., 2000; Diehl et al. 2006; de Boer et al., 2010). However, the impact of solute concentration on freezing point depression

has been found only to occur for drop diameters of around 10 μm or smaller (Pruppacher and Klett, 1997; Diehl et al., 2006) which is typically exceeded in the mixed-phase clouds observed at SPL (e.g., Borys et al., 2003). Modeling sensitivity tests done by Deihl et al. (2006) confirmed that there was no impact on immersion freezing efficiency when cloud droplets exceeded 10 μm in diameter. Thus, there is no reason for ice production by immersion freezing to be related to the droplet spectrum width ($\mathbf{D_t}$) when the drops are larger than 10 μm. Immersion freezing has also been shown to have a strong dependence on temperatures (e.g., Diehl et al., 2006). Very few non-bio-aerosol particles have been observed to nucleate in the immersion mode at temperatures warmer than -7^{o}C (e.g., Hoose and Mohler, 2012). This suggests that the onset of immersion freezing for certain aerosols may partially explain the temperature dependence observed in this study. However, no relationship is observed between the temperature at SPL when it is below -7^{o}C and the high small crystal concentrations (not shown). Therefore, it is unlikely that immersion freezing is responsible for the elevated crystal concentrations at SPL. Condensation freezing is also unlikely, as De Boer et al., (2011) found no evidence for its occurrence in Arctic mixed-phase stratus clouds at temperatures similar to those observed at SPL.

Consistent with the observations from this study and previous work done in mixed-phase clouds (e.g., HR85; Rangno and Hobbs, 1998; Hobbs and Rangno, 2001; Korolev et al., 2003; Lance et al., 2011), contact freezing is a likely candidate for the relationship between small crystal concentrations and cloud droplet spectral width ($\mathbf{D_t}$) at SPL. The collision efficiency between sub-micron aerosols (including ice nuclei) and cloud droplets has been shown to increase with cloud droplet size through Brownian motion (e.g., HR85; Diehl et al., 2006; Rzesanke et al., 2011). This would explain the apparent relationship between $\mathbf{D_t}$ and small crystal concentration at SPL, especially since higher aerosol concentrations are found near the surface. However, studies done by Ladino et al., (2011) and Bunker et al., (2012) found a

much weaker relationship between freezing efficiency and drop size. The threshold temperature of -7^{o}C, with little dependence below this value, can also be explained by contact nucleation, as no relationship between temperature and contact nucleation efficiency has been observed once the nucleating temperature of an IN is reached (e.g., Diehl et al., 2006). Additionally, contact nucleation could be enhanced under conditions where orographic forcing supplies ice nuclei into the cloud. A rapid depletion of IN is expected in steady state stratiform clouds (e.g., de Boer et al., 2010). This could help explain the enhancement of small crystals at SPL compared with the UWKA where conditions were usually more stratiform. During RF#12, when deep convection was observed, much less of a difference between SPL and the UWKA was observed (see Figure 28). This potentially supports the need for updrafts to introduce ice nuclei into the cloud or they would rapidly deplete. Due to the uncertainty in contact freezing efficiency as a function of cloud droplet size, more research is required (e.g., Hoose and Mohler, 2012) to determine if it is the mechanism responsible for the observed relationship between the $\mathbf{D_t}$ and small crystal concentrations at SPL.

Chapter 5: Summary and Conclusions

In this study, *in-situ* and remote sensing cloud microphysical measurements aboard the University of Wyoming King Air (UWKA) were used to study the distribution of cloud microphysical properties across the Park Range of the Colorado Rockies under varying profiles of the nondimensional mountain height number ($\mathbf{M_m}$). Concurrent ground based cloud microphysical measurements at Storm Peak Laboratory (SPL) were used to measure cloud microphysics near cloud base below which the UWKA is prohibited from operating. Cross-barrier flight legs from 29 flights were identified with a total of seven flights selected and binned into three categories: wave, convective and hybrid, based on the observed cloud structure retrieved from the Wyoming Cloud Radar. Cross-barrier average profiles of vertical velocity, liquid water content, ice crystal concentration and mean concentration-weighted crystal diameter were calculated for each flight based on altitude. The cross-barrier averages were compared to vertical profiles of $\mathbf{M_m}$ retrieved from upwind balloon-bourne soundings to evaluate relationships with cloud microphysical distributions. High resolution modeling was performed for a flight from each category in order to validate observed relationships between $\mathbf{M_m}$ and the cloud microphysics across the barrier.

Consistent with theory and previous studies, $\mathbf{M_m}$ was found to be a good predictor of the cloud structure over the barrier obtained from the observations and the modeling. In cases where $\mathbf{M_m}$ was below unity at mountaintop and above, much higher crystal concentrations were observed downwind of the crest at flight level *in-situ* and with the Wyoming Cloud Radar. Furthermore, in all three of the more unstable convective cases, higher flight level crystal concentrations were observed on the leeward slope than on the windward slope. However, form drag was still observed to the lee of the barrier but was much less consistent amongst the convective flights than the flights in the other categories. Meanwhile,

when $\mathbf{M_m}$ was greater than unity at the mountaintop level and below, the Wyoming Cloud Radar showed the presence of lee waves and a rapid decrease in spillover precipitation downwind of the barrier. However, the expected presence of wave breaking was never observed. The amount of moisture present in each case likely dampened the waves and prevented them from breaking. In both of the wave flights, a consistent increase in the period of the flight level vertical velocity field was observed. The deeper hybrid cases had similar $\mathbf{M_m}$ to the convective cases but were more stable, showed less dependence on $\mathbf{M_m}$ and more dependence on the available moisture and the efficiency of precipitation processes. However, the magnitude and location of the vertical motion was very consistent between the two hybrid flights examined. Overall, $\mathbf{M_m}$ was a good indicator of the terrain-induced flow over the barrier, which helped to constrain the flight level microphysics.

Comparisons between upwind UWKA and SPL mountaintop crystal size distributions showed a consistent enhancement of small crystals at SPL, regardless of $\mathbf{M_m}$, and confirmed previous observations of enhanced ice crystal concentrations near snow- covered surfaces. The possibility of contamination from blowing snow was explored by comparing both wind speed and gustiness to crystal concentration. No relationship was found for either variable, indicating that blowing snow was not a likely cause for the observed enhancement. In order to further examine the source of the anomalously high surface crystal concentration, additional data from the IFRACS field campaign at Storm Peak Laboratory were added to the analysis. Ice crystal concentration showed a strong dependence on the cloud droplet size distribution and an upper threshold temperature of -8^{o}C. These results suggest the importance of a liquid-dependent ice nucleation process occurring near the cloud base in mixed-phase orographic clouds. The Hallett-Mossop ice multiplication process is unlikely to occur at the colder temperatures at SPL during winter. Based on the relationship between the cloud droplet size distribution and more importantly, its width, contact nucleation is a likely mechanism for the anomalously high crystal

concentrations at SPL. However, contact nucleation is one of the most uncertain nucleation mechanisms and further work is needed to determine the role of droplet size on collision efficiency before this mechanism can be confirmed. Additionally, potential contamination from blowing snow, limitations in cloud probe resolution and the resulting uncertainty in hydrometeor phase must be addressed in order to determine the exact origin of the small crystals.

Works Cited

Ansmann, A., M. Tesche, P. Seifert, D. Althausen, R. Engelmann, J. Fruntke, U. Wandinger, I. Mattis, *and* D. Müller,2009: Evolution of the ice phase in tropical altocumulus: SAMUM lidar observations over Cape Verde, *J. Geophys. Res*., **114**, D17208, doi:10.1029/2008JD011659.

Baines, P. G. and R. B. Smith, 1993: Upstream stagnation points in stratified flow past obstacles. *Dyn.Atmos.Oceans* **18**, 105-113

Baker, B. A., and R. P. Lawson, 2006: In situ observations of the microphysical properties of wave, cirrus, and anvil clouds. PartI: Wave clouds. J. Atmos. Sci., **63**, 3160–3185.

Barcilon, A., and D. Fitzjarald, 1985: A nonlinear steady model for moist hydrostatic mountain waves. J.Atmos. Sci.,**42**,58–67

Baumgardner, D.,1983: An analysis and comparison of five water droplet measuring instruments, J Appl Meteorol, **22**, 891-910.

___, and A. Korolev, 1997: Airspeed corrections for optical array probe sample volumes, J Atmos Ocean Tech, **14**, 1224-1229.

Bergeron, T., 1965: On the low-level redistribution of atmospheric water caused by orography.Proc. Int. Conf. on Cloud Physics,Tokyo, Japan, IAMAP/WMO, 96–100

Bertram, A. K., T. Koop, and M.J. Molina, 2000: Ice formation in $(NH_4)_2SO_4$-H_2O particles. *J. Phys. Chem. A*., **140**, 584-588.

Borys, R. D., D. H. Lowenthal, and D. L. Mitchell, 2000: The relationships among cloud microphysics, chemistry, and precipitation rate in cold mountain clouds. *Atmos. Environ*., **34**, 2593–2602.

___,M.A. Wetzel, S. A. Cohn, and W. O. J. Brown, 2003: Mountaintop and radar measurements of anthropogenic aerosol effects on snow growth and snowfall rate. *Geophys. Res. Lett*., **30**, 1538, doi:10.1029/2002GL016855.

Browning, K. A., 1980: Structure, mechanism, and prediction of orographically enhanced rain in Britain. Orographic Effects in Planetary Flows,R. Hide and P. W. White, Eds., GARP Publication Series, Vol. **23**, WMO, 85–114.

Bunker, K, W., S. China, C. Mazzoleni, A. Kostinski, and W. Cantrell, 2012: Measurements of ice nucleation by mineral dusts in the contact mode. *Atmos. Chem. Phys. Discuss*., **12**, 20291-20309, doi: 10.5194/acpd-12-20291-2012.

Burakowski, E. and M. Magnusson. 2012: Climate Impacts on the Winter Tourism Economy in

the United States.National Resources Defense Council, (December).

Carruthers, D. J., and T. W. Choularton., 1983: A model of the feeder-seeder mechanism of orographic rain including stratification and wind drift effects. *Quart. J. Roy. Meteorol. Soc*., **109**, 575-588.

Cerni, T.1983: Determination of the size and concentration of cloud drops with an fssp, J Clim Appl Meteorol, **22**, 1346-1355.

Choularton, T. W., and S. J. Perry, 1986: A model of the orographic enhancement of snowfall by the seeder-feeder mechanism. Quart .J. Roy. Meteorol. Soc., 112, 335-345.

Cooper, W. A., 1978: Precipitation mechanisms in summertime storms in the Montana HIPLEX area. *Preprints Conf. on Cloud Physics and Atmospheric Electricity*, Issaquah, *Amer. Metero. Soc*. 347-350

Cohen, M., J. Christian-Smith, J. Berggren, 2013: Water to Supply the Land: Irrigated Agriculture in the Colorado River Basin. *Pac. Inst.* (May)

Collins, W. D., P. J. Rasch, B. A. Boville, J. J. Hack, J. R. McCaa, D. L. Williamson, J. T. Kiehl, B. Briegleb, C. Bitz, S. J. Lin, M. Zhang, Y. Dai, 2004: Description of the NCAR community atmosphere model (CAM 3.0). *Tech. Rep. NCAR*/TN-464+ STR.

Colle, B., 2004: Sensitivity of orographic precipitation to changing ambient conditions and terrain geometries: An idealized modeling perspective. *J. Atmos. Sci.,* **61,** 588–606.

Davis, S. M., Hallar, A. G., Avallone, L. M., and Engblom, W.2007: Measurement of total water with a tunable-diode laser hygrometer: Inlet analysis, calibration procedure, and ice water content determination, J Atmos Ocean Tech, **24**, 463-475, 10.1175/JTECH1975.1.

de Boer, G., Hashino, T., and Tripoli, G.J., 2010: Ice nucleation through immersion freezing in mixed-phase stratiform clouds: Theory and numerical simulations. *Atmos. Res*. **96**, 315-324

___, Morrison, H., Shupe, M. D., and Hildner, R. 2011: Evidence of liquid dependent ice nucleation in high-latitude stratiform clouds from surface remote sensors, *Geophys. Res. Lett*., **38**, L01803, doi:10.1029/2010GL046016

Diehl, K., Simmel, M., and Wurzler, S. 2006: Numerical sensitivity studies on the impact of aerosol properties and drop freezing modes on the glaciation, microphysics and dynamics of clouds. *J. Geophys. Res*., **111**, D07202, doi:10.1029/2005JD005884

Dorsi, S.W.,2013: Airborne and surface-level in situ observation of wintertime clouds in the Southern Rockies. (Doctoral Dissertation). Dissertation Abstracts International,Volume:74-09(E),Section:B

Doyle, J., and Smith, 2003: Mountain waves of the Hohe Tauern: Influence of upstream diabatic effects,

Quart. J. roy. Meteorol. Soc., **129**, 799-823

Durran, D., and J. Klemp, 1982: On the effects of moisture on the Brunt–Väisälä frequency. J. Atmos. Sci., 39, 2152–2158.

___, 1990: Atmospheric Processes over Complex Terrain. *Meteor. Monogr. Amer. Meteor. Soc*., **45**, 394

____, 2003: Lee waves and mountain waves. Encyclopedia of Atmospheric Science, Elsevier Science Ltd., 1161–1170

Eidhammer, T., P. J. DeMott, and S. M. Kreidenweis, 2010: Ice initiation by aerosol particles: Measured and predicted ice nuclei concentrations versus measured ice crystal concentrations in an orographic wave cloud. J. Atmos. Sci., 67, 2437–2450.

Feng, D., and L. 0. Grant, 1982: Correlation of snow crystal habit, number flux and snowfall intensity from ground observations. Preprints, Conf. on Cloud Physics, Amer. Meteor. Soc., Boston, Massachusetts, 485-487.

Field, P. R., 1999: Aircraft observations of ice crystal evolution in an altostratus cloud. *J. Atmos. Sci.,* **56,** 1925–1941.

___, 2000: Bimodal ice spectra in frontal clouds. *Quart. J. Roy.Meteor. Soc.,* **126,** 379–392.

___, A. J. Heymsfield, B. J. Shipway, P. J. Demott, K. A. Pratt, D. C. Rogers, J. Stith, and K. A. Prather, 2001: Ice nucleation in orographic wave clouds: Measurements made during INTACC. Quart.J. Roy. Meteor. Soc., **127**, 1493–1512.

___,Wood, R., Brown, P., Kaye, P., Hirst, E., Greenaway, R., and Smith, J.,2003: Ice particle interarrival times measured with a fast FSSP, J Atmos Ocean Tech, **20**, 249-261.

___,Heymsfield, A. J., and Bansemer, A.,2003: Shattering and particle interarrival times measured by optical array probes in ice clouds, J Atmos Ocean Tech, **23**, 1357-1371.

___, A. J. Heymsfield, B. J. Shipway, P. J. Demott, K. A. Pratt, D. C. Rogers, J. Stith, and K. A. Prather, 2012: Ice in Clouds Experiment-Layer Clouds. PartII: Testing Characteristics of Heterogeneous Ice Formation in Lee Wave Clouds.J.Atmos.Sci.,**69,**1066-1078.

Fukuta, N. and T. Takahashi, 1999: The growth of atmospheric ice crystals –A summary of findings in vertical supercooled cloud tunnel studies. *J. Atmos. Sci*., **56(12)**, 1963-1979.

Gardiner, B., and Hallett, J.,1985: Degradation of in-cloud forward scattering spectrometer probe measurements in the presence of ice particles, J Atmos Ocean Tech.

Garvert, M. F., B. Smull, and C. Mass, 2007: Multiscale mountain waves influencing a major orographic precipitation event.J. Atmos. Sci., **64**, 711–737.

Geerts, B., Q. Miao, and Y. Yang, 2011: Boundary-layer turbulence and orographic precipitation growth

in cold clouds: evidence from profiling airborne radar data.J. Atmos. Sci.,**68**,2344-2365.

Gerber, H., B. Arends, and A. Ackerman, 1994: New microphysics sensor for aircraft use, Atmos Res, **31**, 235-252.

___, H., G. Frick, and A. Rodi, 1999: Ground-based FSSP and PVM measurements of liquid water content, J Atmos Ocean Tech, **16**, 1143-1149.

Givati, A., and D. Rosenfeld, 2004: Quantifying precipitation suppression due to air pollution. *J. Appl. Meteor*., **43**, 1038–1056.

Gordon, M. and Taylor, P.A. 2009, Measurements of blowing snow, part I: particle size distribution, velocity, number and mass flux at Churchill, Manitoba, Canada. *Cold Regions Science and Technology*. **55**, 63-74.

Graedel, T. E.*, and* J. P. Franey*, 1975:* Field measurements of submicron aerosol washout by snow*,* *Geophys. Res. Lett*.*,* **2***,* 325–328*.*

Grossman, P. A., and D. R. Durran, 1984: Interaction of low-level flow with the Western Ghat Mountains and offshore convection in the summer monsoon.Mon. Wea. Rev.,**112**,652–672.

Hallar, A., L. Avallone, R. Herman, B. Anderson, and A. Heymsfield, 2004: Measurements of ice water content in tropopause region arctic cirrus during the SAGE III Ozone Loss and Validation Experiment (SOLVE), J Geophys Res-Atmos, **109**, D17203,10.1029/2003JD004348.

Hallatt, J., and Mossop, S. C., 1974: Production of secondary particles during the riming process. *Nature*, **249**, 26-28.

Harimaya, T., and M. Sato, 1989: Measurement of the riming amount on snowflakes. *J. Fae. Sci., Hokkaido Univ., Ser. VII,* **8**, 355-366.

Heymsfield, A., 1972: Ice crystal terminal velocities*. J. Atmos. Sci.,***29**, 1348-1357.

___, and J.L. Parrish, 1978: A computational technique for increasing the effective sampling volume of the PMS 2-D particle size spectrometer. *Journal of Applied Meteorology 1989-2005 (After 2005 - Journal of Applied Meteorology and Climatology)*, **17**, 1566-1572, DOI: 10.1175/1520-0450(1978)017%3C1566:ACTFIT%3E2.0.CO;2.

___, Schmitt, C., and Bansemer, A., 2013: Ice cloud particle size distributions and pressure-dependent terminal velocities from in situ observations at temperatures from 0 to -86 C, *J.Atmos. Sci.,* **70**, 4123–4154.

Hill, F. F., 1983: The use of average annual rainfall to derive estimates of orographic enhancement of frontal rain over England and Wales for different wind directions.J. Climatol.,**3**,113–129.

Hindman, E. E., 1986: Characteristics of supercooled liquid water in clouds at mountaintops in the Colorado Rockies. *J. Climate Appl. Meteor*., **25**, 1271–1279.

Hobbs, P. V., and Rangno, A. L., 1985: Ice Particle Concentration in Clouds. *J. Atmos. Sci*., **42(23)**, 2523-2549

___, Alkezweeny, A.J., 1968: The fragmentation of freezing water droplets in free fall. *J. Atmos. Sci*., **25**, 881-888

Hoose, C. and Möhler, O.: Heterogeneous ice nucleation on atmospheric aerosols: a review of results from laboratory experiments, *Atmos. Chem. Phys.,* **12**, 9817-9854, doi:10.5194/acp-12-9817-, 2012

Hunt, C. R. and Snyder, W. H., 1980: Experiments on stably and neutrally stratified flow over a three-dimensional hill. *J.Fluid. Mech.* **96**, 671-704

James, T., A. Evans, E. Madly, C. Kelly, 2014: The Economic Importance of the Colorado River to the Basin Region. *ASU W.P Carey School of Business*, (December)

Janjic, Z. I., 1994: The step-mountain Eta coordinate model: Further developments of the convection, viscous sublayer, and turbulence closure schemes. *Mon. Wea. Rev.,* **122,** 927–945.

___,1996: The surface layer in the NCEP Eta Model, Eleventh Conference on Numerical Weather Prediction, Norfolk, VA, 19–23 August; Amer. Meteor. Soc., Boston, MA, 354–355.

___,2002: Nonsingular Implementation of the Mellor–Yamada Level 2.5 Scheme in the NCEP Meso model, NCEP Office Note, No. 437, 61 pp

Jiang, Q., 2003: Moist dynamics and orographic precipitation. Tellus, **55A**, 301–316.

Joe, P, and R. List, 1987: Testing and performance of two-dimensional optical array spectrometers with grayscale. *J. Atmos. Oceanic Technol*., **4**, 139-150

Kalina, M.F. and H. Puxbaum,1994: A study of the influence of riming of ice crystals on snow chemistry during different seasons in precipitating continental clouds., *Atmos. Environ*., **28**, pp. 3311–3328

Kaplan, Michael L., Ramesh K. Vellore, Phillip J. Marzette, John M. Lewis, 2012: The Role of Windward-Side Diabatic Heating in Sierra Nevada Spillover Precipitation. *J. Hydrometeor*, **13**, 1172–1194. *doi:* http://dx.doi.org/10.1175/JHM-D-11-06.1

King, W., Parkin, D., and Handsworth, R.,1978: Hot-wire liquid water device having fully calculable response characteristics, J Appl Meteorol, **17**, 1809-1813.

Knollenberg, R.G,1970: The optical array: An alternative to scattering or extinction for airborne particle size determination., J Appl Meteorol.

___,1981: Techniques for probing cloud microstructure, Clouds, Their Formation, Optical Properties and Effects,edited by: Hobbs, P., and Deepak, A., Academic Press,495 pp.

Korolev, A., Strapp, J., and Isaac, G.,1998: Evaluation of the accuracy of PMS Optical Array Probes, J.Atmos Ocean Tech, **15**, 708-720.

___, and Sussman, B.,2000: A technique for habit classification of cloud particles, J Atmos Ocean Tech, **17**, 1048-1057.

___, Isaac, G. A., Cober, S. G., Strapp, W., and Hallett, J., 2003: Microphysical characterization of mixed-phase clouds., *Q. J. R. Meteorol. Soc*., **129**, 39-65

___, Emery, E. F., Strapp, J. W., Cober, S. G., Isaac, G. A., Wasey, M., and Marcotte,D.,2011: Small Ice Particles in Tropospheric Clouds: Fact or Artifact? Airborne Icing Instrumentation Evaluation Experiment, B Am Meteorol Soc, **92**, 967-973, 10.1175/2010BAMS3141.1.

Ladino, L., Stetzer, O., Luond, F., Welti, A., and Lohmann, U., 2011: Contact freezing experiments of kaolinite particles with cloud droplets. *J. Geophys. Res*., **116**, D22202, doi:10.1029/2011JD015727.

___, Stetzer, O., and Lohmann, U., 2013: Contact freezing: a review, Atmos. Chem. Phys. Discuss., 13, 7811–7869, doi:10.5194/acpd-13-7811-2013.

Lance, S., Shupe, M. D., Feingold, G., Brock, C. A., Cozic, J., Holloway, J. S., Moore, R. H., Nenes, A., Schwarz, J. P., Spackman, J. R., Froyd, K. D., Murphy, D. M., Brioude, J., Cooper, O. R., Stohl, A., and Burkhart, J. F., 2011: Cloud condensation nuclei as a modulator of ice processes in Arctic mixed-phase clouds, *Atmos. Chem. Phys*., **11**, 8003–8015, doi:10.5194/acp-11-8003-2011

Lawson, R. P.,2011: Effects of ice particles shattering on optical cloud particle probes, Atmos Meas Tech Discuss, **4**, 939-968, 10.5194/amtd-4-939-2011.

Lo, K., and R. E. Passarelli, 1982: The growth of snow in winter storms: An airborne observational study. *J. Atmos. Sci.,* **39,** 697–706.

Lohmann, U., and Diehl, K., 2006: Sensitivity studies of the importance of dust ice nuclei for the indirect aerosol effect on stratiform mixed-phase clouds., *J. Atmos. Sci*., **63**, 968-982.

Long, R. R., 1953: Some aspects of stratified fluids, I. A theoretical investigation. *Tellus* **5**, 42-58

Lowenthal, D. H.*,* R. D. Borys*, and* M. A. Wetzel, 2002: Aerosol distributions and cloud interactions at a mountaintop laboratory*,* J. Geophys. Res.*,* **107*(*D18*), 4345, doi:*10.1029/2001JD002046

___,___, W. Cotton, S. Saleeby, S. A. Cohn, and W. J. Brown, 2011: The altitude of snow growth by riming and vapor deposition in mixed-phase orographic clouds. *Atmos. Environ*.,**45**,519–522.

Mason, B. J., and Maybank, J. 1960: *Quart. J. Roy. Meteor. Soc.,* **86**, 176

Matrosov, Sergey Y., Gerald G. Mace, Roger Marchand, Matthew D. Shupe, Anna G. Hallar, Ian B. McCubbin, 2012: Observations of Ice Crystal Habits with a Scanning Polarimetric W-Band Radar at Slant Linear Depolarization Ratio Mode. J. Atmos. Oceanic Technol., 29, 989-1008. doi: http://dx.doi.org/10.1175/JTECH-D-11-00131.1

Mitchell, D. L., R. Zhang, and R. L. Pitter, 1990: Mass dimensional relationships for ice particles and the influence of riming on snowfall rates*. J. Appl. Meteor*., **29**, 153–163.

___, 1996: Use of mass- and area-dimensional power laws for determining precipitation particle terminal velocities. *J. Atmos.Sci.,* **53,** 1710–1723.

Mlawer, E. J*.,* S. J. Taubman*,* P. D. Brown*,* M. J. Iacono*, and* S. A. Clough*.,*1997: Radiative transfer for inhomogeneous atmospheres: RRTM, a validated correlated-k model for the longwave*,* J. Geophys. Res*.,* **102*(*D14*)***,* 16663–16682*, doi:*10.1029/97JD00237.

Monin, A.S. and A.M. Obukhov, 1954: Basic laws of turbulent mixing in the surface layer of the atmosphere. Contrib. Geophys. Inst. Acad. Sci., USSR, **151**, 163–187 (in Russian)

Mossop, S. C., 1985: Secondary ice particle production during rime growth: The effect of drop size distribution and rimer velocity., *Q. J. R Mterorol. Soc*., **111**, 1113-1124.

Pandey, G. R., D. R. Cayan, and K. P. Georgakakos, 1999: Precipitation structure in the Sierra Nevada of California during winter.J. Geophys. Res.,**104**,12 019–12 030.

Peng, Y*.,* U. Lohmann*,* R. Leaitch*,* C. Banic*, and* M. Couture, 2002: The cloud albedo-cloud droplet effective radius relationship for clean and polluted clouds from RACE and FIRE.ACE*, J. Geophys. Res*., **107***(*D11*), 4106, doi:*10.1029/2000JD000281.

Pratt, K. A., Paul J. DeMott, Jeffrey R. French, Z. Wang, Douglas L. Westphal, Andrew J. Heymsfield, Cynthia H. Twohy, Anthony J. Prenni & Kimberly A. Prather,2009: In situ detection of biological particles in cloud ice-crystals. Nature Geoscience; DOI: 10.1038/ngeo521.

Pruppacher, H. R., and Klett, J. D., 1997: Microphysics of clouds and precipitation, 2nd Ed., Kluwer Academic Publishers, Boston. 954 pp.

Ralph, F. M., P. J. Neiman, T. L. Keller, D. Levinson, and L. Fedor, 1997:Observations, simulations and analysis of nonstationary trapped lee waves.J. Atmos. Sci.,54, 1308–1333.

Rangno, A. L., and Hobbs, P. V., 2001: Ice particles in stratiform clouds in the Arctic and possible

mechanisms for the production of high ice concentrations., *J. Geophys. Res*., **106(D14)**, 15065-15075.

Reinking, R. F., J. B. Snider, and J. L. Coen, 2000:Influence of storm-embedded orographic gravity waves on cloud liquid water and precipitation. *J. Appl. Meteor*., **39**, 733-759.

Rogers, D., and Vali, G.,1987: Ice crystal production by mountain surfaces, J Clim Appl Meteorol, 26, 1152-1168.

Rosenfeld, D., and A. Givati, 2006: Evidence of orographic precipitation suppression by air pollution-induced aerosols in the western United States. *J. Appl. Meteor. Climatol*., **45**, 893–911.

Rotunno R, Houze RA. 2007. Lessons on orographic precipitation from MAP. *Q. J. R. Meteorol. Soc*. **133**, 811 – 830

Rzesanke, D., Duft, D., and Leisner, T., 2011: Laboratory experiments on the microphysics of electrified cloud droplets, in: Climate And Weather of the Sun-Earth System (CAWSES): Highlights from a priority program, edited by Lubken, F.-J., Springer, Dordecht, The Netherlands, 2011

Thompson, G., P. R. Field, R. M. Rasmussen, and W. D. Hall, 2008: Explicit forecasts of winter recipitation using an improved bulk microphysics scheme. Part II: Implementation of a new snow parameterization.Mon. Wea. Rev.,**136**,5095–5115

Saleeby, S. M., and W. R. Cotton, D. Lowenthal, R. D. Borys, and M. A. Wetzel, 2009: Influence of cloud condensation nuclei on orographic snowfall.J. Appl. Meteor. Climatol.,**48**,903–922.

___,___, ___, Joe Messina, 2013: Aerosol Impacts on the Microphysical Growth Processes of Orographic Snowfall. *J. Appl. Meteor. Climatol.*, **52**, 834–852. doi: http://dx.doi.org/10.1175/JAMC-D-12-0193.1

Scorer, R. S., 1949: Theory of waves in the lee of mountains. *Quart. J. Roy. Meteor. Soc.,* **76**, 41-56

Schmidt, R. A. Jr., 1982: Properties of blowing snow. *Rev. Geophys. Space Phys*., **20**, 39-44

Shaw, R. A.,Durant, A. J., and Mi, Y., 2005: Heterogeneous surface crystallization observed in undercooled water., *J. Phys. Chem. Lett*., **109**, 9865-9868.

Sinclair, M.R., Wratt, D.S., Henderson, R., Gray, W.R., 1997: Factors affecting the distribution and spillover of precipitation in the Southern Alps of New Zealand — a case study. J. Appl. Meteorol. **36**, 428–442.

Skamarock, W. C., and Coauthors, 2008: A description of the Advanced Research WRF Version 3. NCAR Tech. Note NCAR/TN-4751 STR, 113 pp.

Smith, R. B. 1979: The influence of mountains on the atmosphere. *Adv. Geophys*. **21**, 87-230

___ 1989: Mountain-induced stagnation points in hydrostatic flow. *Tellus.* **41A**, 270-274

Smolarkiewicz, P. K. and Rotunno, R. 1990: Low Froude number flow past three-dimensional obstacles. PartII: Upwind flow reversal zone. *J.Atmos.Sci*. **47**, 1498-1511.

Strapp, J. W., F. Albers, A. Reuter, A. V. Korolev, U. Maixner,E. Rashke, and Z. Vukovic, 2001: Laboratory measurements of the response of a PMS OAP-2DC. J. Atmos. Oceanic.Technol., **18**, 1150–1170.

Twomey, S*.,* M. Piepgrass*,* and T. L. Wolfe, 1984*:* An assessment of the impact of pollution on global cloud albedo*, Tellus,* **36B***,* 356–366*.*

Uematsu, A., H. Hashiguchi, M. Teshiba, H. Tanaka, K. Hirashima, and S. Fukao, 2005: Moving cellular structure of fog echoes obtained with a millimeter-wave scanning Doppler radar at Kushiro. *J. Appl. Meteor*., **44**, 1260–1273.

Vali, G., M. K. Politovich, D. Baumgardner and W. A. Cooper, 1980: Conduct of cloud spectra measurements. Scientific Report1 to the Air Force Geophysics Laboratory, Contract No. AFGL-TR-79-0251.

___,___and___, 1981: Conduct of cloud spectra measurements.Final Report to the Air Force Geophysics Laboratory, Contract No. AFGL-TR-81-0122.

Wang, Z. et al., 2012: Single aircraft integration of remote sensing and in situ sampling for the study of cloud microphysics and dynamics. BAMS, **93**, 653-766. doi: 10.1175/BAMS-D-11-00044.1.

Wendisch, M., 1998:A quantitative comparison of ground-based FSSP and PVM measurements., *J. Atmos. Ocean. Tech*., **15**, 887-990.

___, S. Mertes, J, Heintzenberg, A. Wiedensohler, D. Schell, W. Wobrock, G. Frank, B. Matinsson, S. Fuzzi, G. Orsi, G. P. A. Kos, and A. Berner, 1998: Drop size distribution and LWC in Po Valley fog. *Contr. Atmos. Phys.*, **71**, 87-100.

___, Garrett, T., and Strapp, J.,2010: Wind tunnel tests of the airborne PVM-100A response to large droplets, J Atmos Ocean Tech, **19**, 1577.

Wood, R.,C. Bretherton, D. Leon, A. Clarke,P. Zuidema, G. Allen, and H. Coe, 2011: An aircraft case study of the spatial transition from closed to open mesoscale cellular convection over the southeast Pacific. *Atmos. Chem. Phys*., **11**, 2341–2370

Woods, C., M. T. Stoelinga, J. D. Locatelli, and P. V. Hobbs, 2005: Cloud structures and microphysical processes during the 13 December 2001 IMPROVE-2 event. *J. Atmos. Sci.,* **62,** 3493–3519.

Zängl, G., 2007: Interaction between dynamics and cloud microphysics in orographic precipitation

enhancement: A high-resolution modeling study of two north Alpine heavy precipitation events. Mon. Wea. Rev.,**135**, 2817–2840.

Figures and Tables

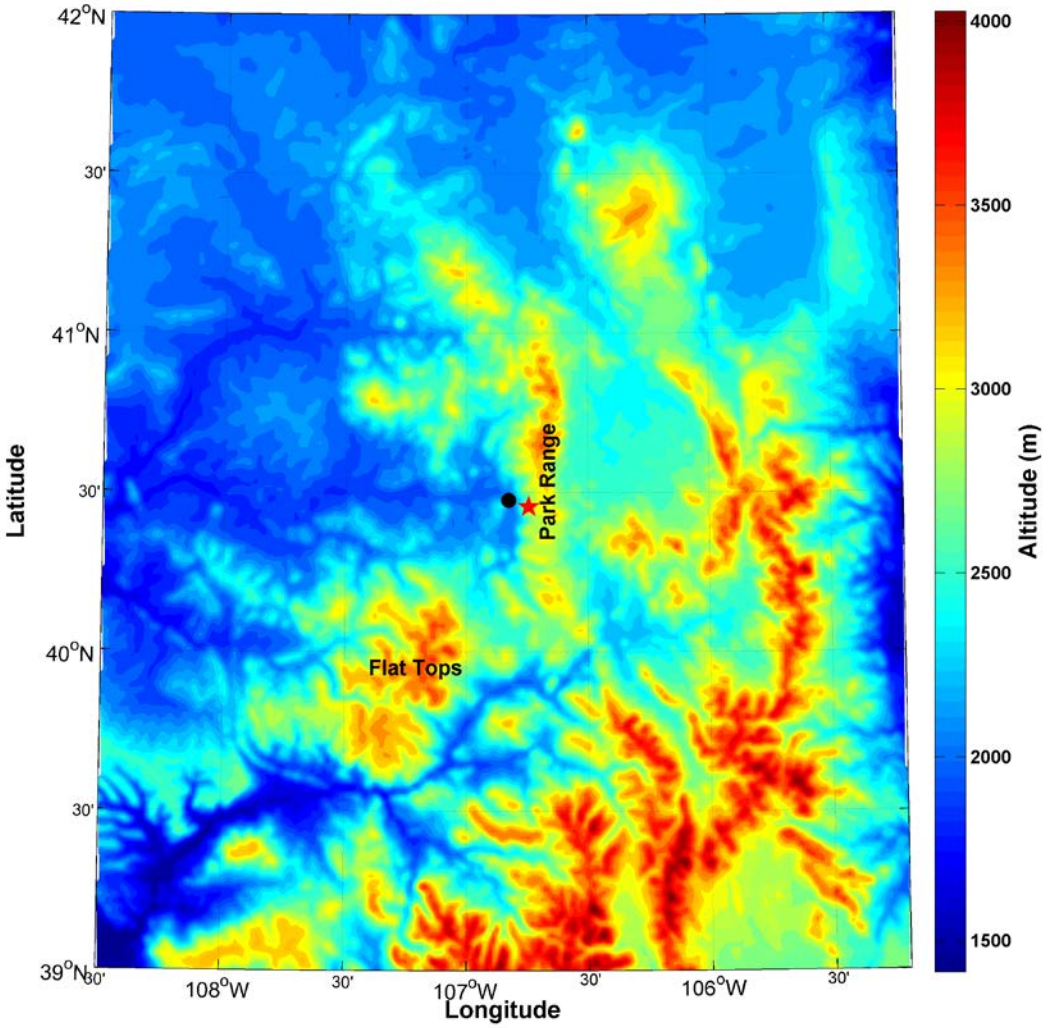

Figure 1. Shows the elevation profile of the study area and the location of Storm Peak Lab (marked by the red star) and the town of Steamboat Springs where the BBSS was located (black circle).

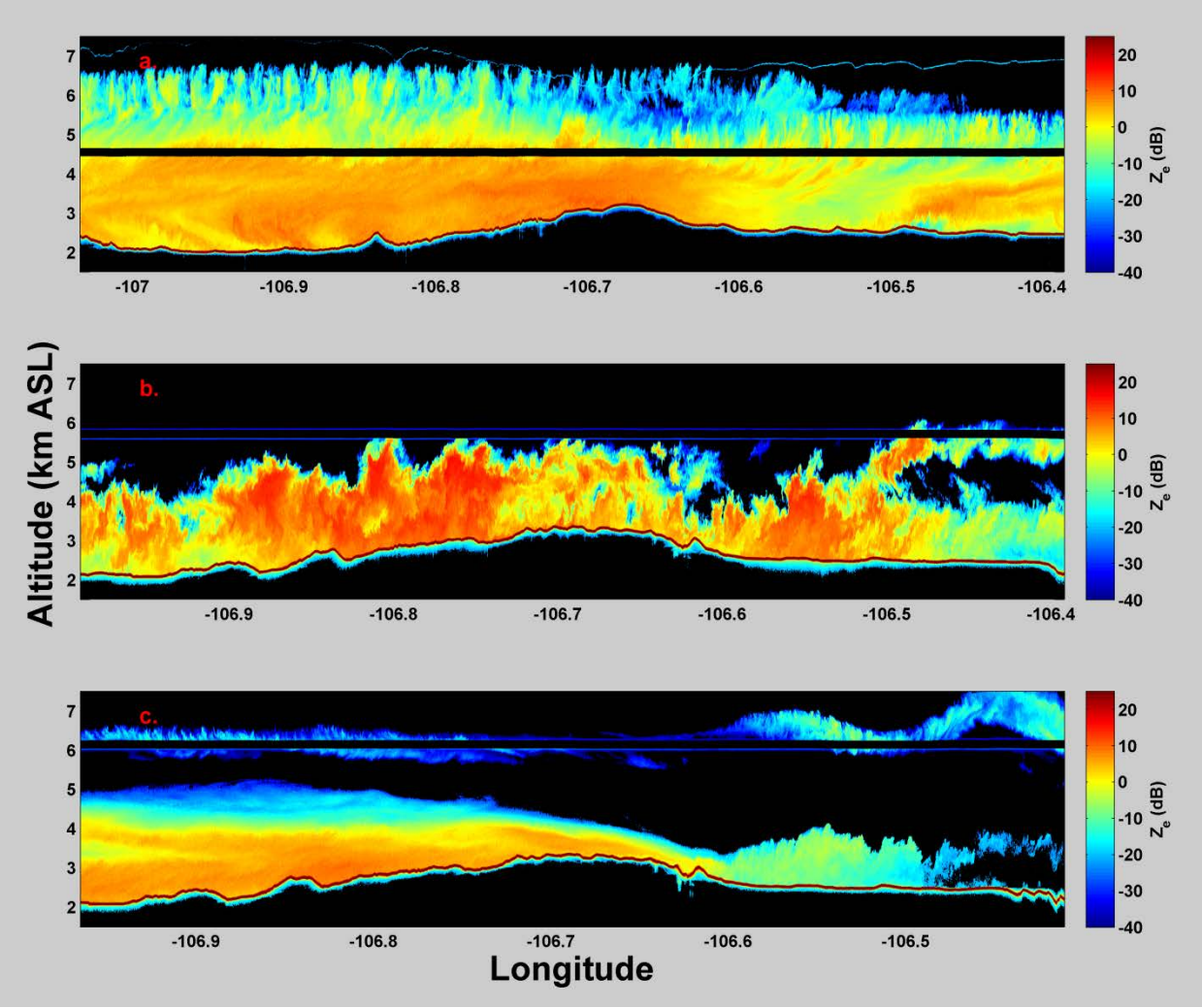

Figure 2. Examples of the hybrid (a.), convective (b.) and wave (c.) cloud types observed over the Park Range obtained from the upward and downward pointing WCR.

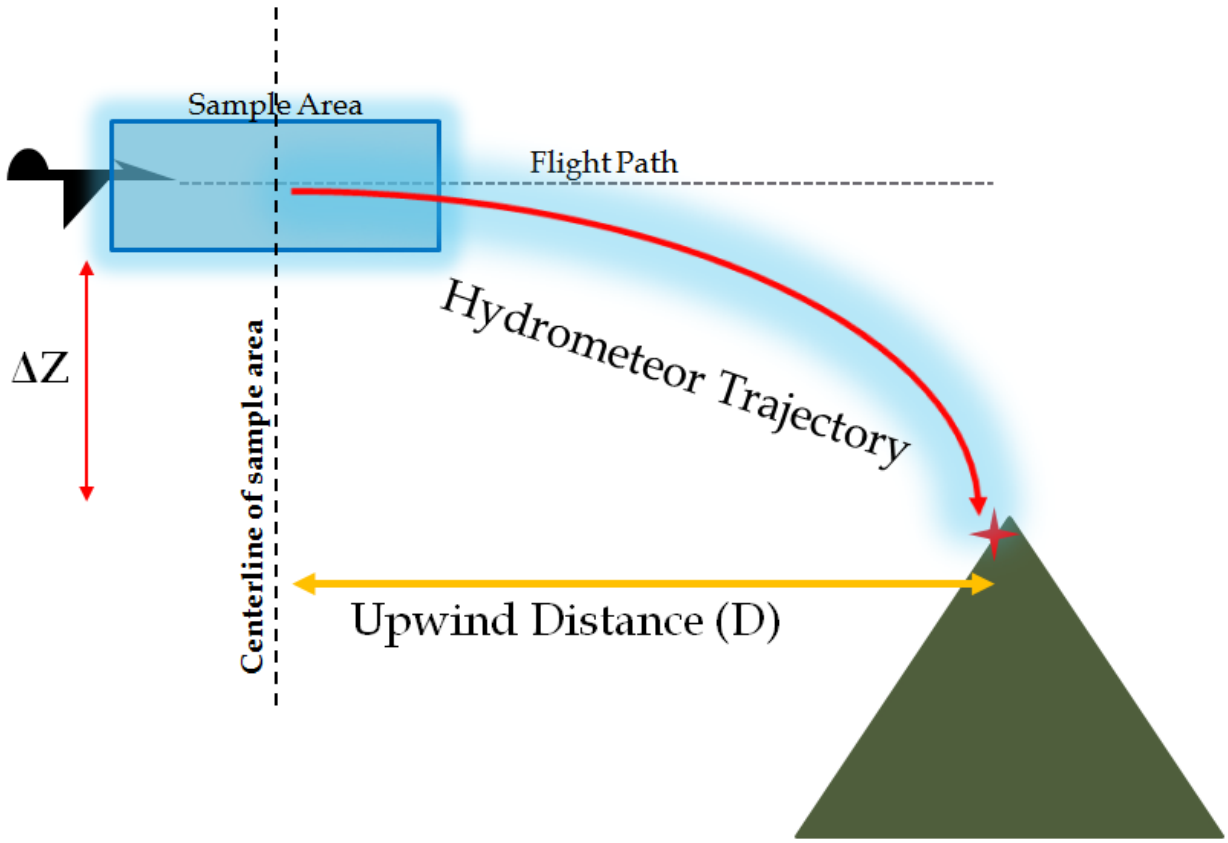

Figure 3. An example of a hydrometeor trajectory sampled by the UWKA and then arriving at SPL (red compass). ΔZ represents the difference in altitude between SPL and the UWKA. D is the upwind distance necessary for the same hydrometeor to be sampled by the UWKA and SPL.

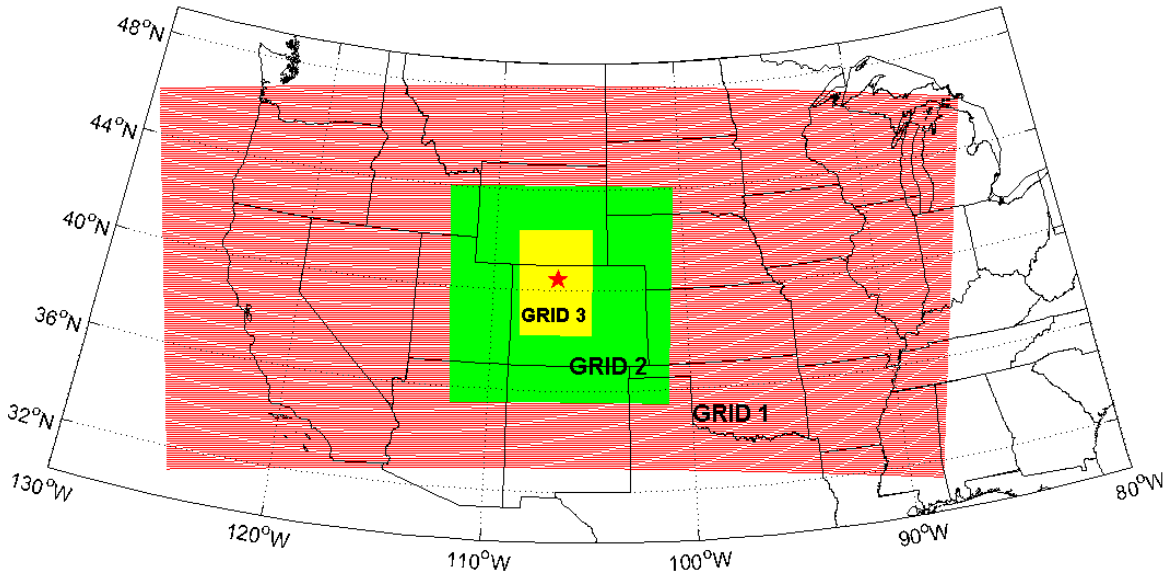

Figure 4. The domain setup for the WRF model runs with the outermost domain (GRID1) highlighted in red, the middle domain (GRID2) in green and the innermost domain (GRID3) in yellow. The red star represents the location of SPL.

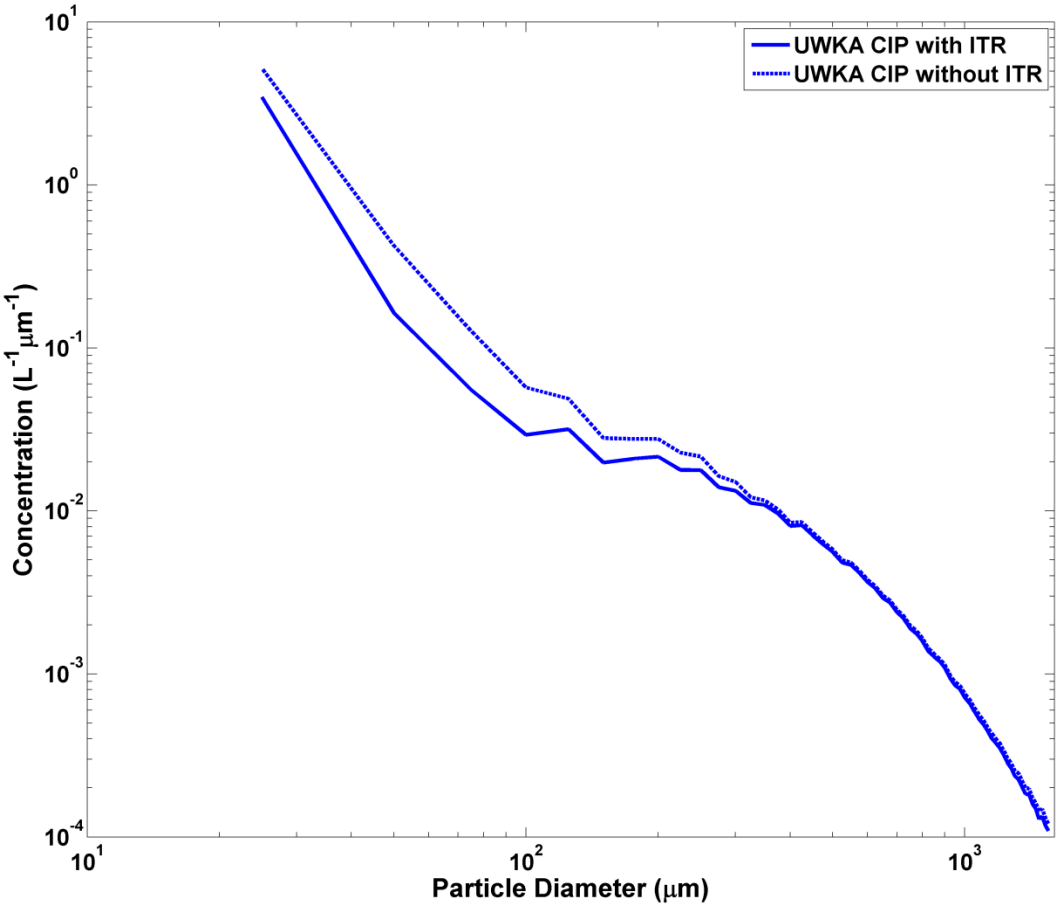

Figure 5. The impact of the interarrival time rejection (ITR) on the average UWKA CIP PSD for all seven cases when crystals are present. Solid line is the PSD when the ITR is applied and the dashed line is when no ITR is applied

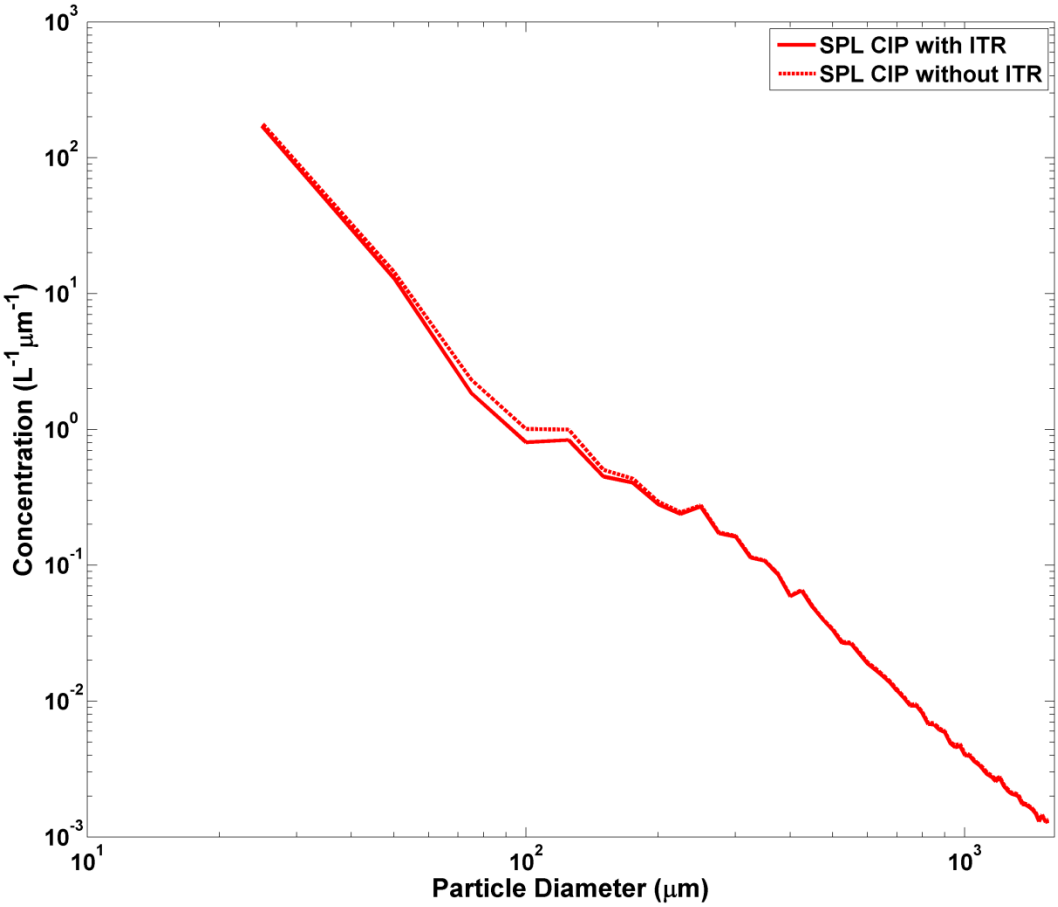

Figure 6. The impact of the interarrival time rejection (ITR) on the average SPL CIP PSD for the December 15th (RF#1) case when crystals are present. Solid line is the PSD when the ITR is applied and the dashed line is when no ITR is applied

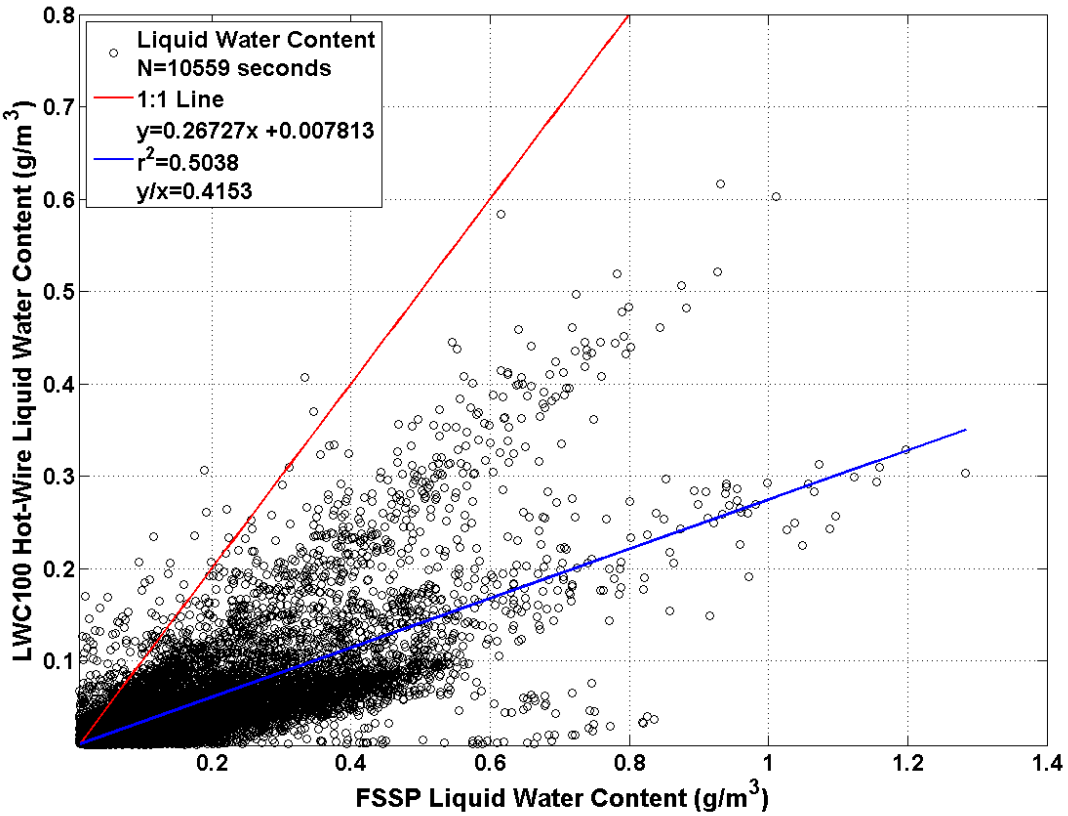

Figure 7. Liquid Water Content comparison between the UWKA FSSP and LWC100 Hot-Wire for all seconds when both probes reported the presence of liquid water during the 7 flights examined in this study. The red line is the 1 to 1 line and the blue line is the linear fit between the two datasets.

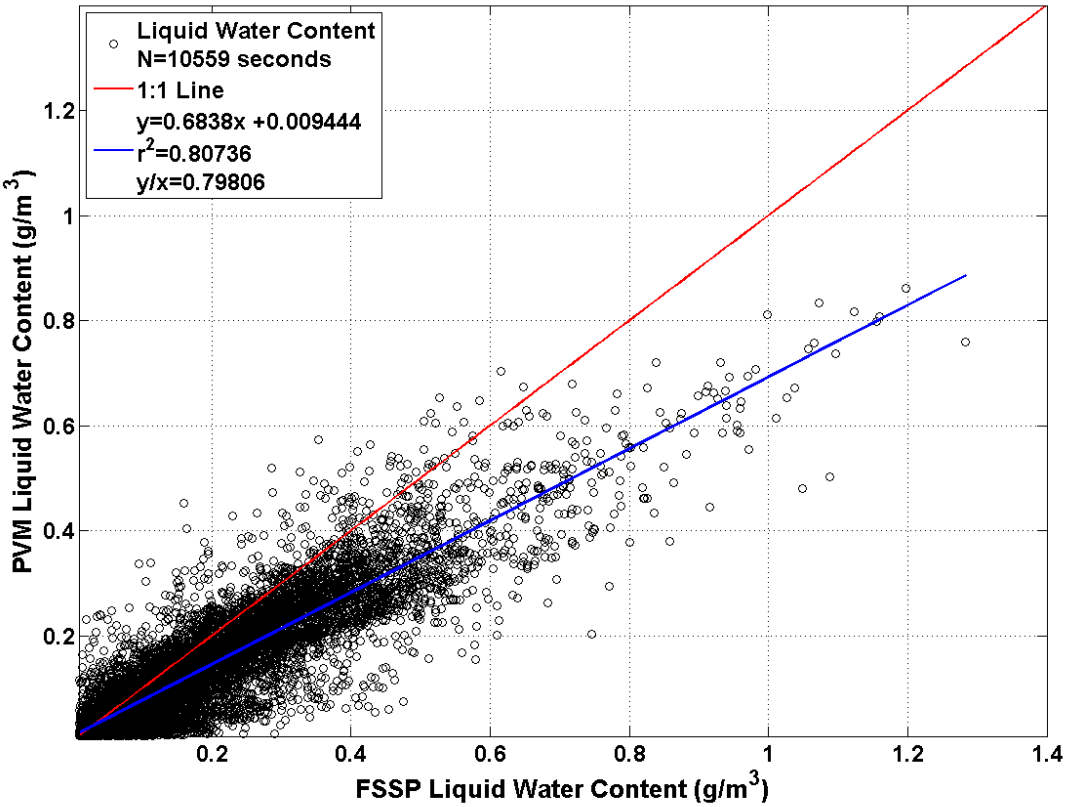

Figure 8. Same as for Figure 7 but for the comparison between the UWKA FSSP and PVM

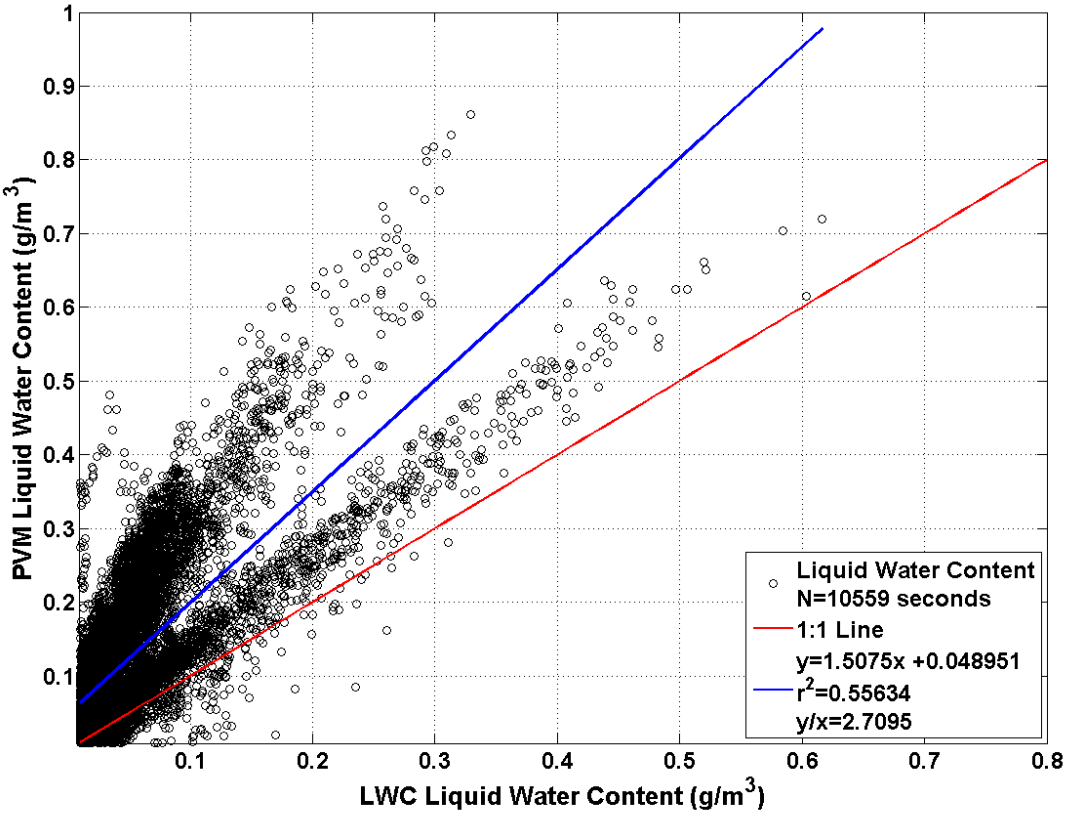

Figure 9. Same as for Figure 7 but for a comparison between the UWKA PVM and the LWC100 Hot-Wire.

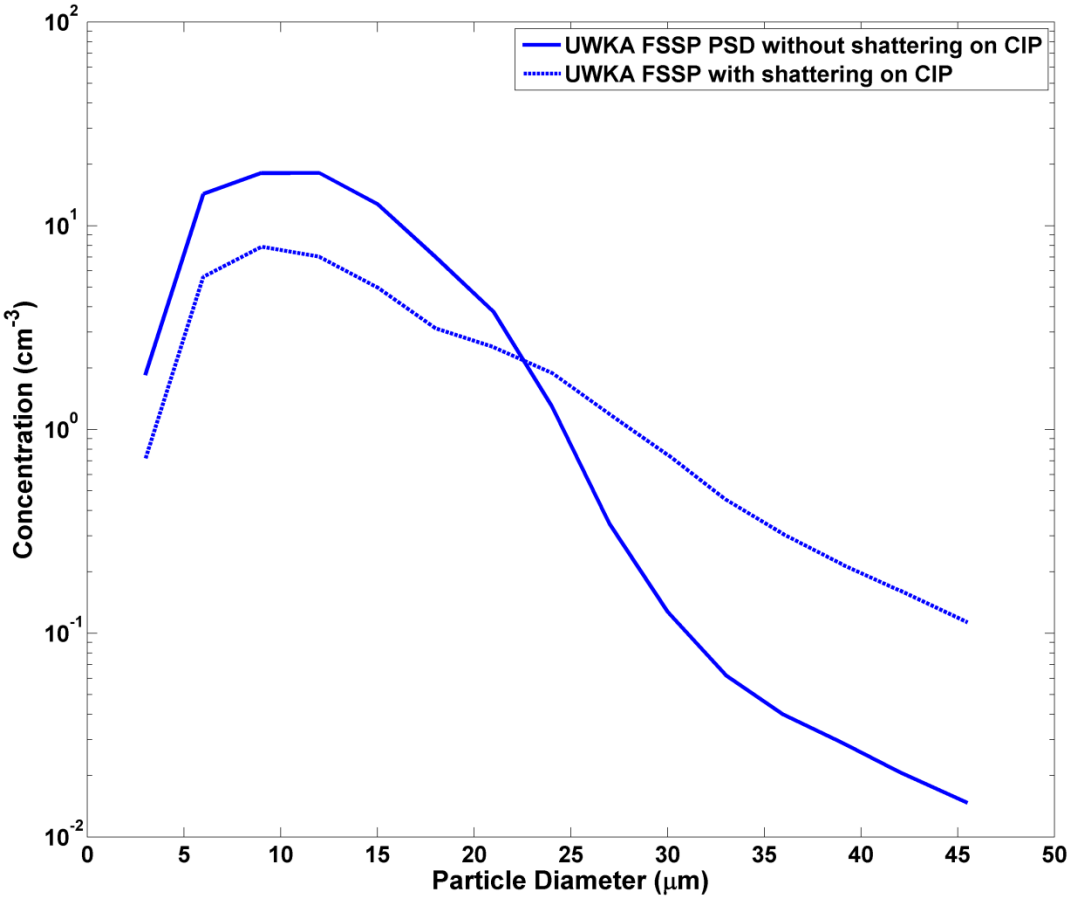

Figure 10. Comparison of the UWKA FSSP PSD with (dashed line) and without (solid line) shattering reported on the UWKA CIP.

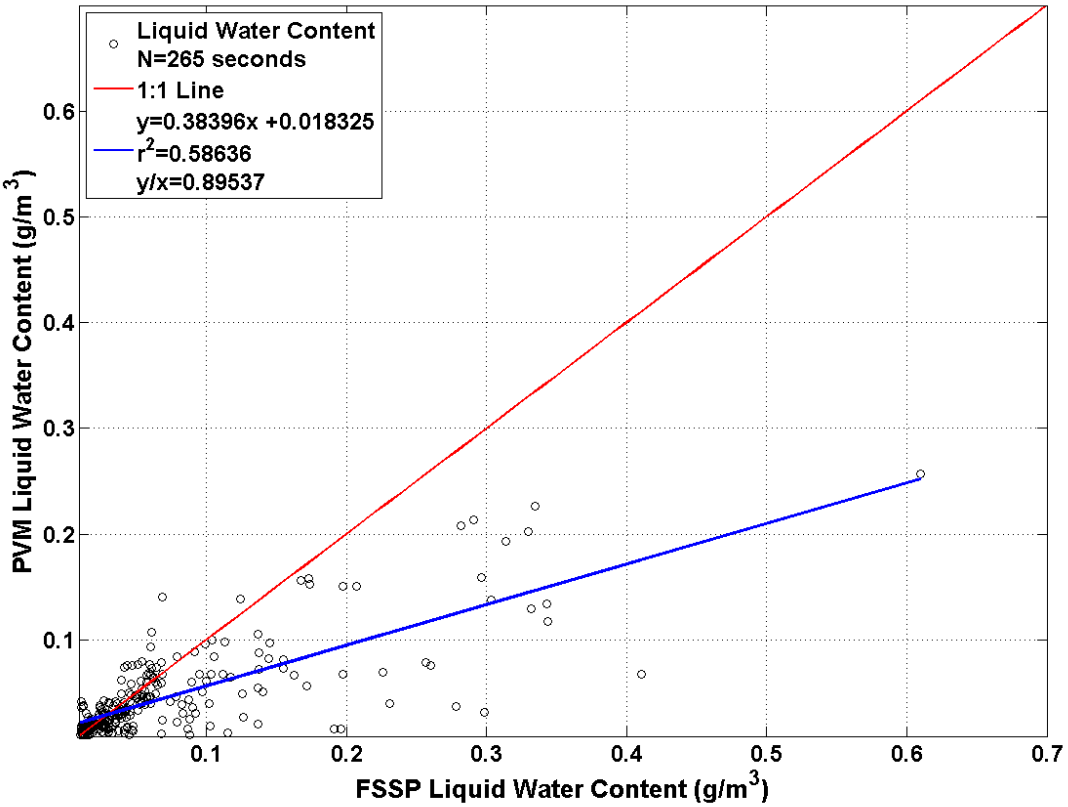

Figure 11. Comparison between the LWC from the UWKA FSSP and PVM when both probes reported LWC>=0.01 and no crystals were present on the CIP.

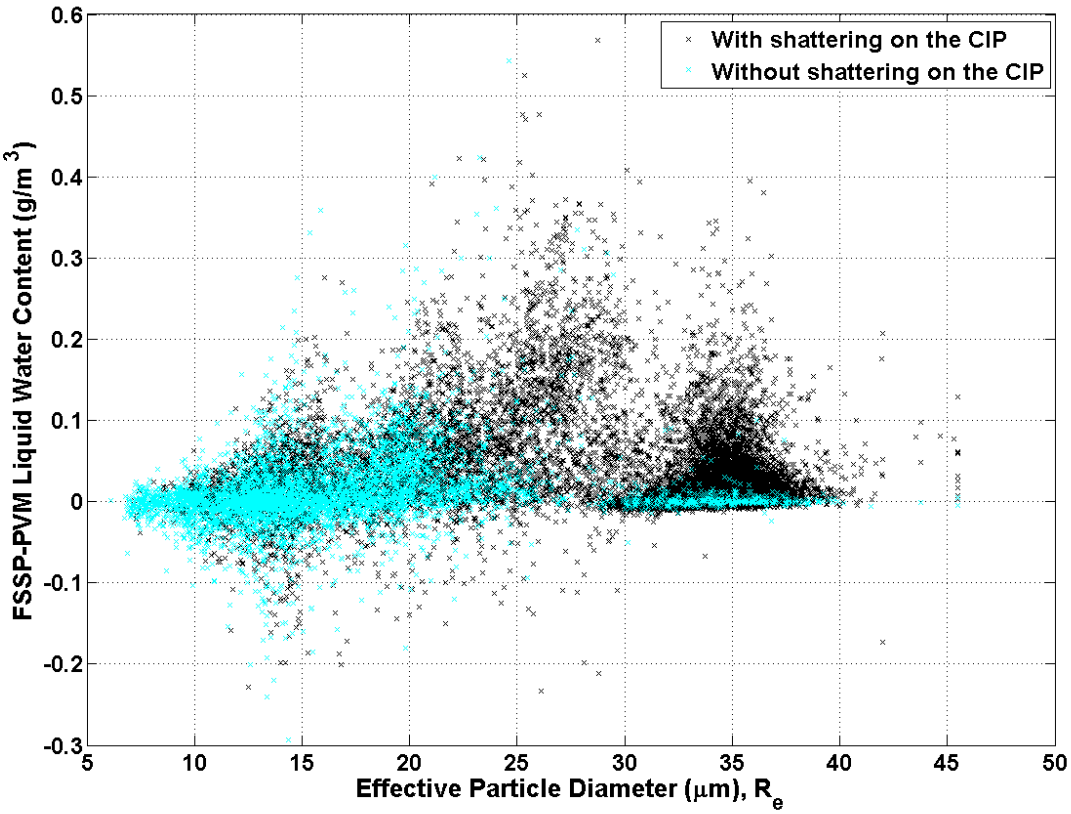

Figure 12. Difference in UWKA LWC observed from the FSSP and PVM based on effective particle radius when shattering (black x's) and no shattering (cyan x's) was observed on the CIP.

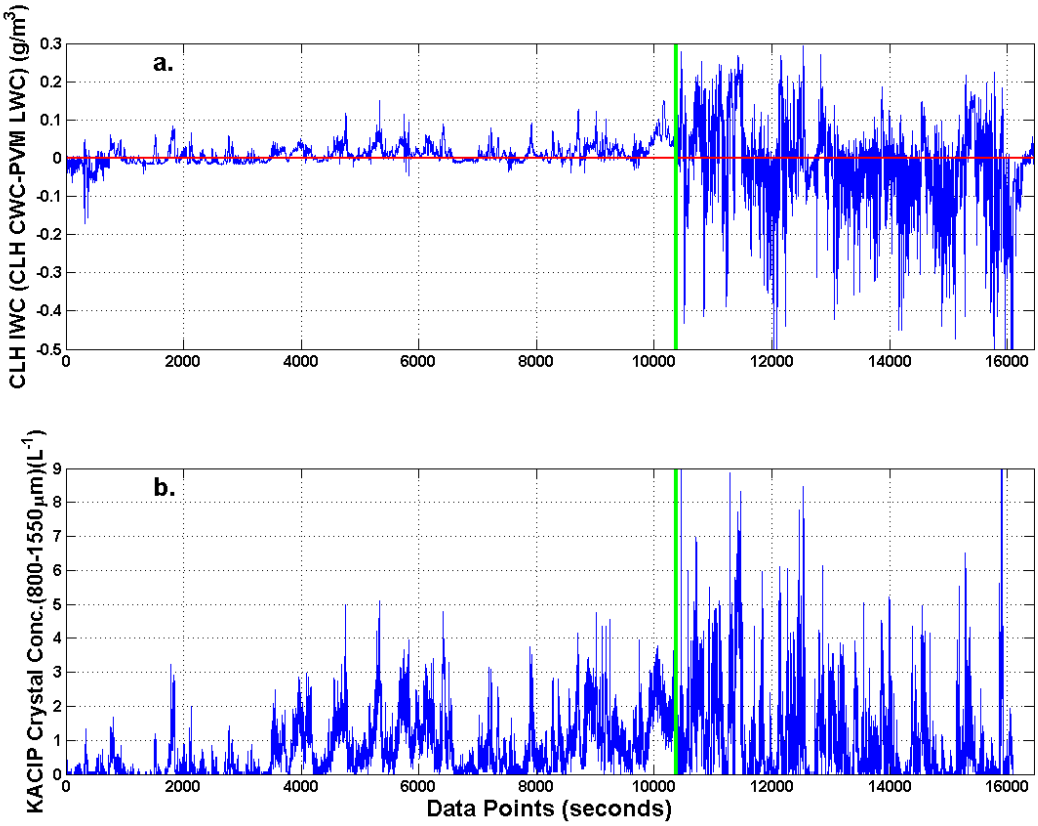

Figure 13. CLH-derived IWC (a.) and UWKA CIP crystal concentrations for crystals between 800 and 1550 microns (b.) The vertical green line refers to the start of RF#12and the red line in panel a. is the zero line.

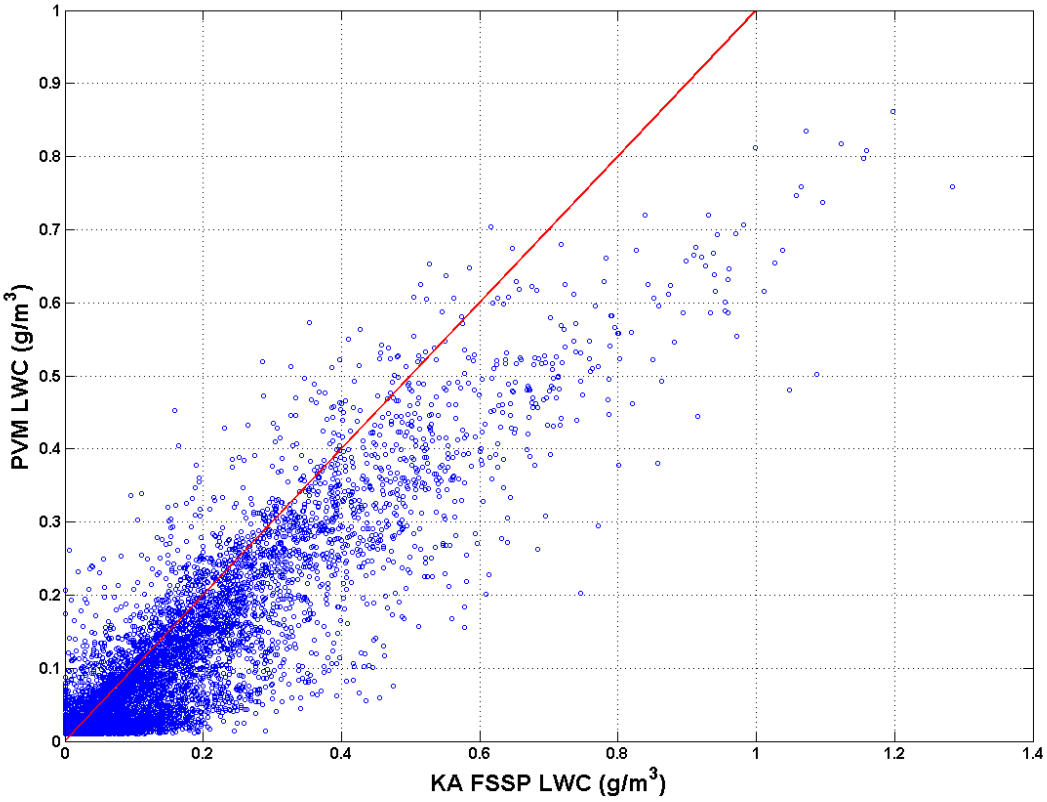

Figure 14. Comparison between the UWKA FSSP and PVM LWC for seconds when the CLH was functioning and after the start of RF#12. The red line signifies the 1 to 1 line.

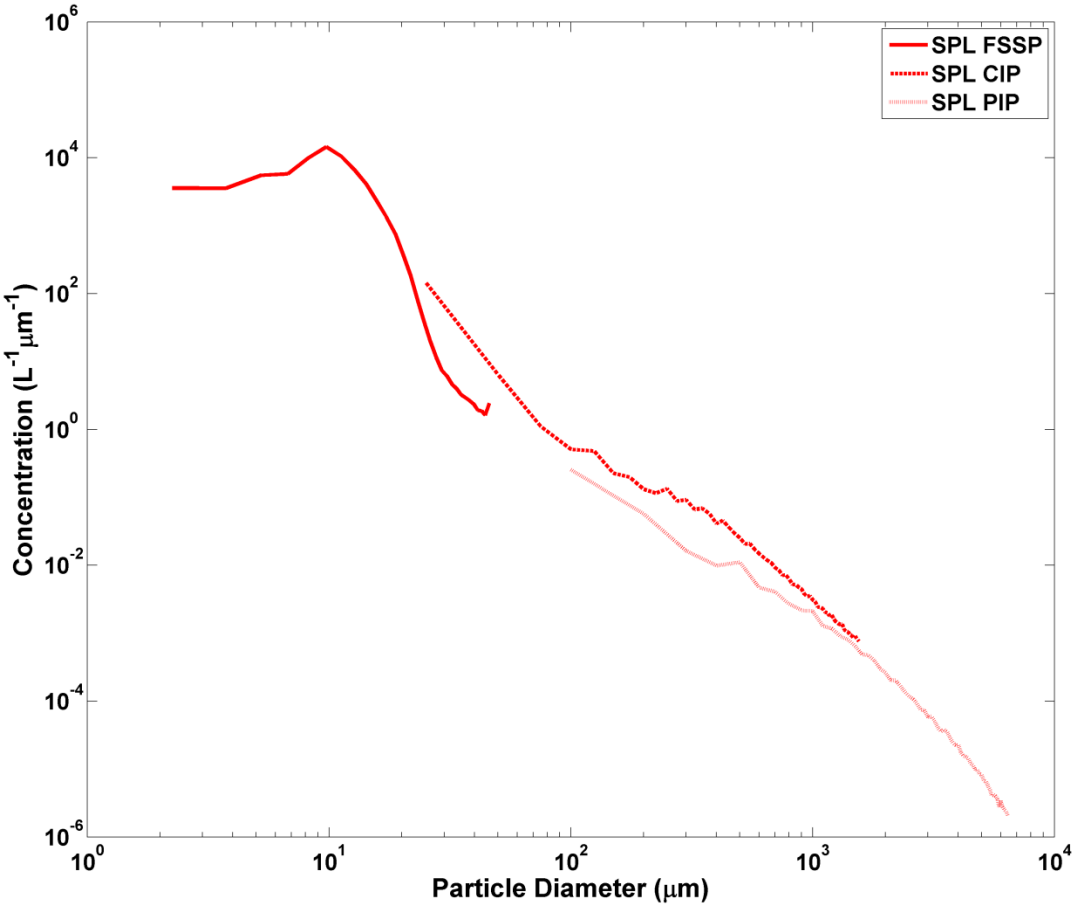

Figure 15. Average Particle Size Distribution from the SPL FSSP (solid line), CIP (dashed line) and PIP (dotted line) for the seven cases analyzed.

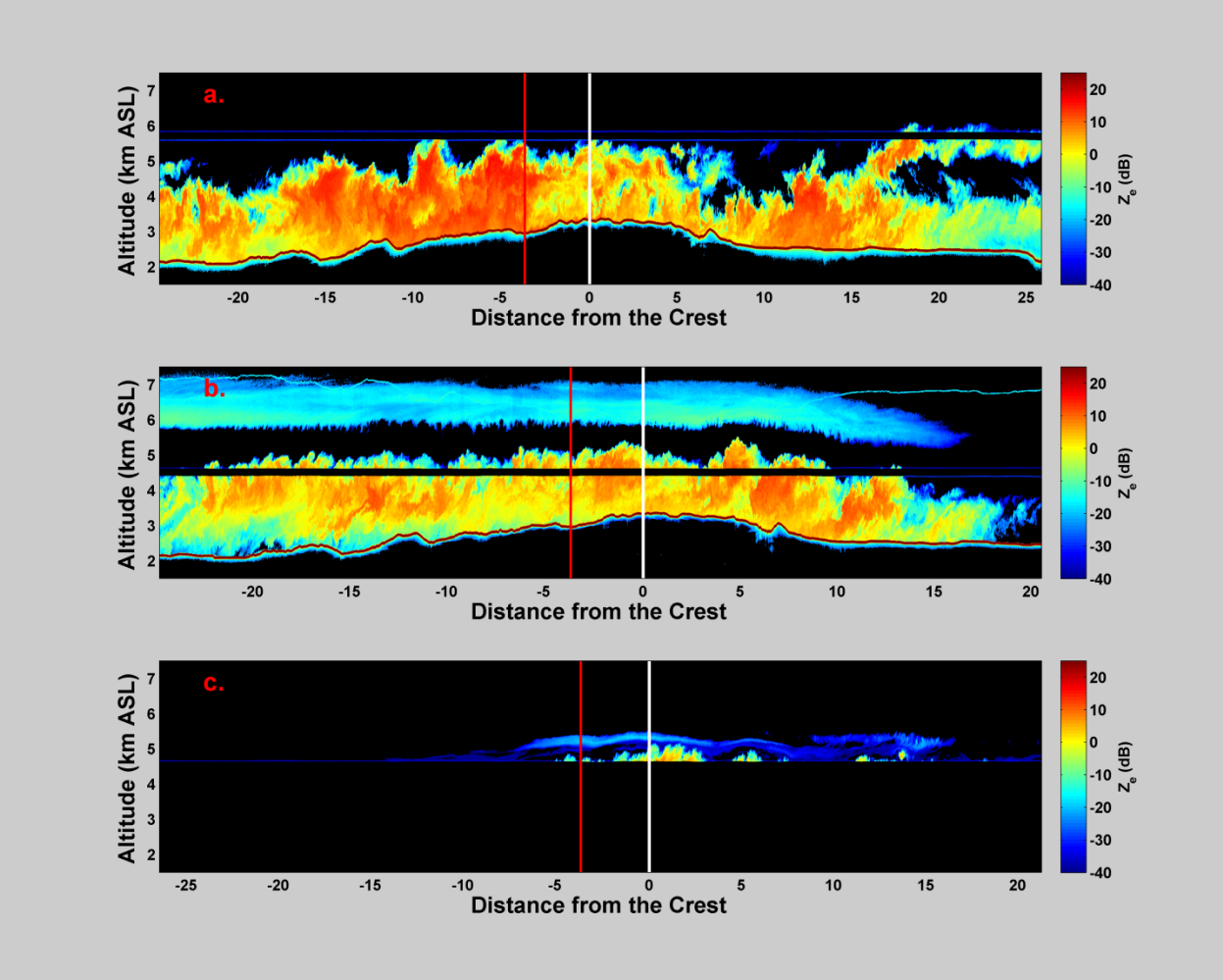

Figure 16. Example of the cloud structure as observed from the WCR for RF#12 (a.), RF#26 (b.) and RF#28 (c.). The vertical white line is the crest of the Park Range and the vertical red line is the location of SPL.

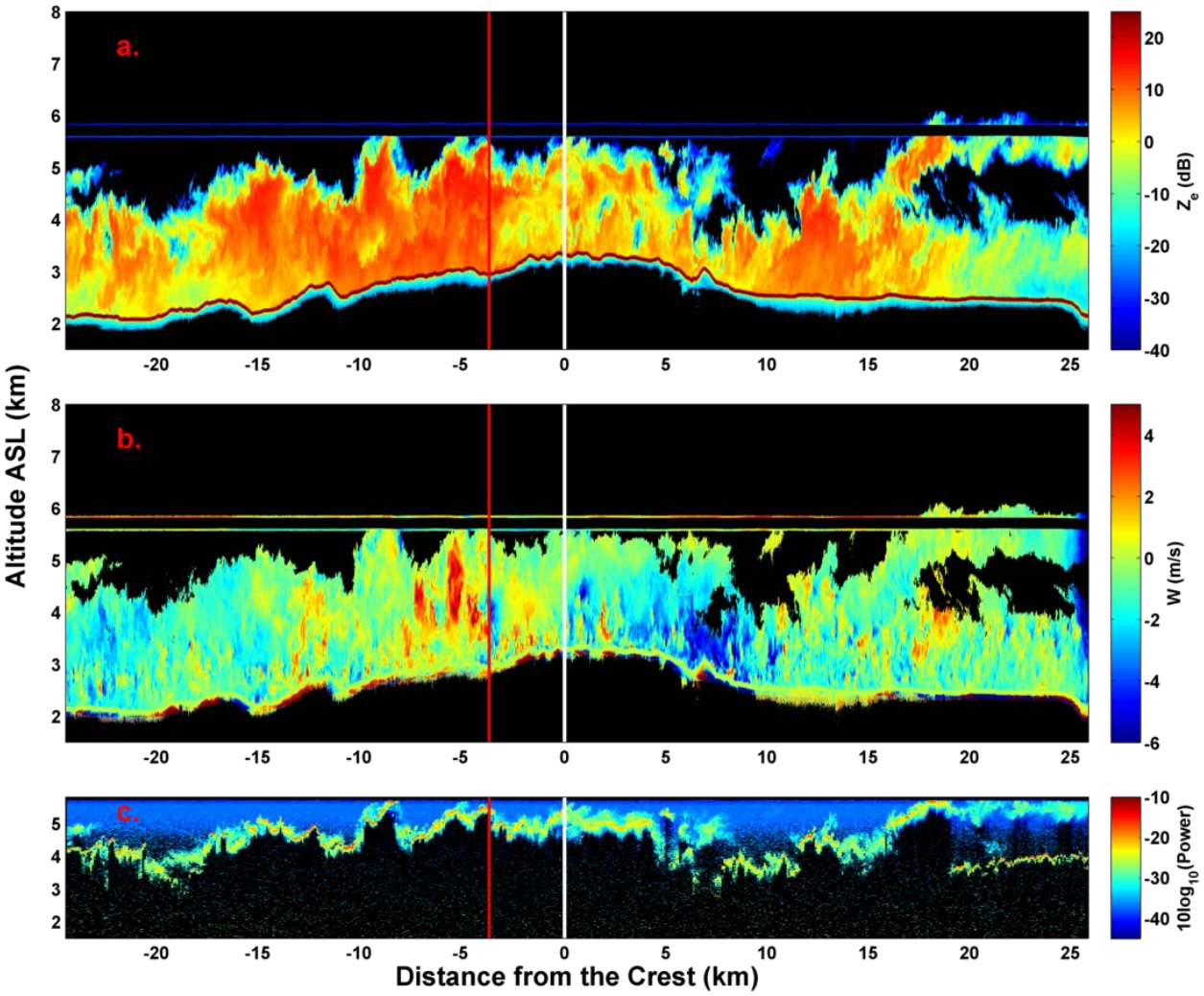

Figure 17. An example of the WCR reflectivity (a.), vertical velocity (b.) and WCL Power (c.) during RF#12. The white line represents the location of the crest while the red line is the location of SPL.

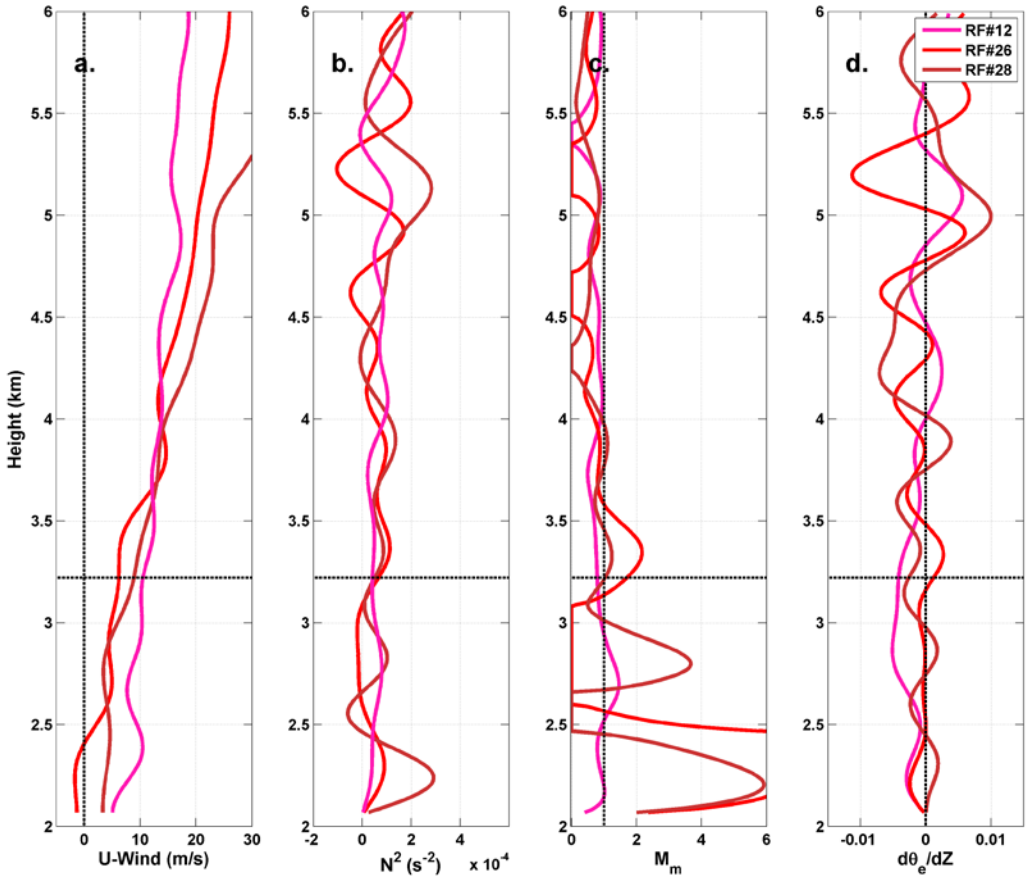

Figure 18. Sounding based profiles of u-wind speed (a.), moist static-stability (b.), inverse Froude number (c.), and potential instability (d.) for all three convective flights. The horizontal dotted black line represents the altitude of SPL.

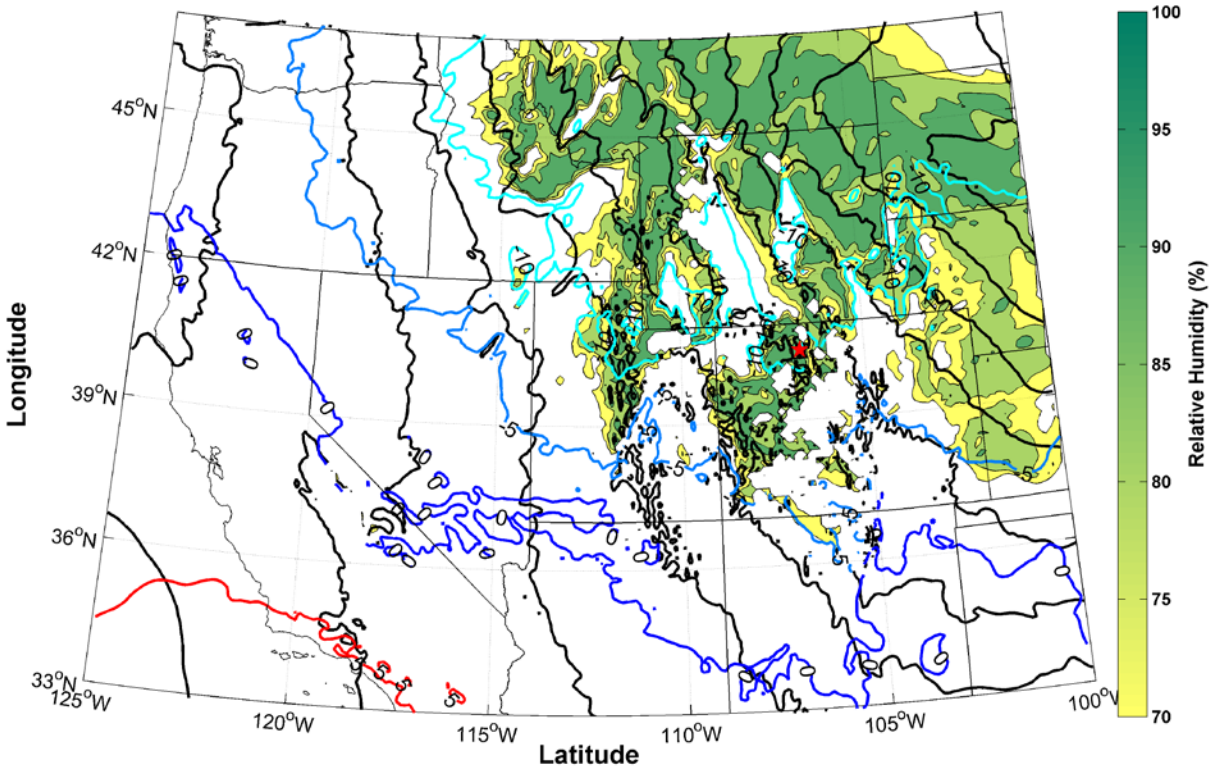

Figure 19. Model-derived 700 hPa height (black contours), relative humidity (color fill) and temperature contours for RF#12. The red star indicates the location of SPL.

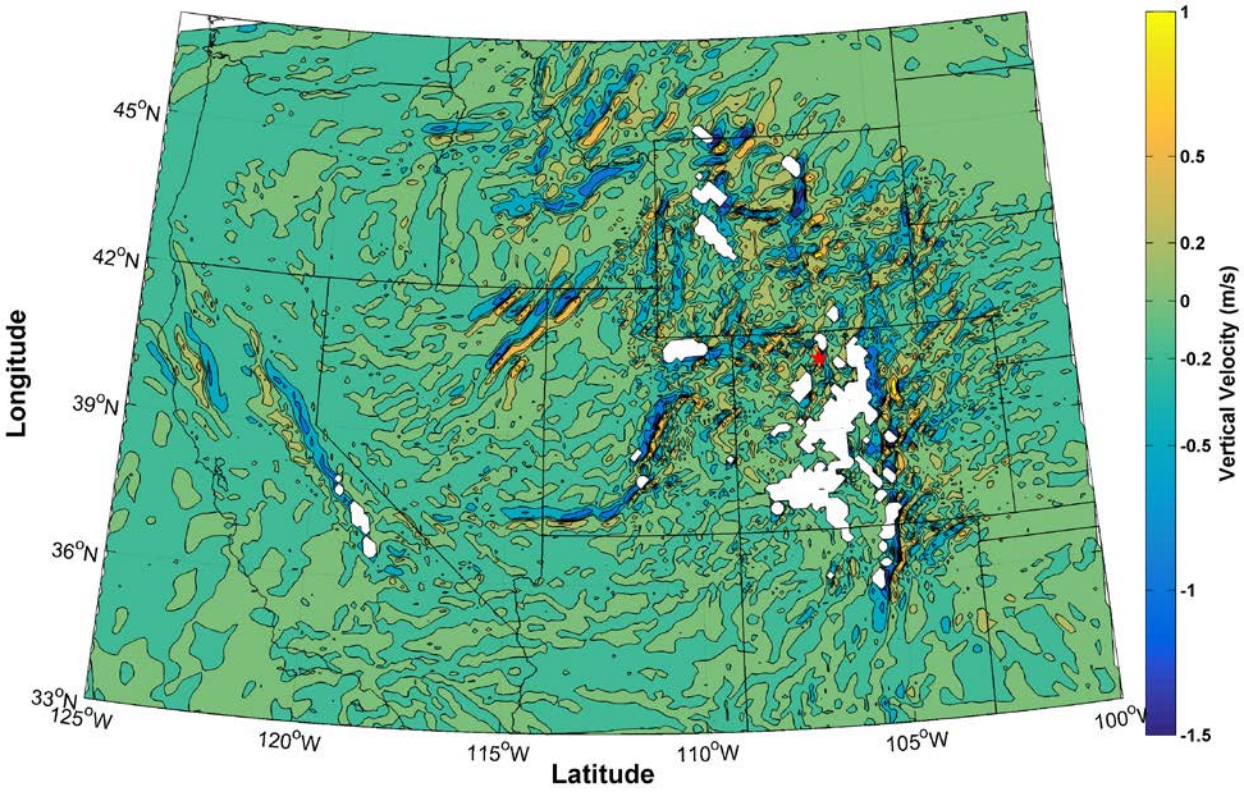

Figure 20. Model-derived 700 hPa vertical velocity contours during RF#12. The lack of color fill is where the terrain exceeds the 700 hPa height level. The red star indicates the location of SPL.

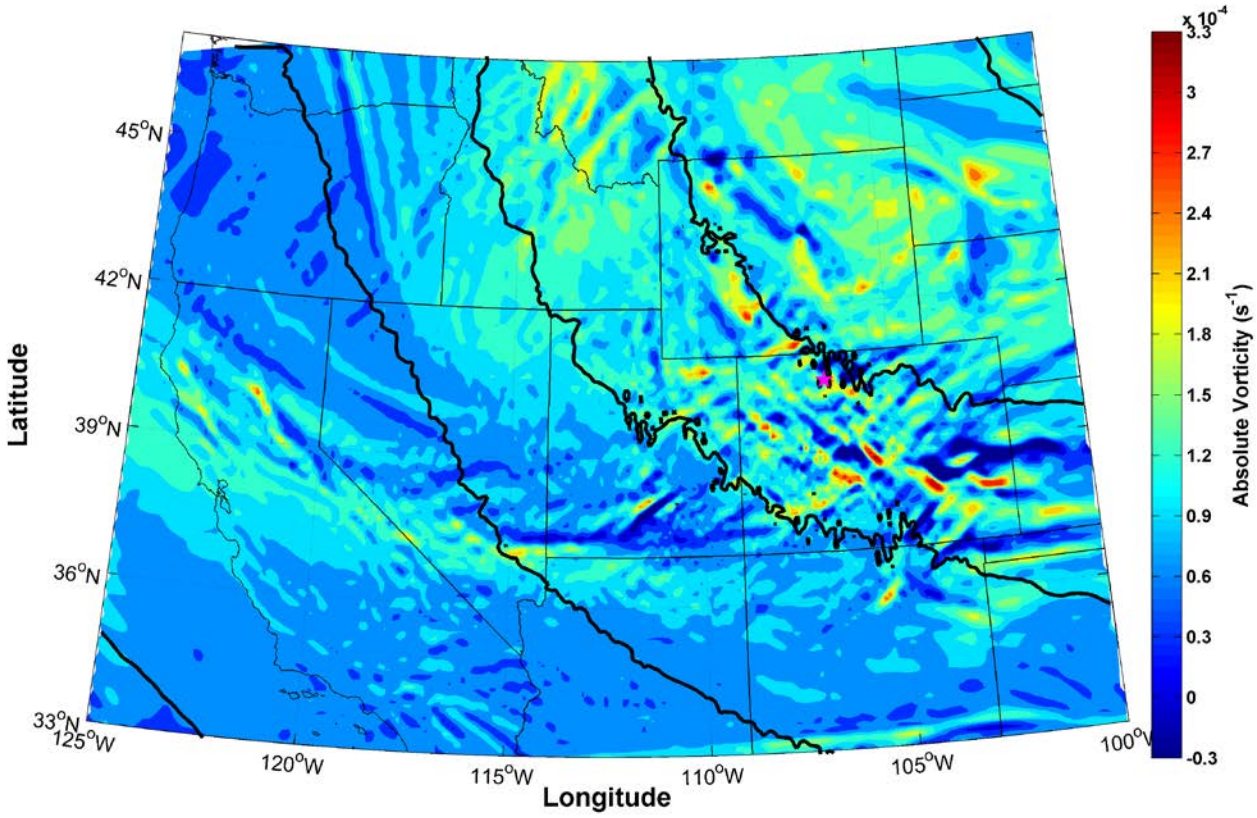

Figure 21. 500 hPa absolute vorticity (s-1) (color fill) and height (black lines) during RF#12. The red star indicates the location of SPL.

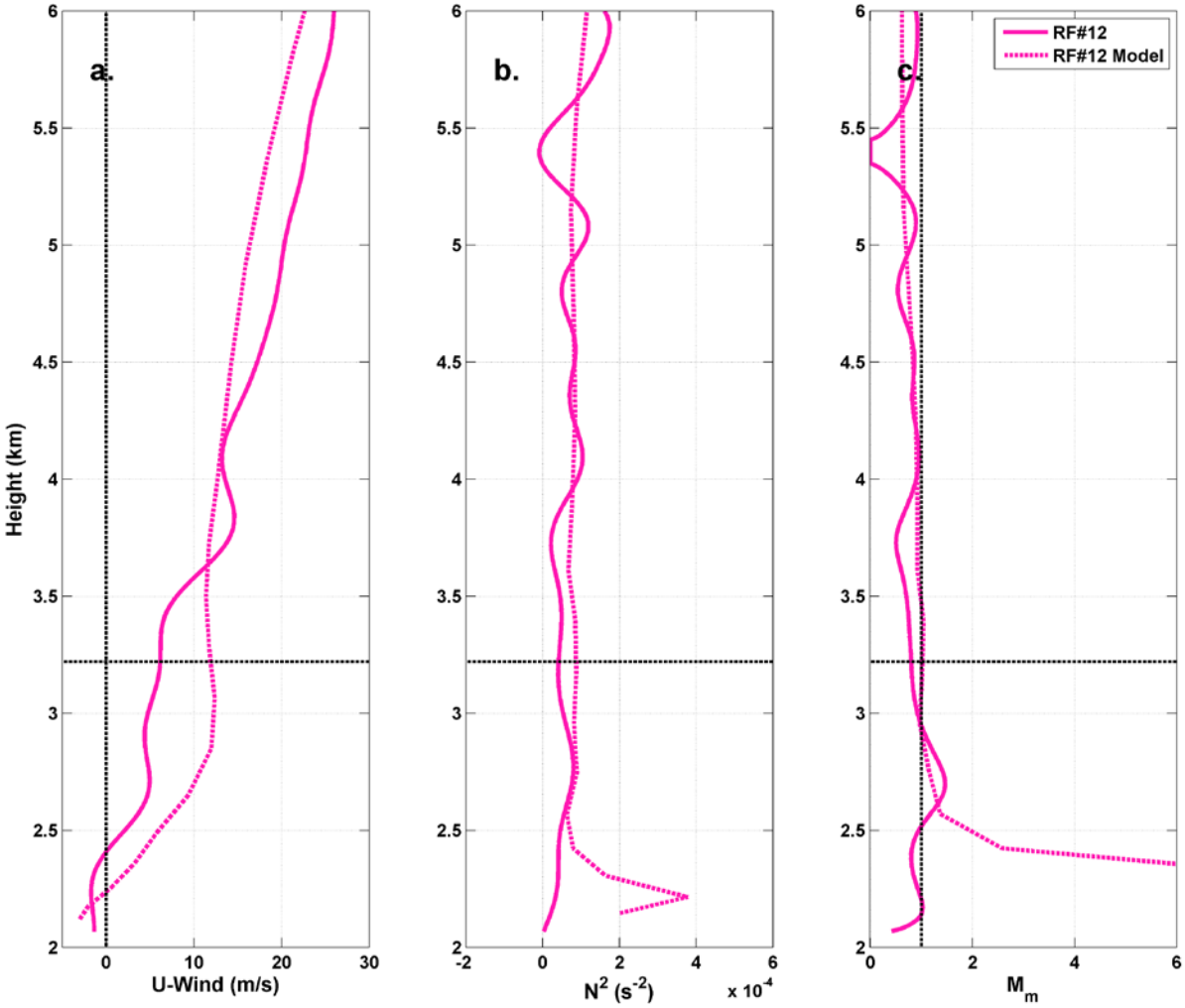

Figure 22. Comparison between model-derived (dotted line) and observed (solid line) sounding at the onset of RF#12. The u-component of the wind speed (a.), static stability (b.) and M_m (c.) are compared.

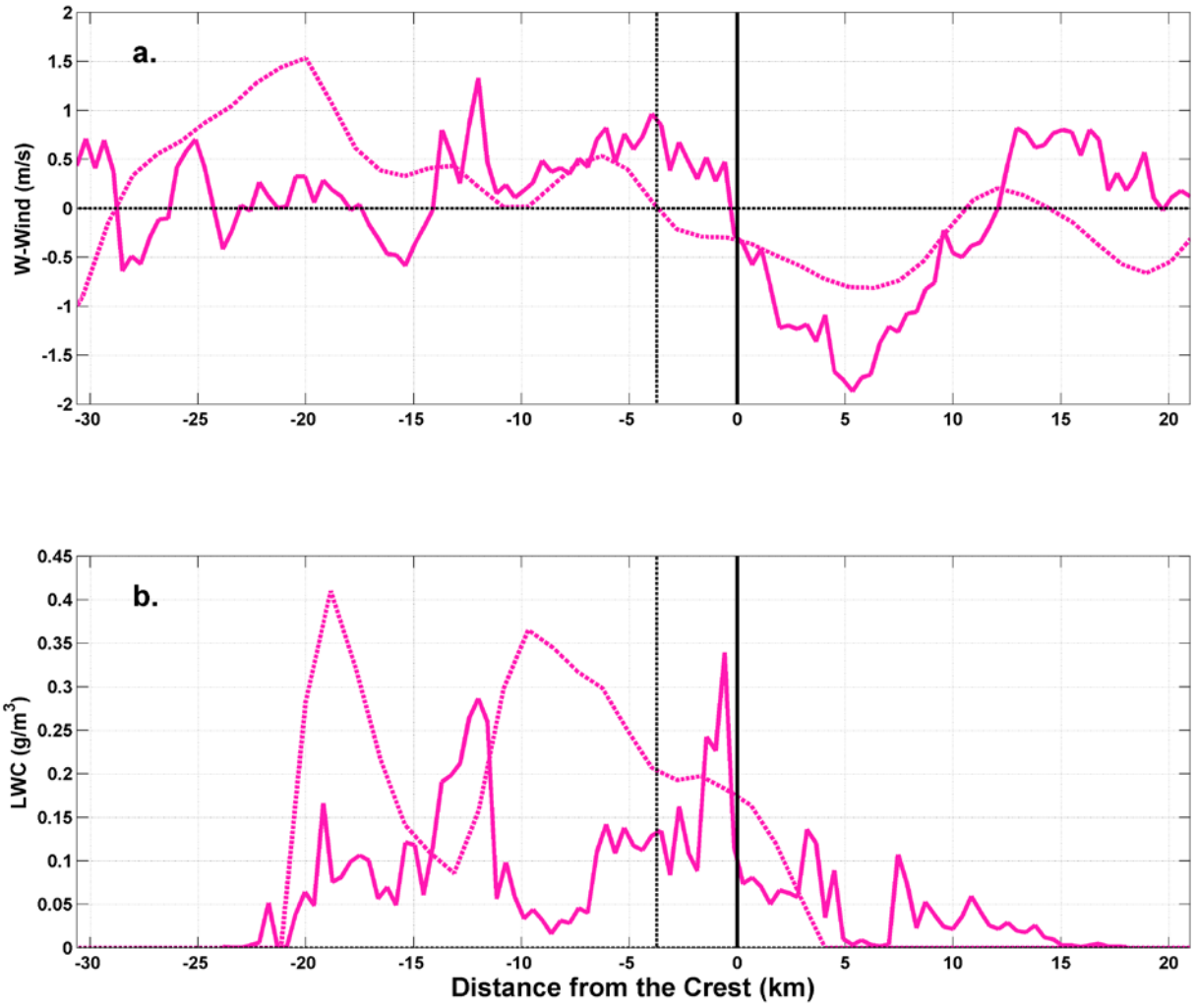

Figure 23. Cross-barrier profiles of model-derived (dotted line) and observed (solid line) vertical velocity (a.) and LWC (b.) during RF#12. The black dotted vertical line represents the location of SPL on the barrier while the solid black line represents the location of the crest of the Park Range.

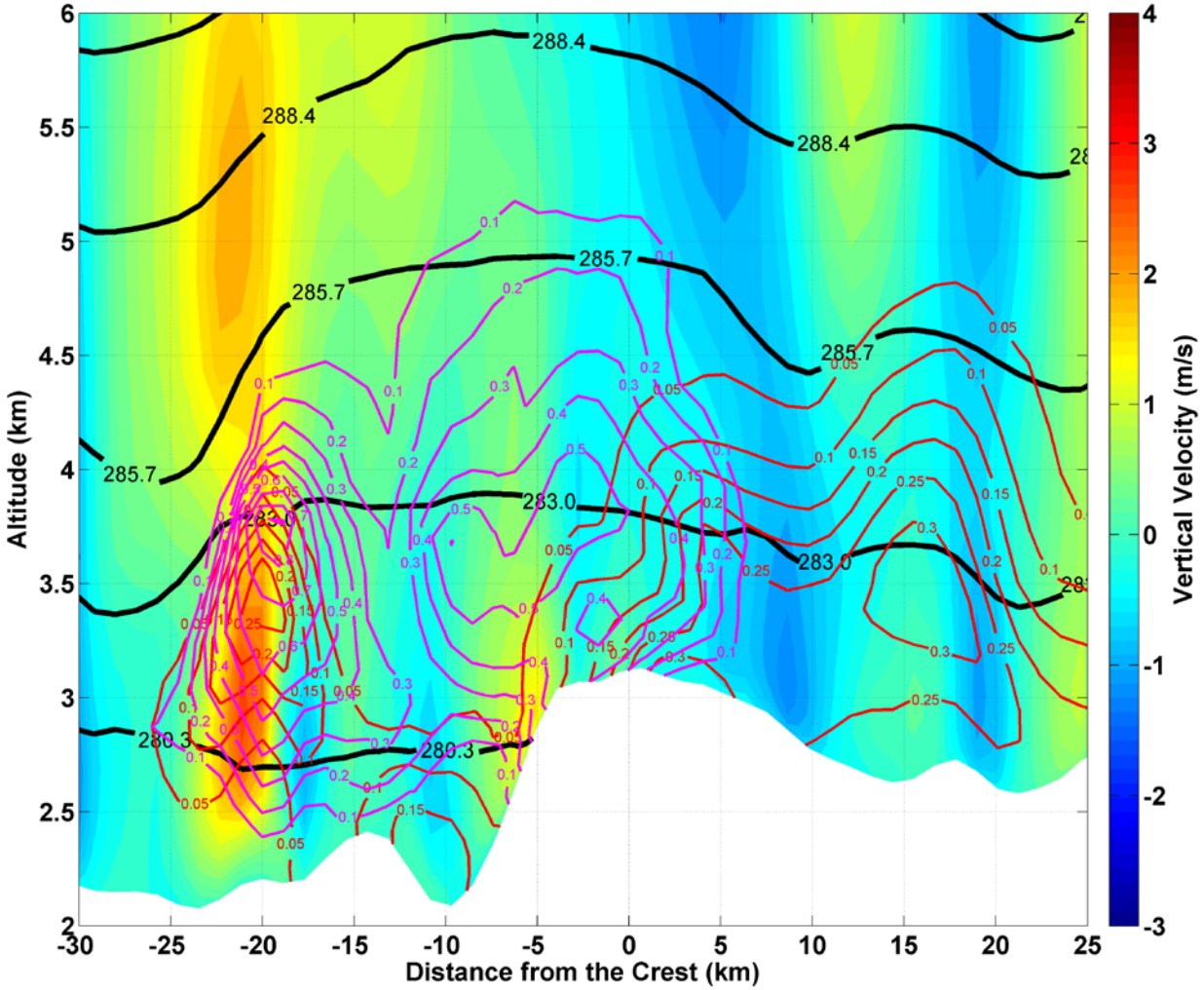

Figure 24. Model-derived vertical cross section of theta (black contours), vertical velocity (color fill), LWC (magenta contours) and IWC (red contours) over the Park Range at the latitude of SPL during RF#12.

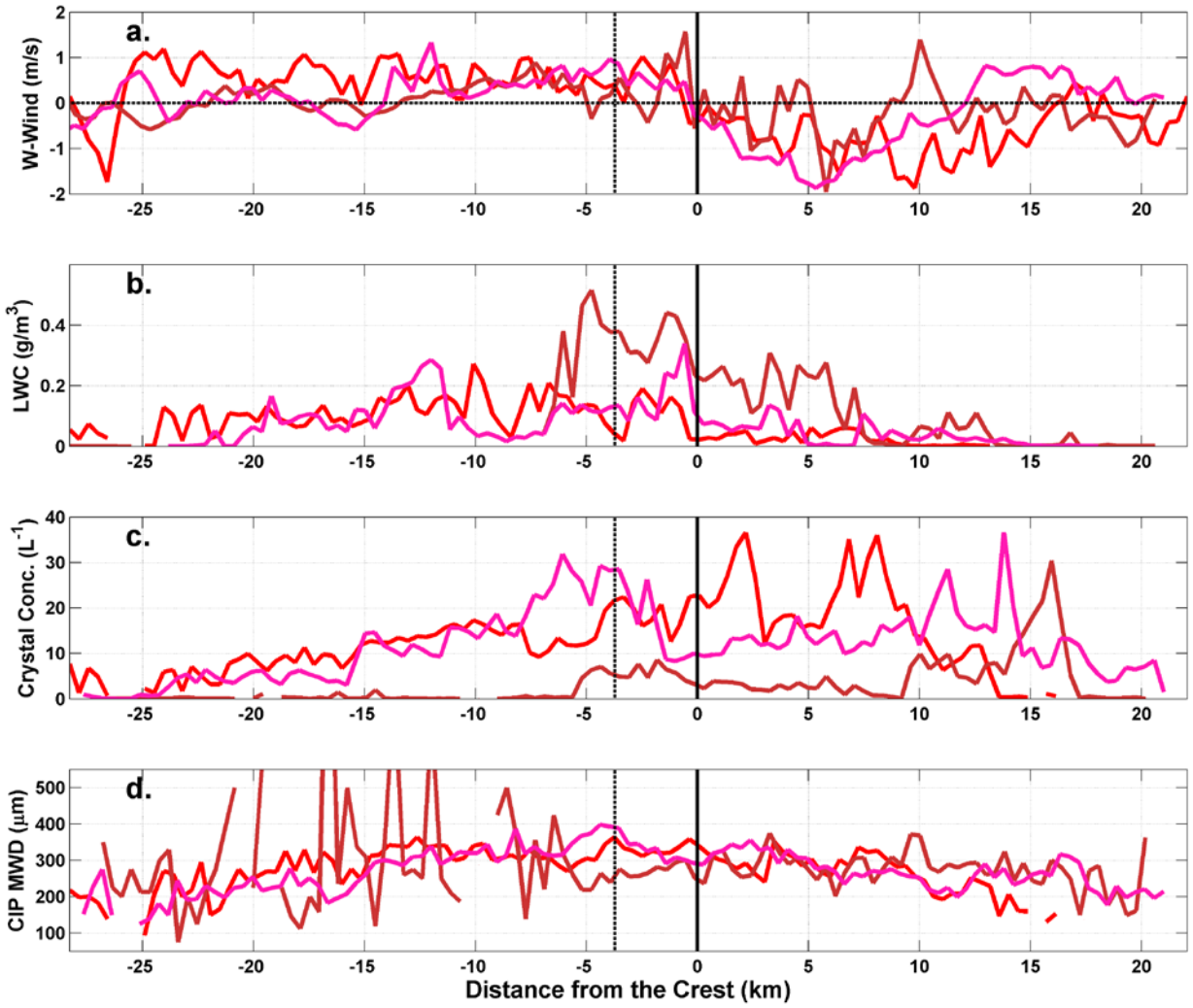

Figure 25. Average cross-barrier profiles of vertical velocity (a.), liquid water content in g/m3,(b.), crystal concentration (75-1550 microns) per liter (c.), and number weighted mean diameter for crystals (75-1550 microns) in microns (d.) for RF#12 (magenta), RF#26 (red) and RF#28 (brown).

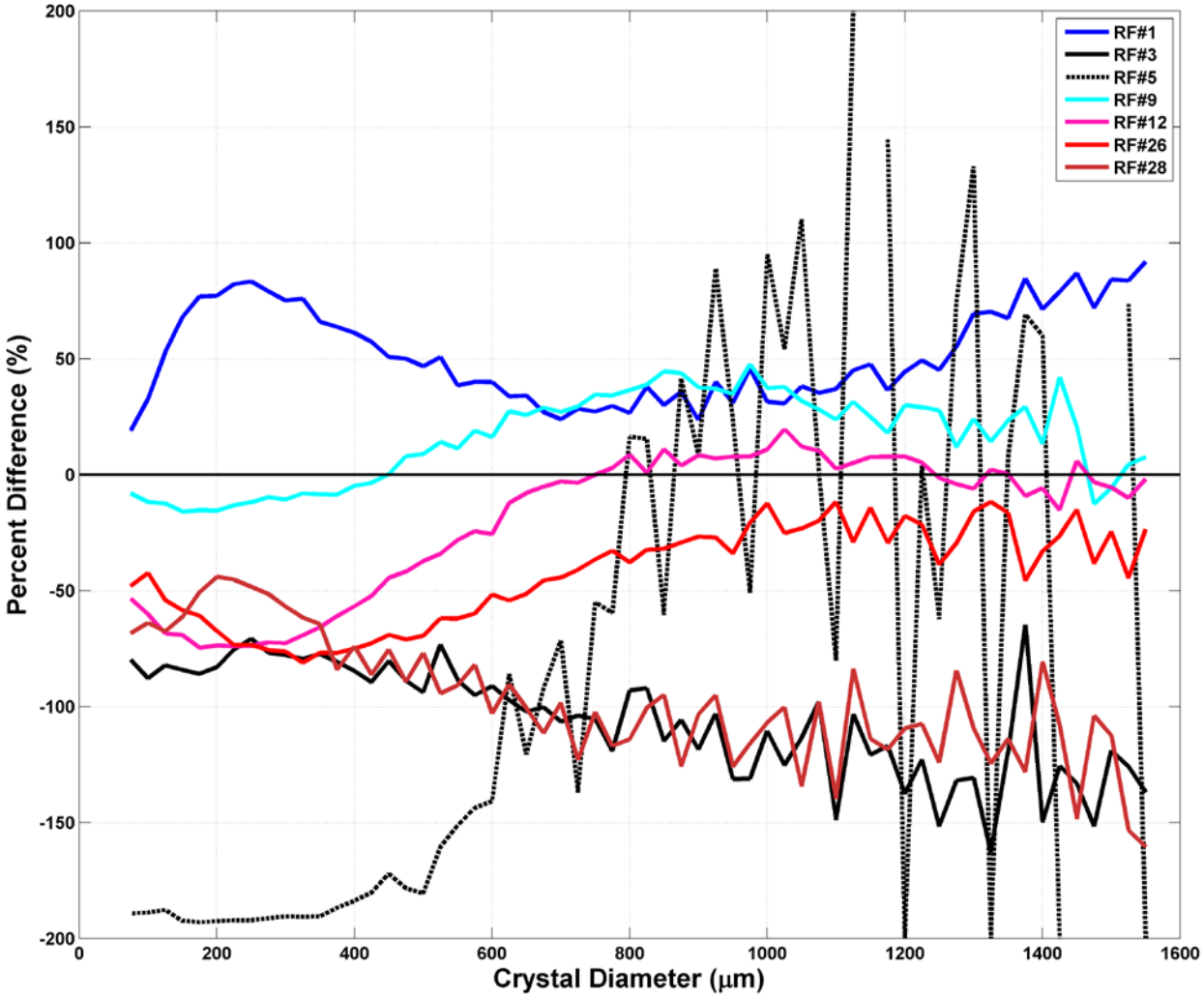

Figure 26. Percent difference between the average upwind and downwind crystal size distributions for flight levels below 4700 meters. Percent difference is calculated as (upwind-downwind)/((upwind+downwind)/2). As such, positive (negative) difference means higher concentrations on the windward (leeward) slope. Convective cases are in red, hybrid cases are in blue and wave cases are in grey hues.

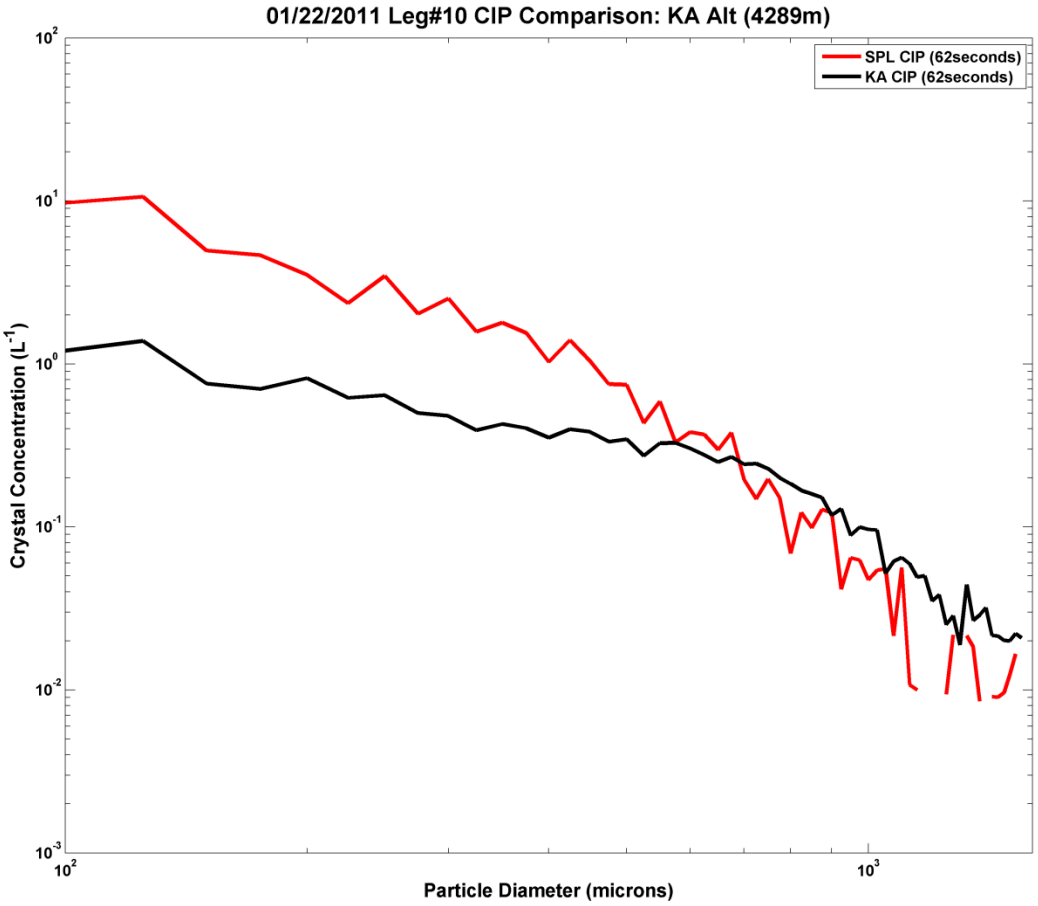

Figure 27. Comparison of the UWKA and SPL crystal size distribution based on the trajectory model for leg 10 of RF#12.

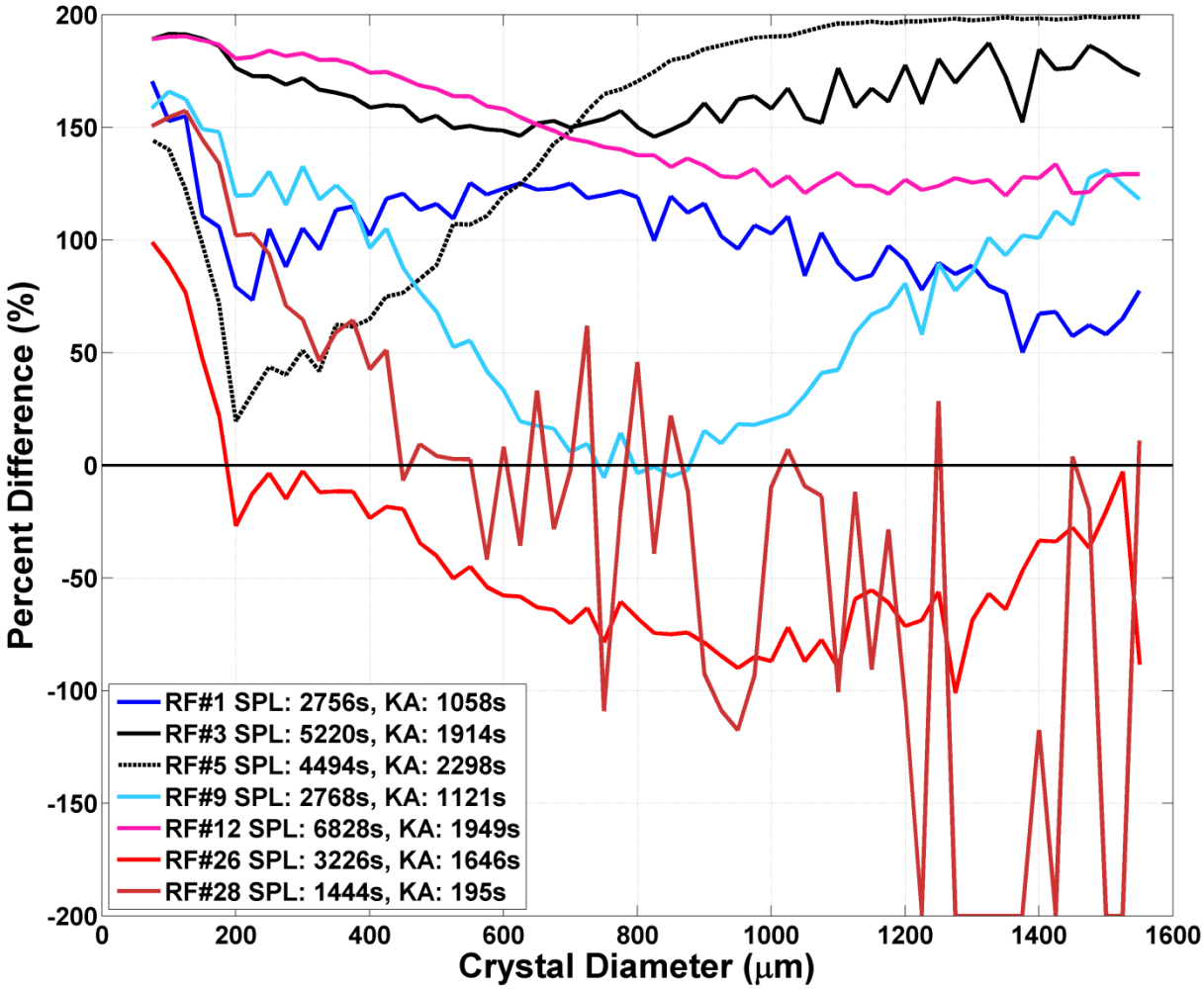

Figure 28. Percent difference between SPL and the upwind UWKA below 4700 meters crystal size distributions (75-1550 microns). Positive (negative) percent difference indicates higher concentrations at SPL (on the UWKA). Convective cases are in red, hybrid cases are in blue and wave cases are in grey hues.

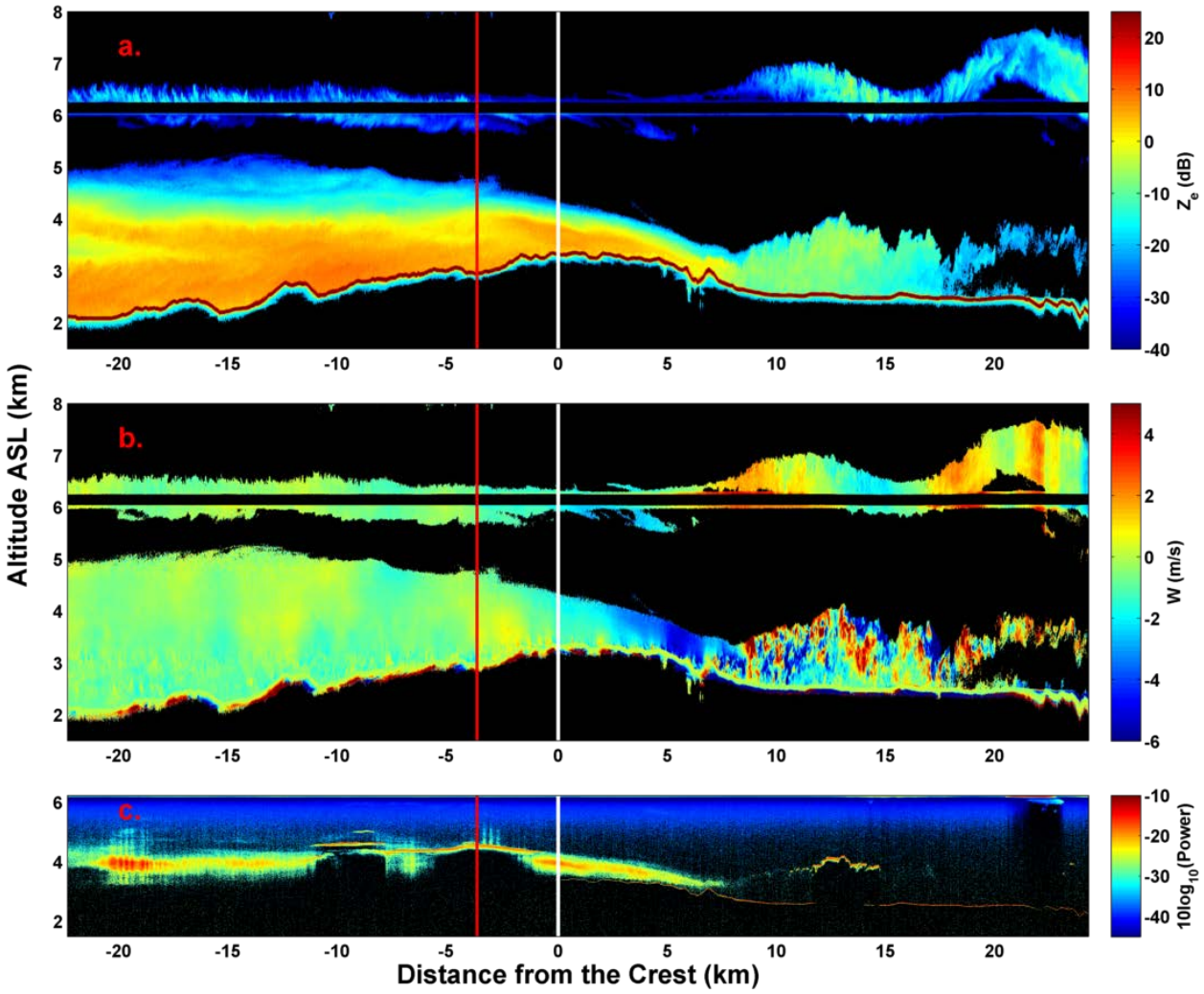

Figure 29. WCR reflectivity (a.) vertical velocity (b.) and WCL power (c.) for RF#3. The white line represents the location of the crest and the red line is SPL.

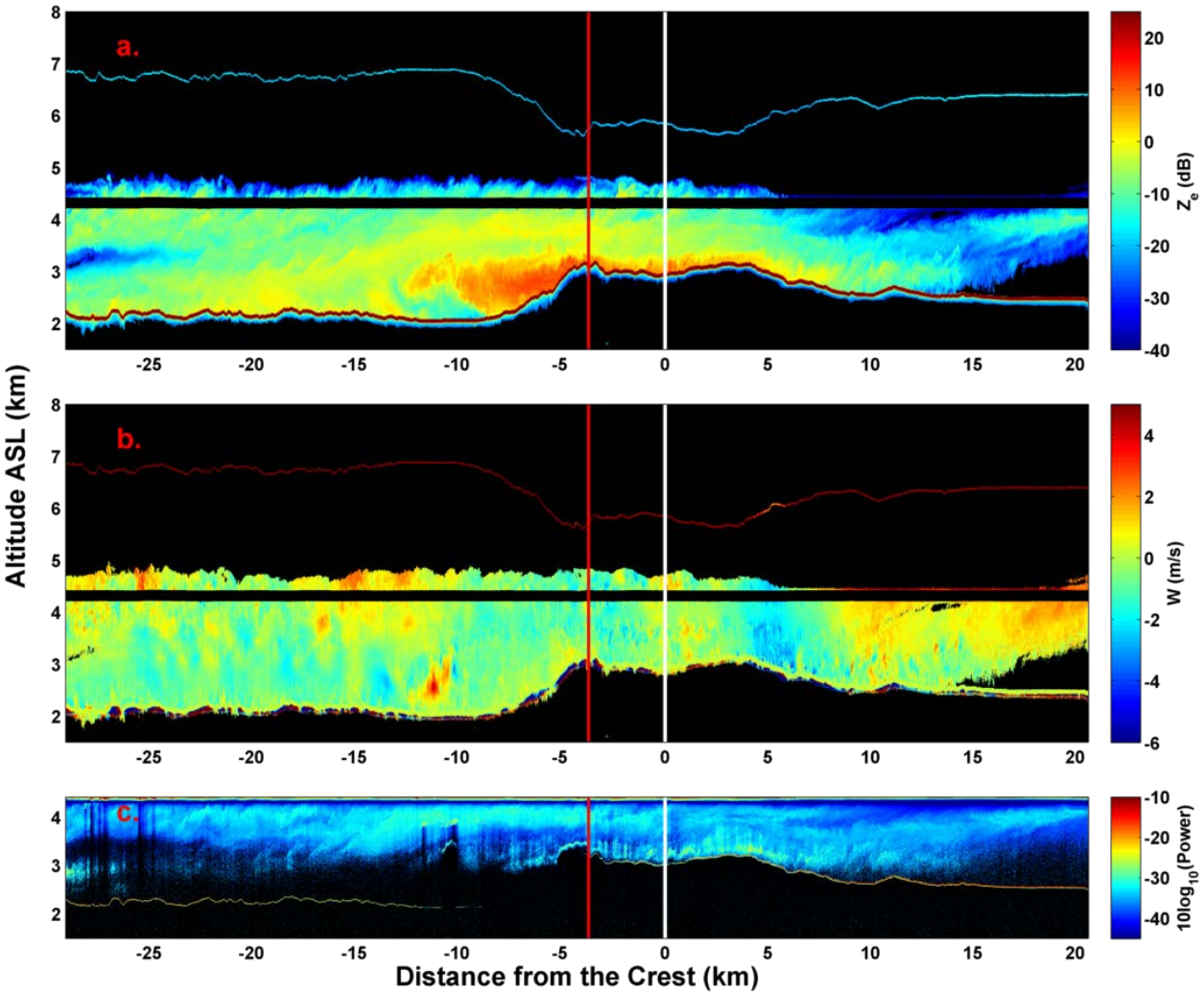

Figure 30. Same as Figure 29 except for during RF#5.

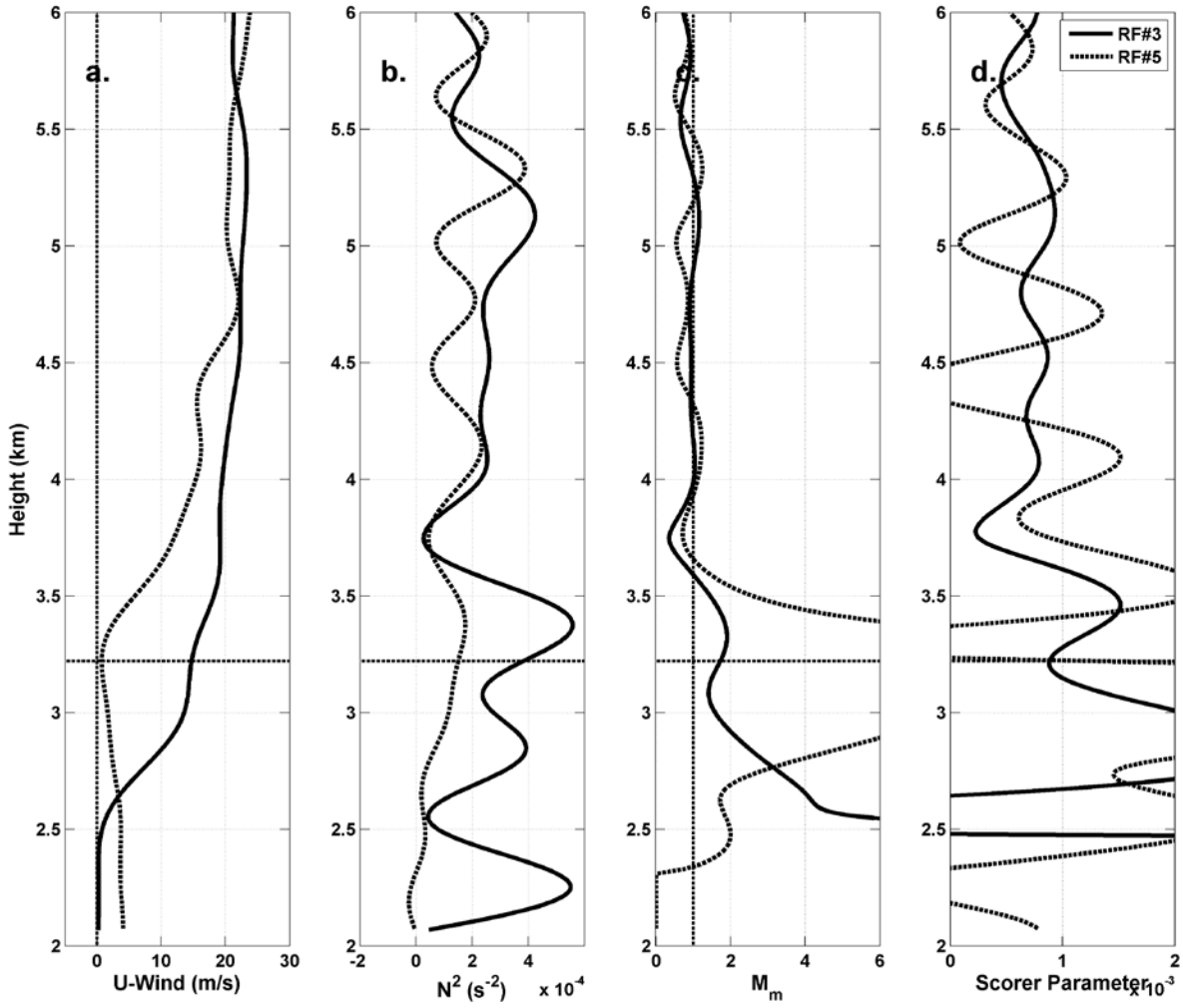

Figure 31. Sounding based profiles of U-Wind Speed in m/s (a.), Moist Static Stability (b.), Nondimensional Mountain Height Number (c.) and Scorer Parameter (d.) for RF#3 and 5.

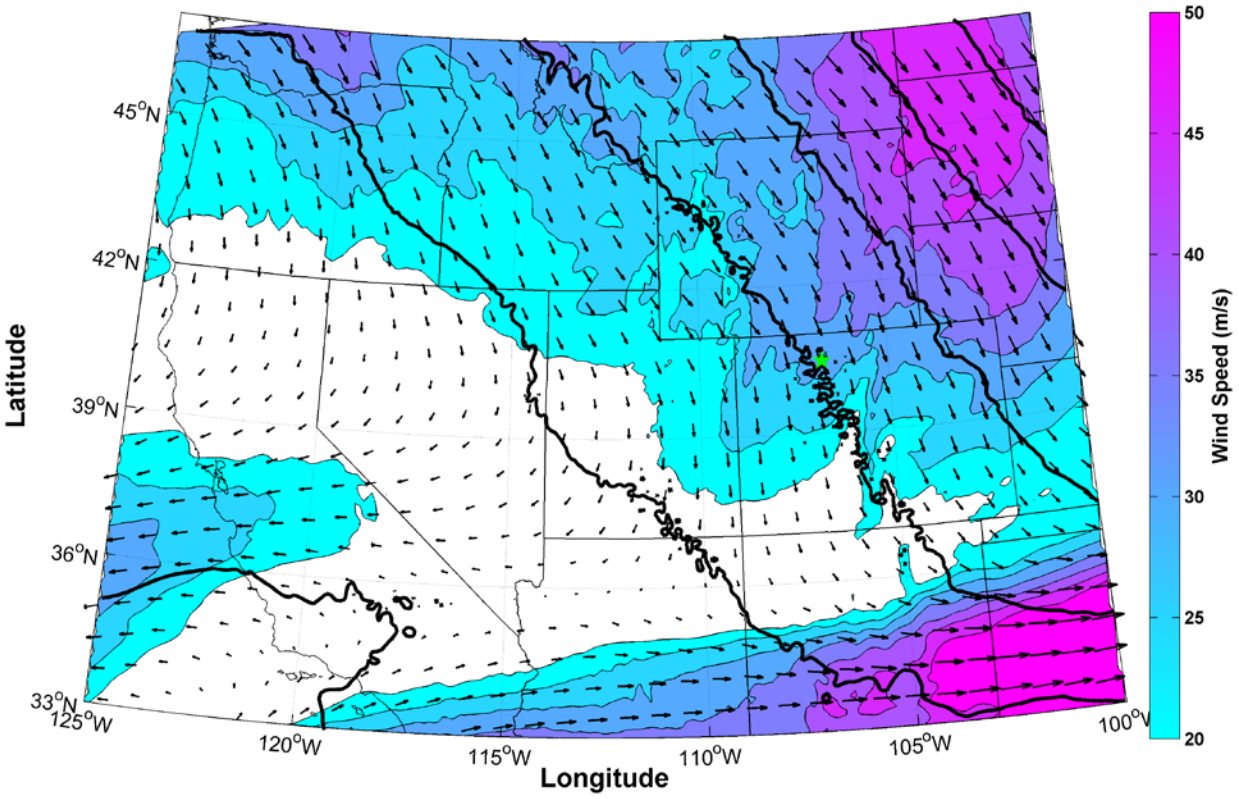

Figure 32. Model-derived 300 hPa wind speed (color fill), height (black contours) and direction (arrows) just before RF#3. The green star represents the location of SPL.

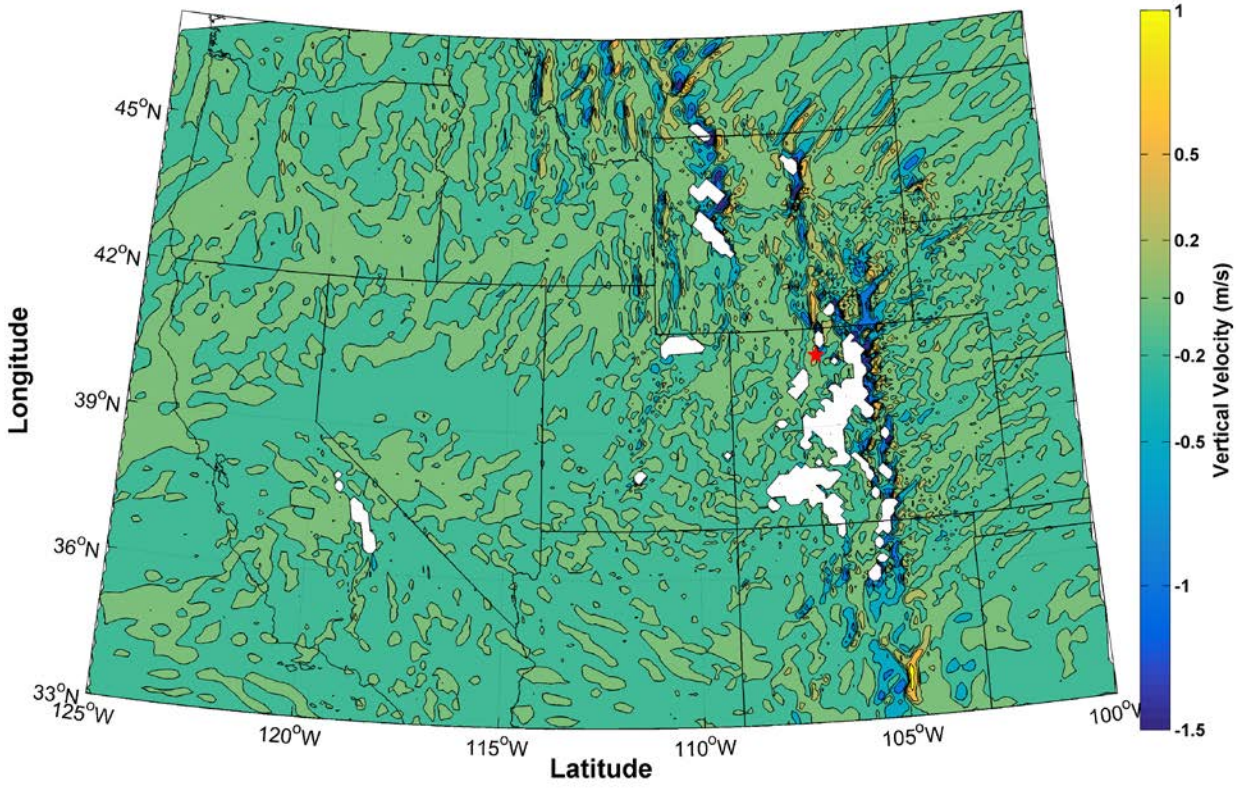

Figure 33. Model-derived 700 hPa vertical velocity right before RF#3. The red star represents the location of SPL.

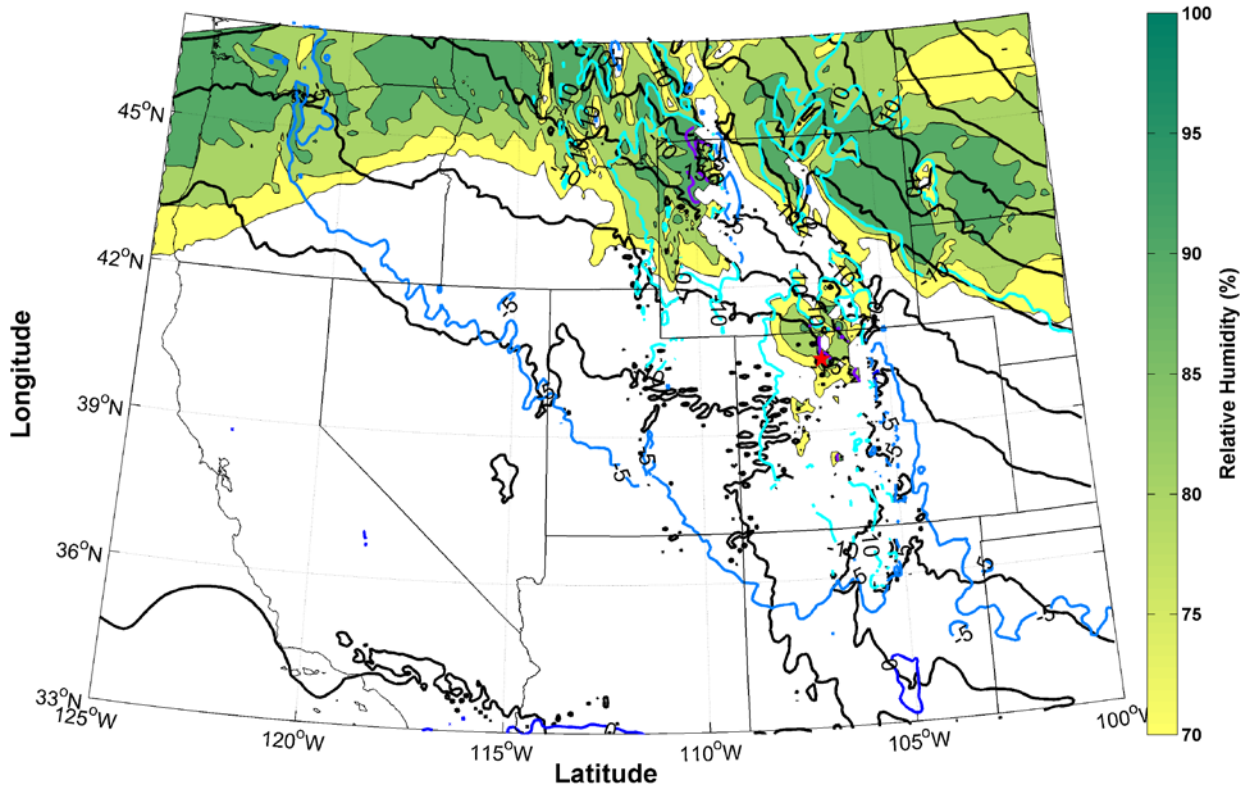

Figure 34. Model-derived 700 hPa height (black contours), relative humidity (color fill) and temperature (colored contours) just before RF#3. The red star represents SPL.

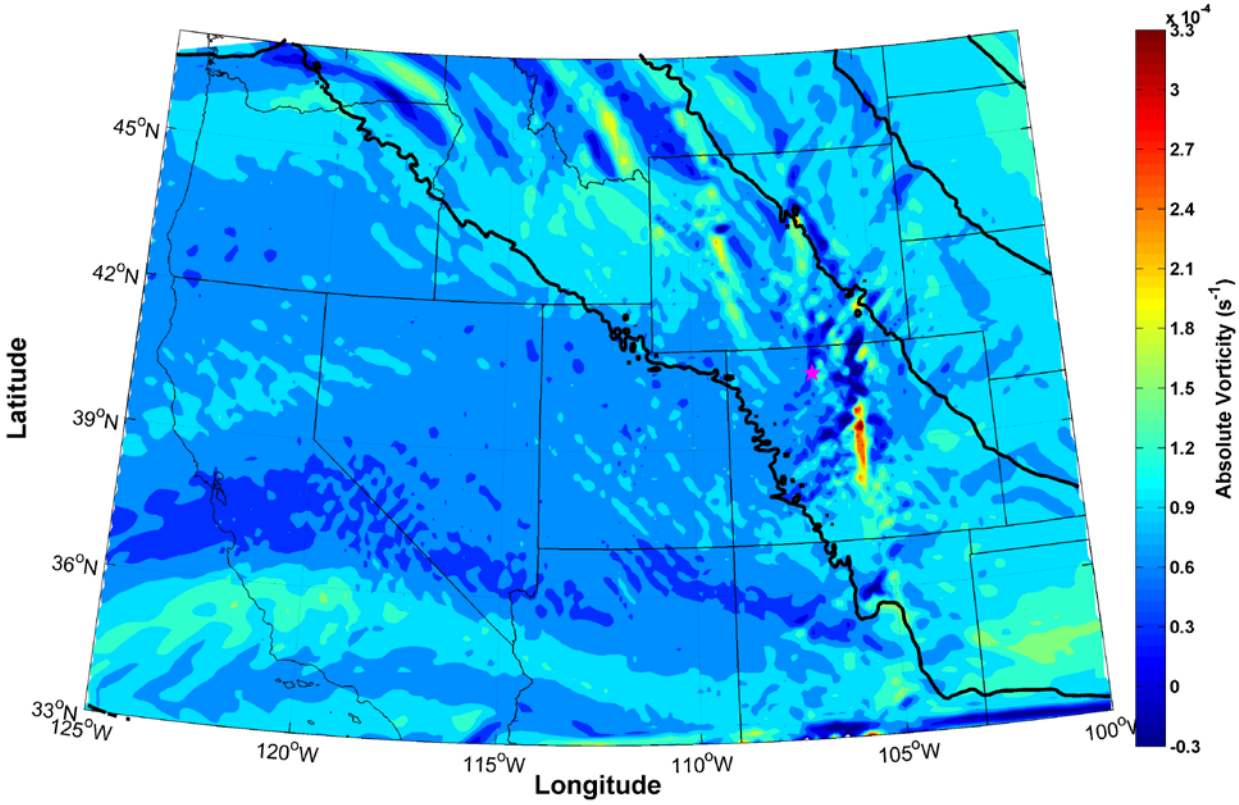

Figure 35. Model-derived 500 hPa absolute vorticity (color fill) and height (black contours). The magenta star represents the location of SPL.

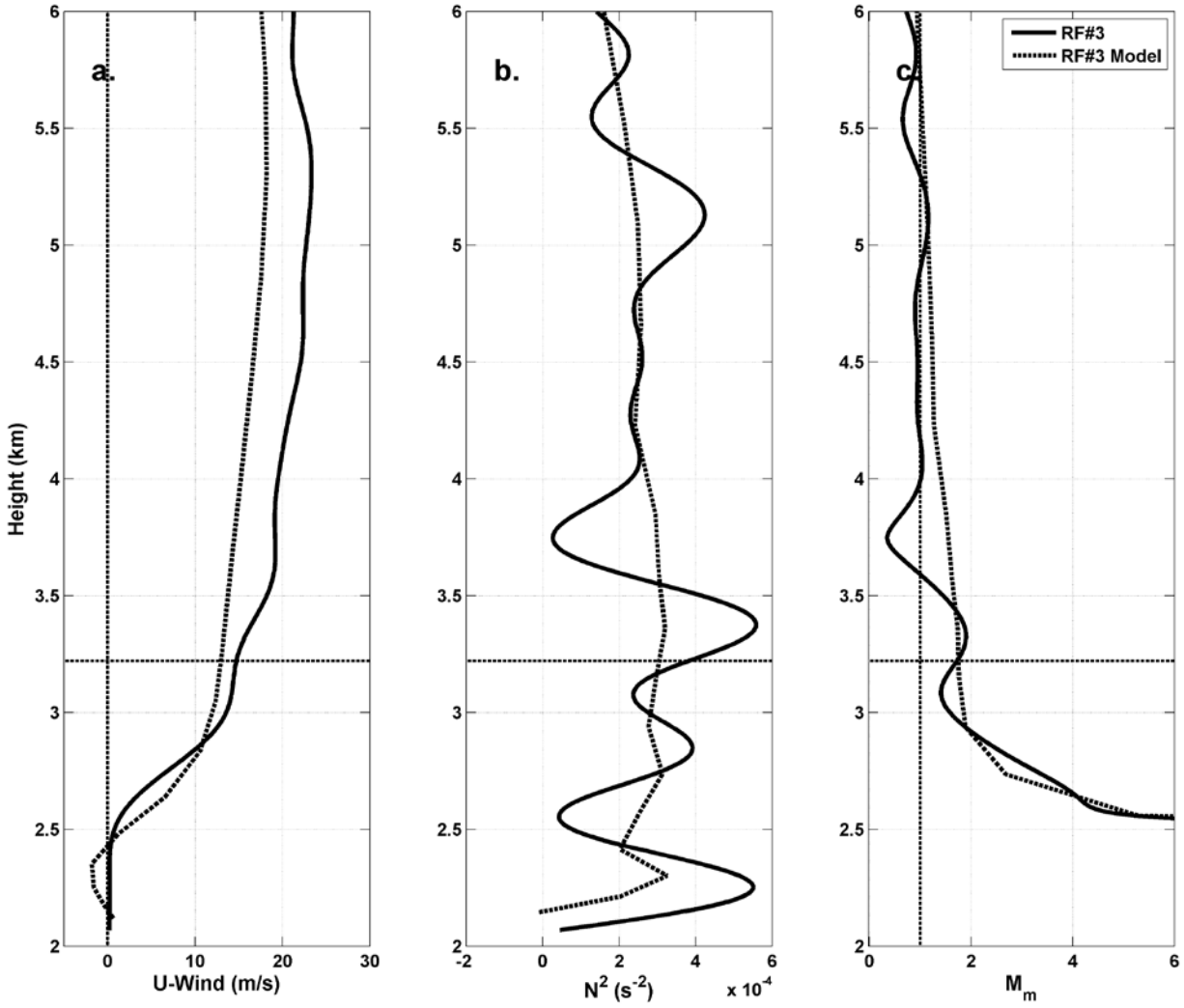

Figure 36. Model-derived (dotted line) and observed (solid line) vertical profiles of u-wind speed (a.), static stability (b.) and Mm (c.) during RF#3. The horizontal dotted line represents the altitude of SPL.

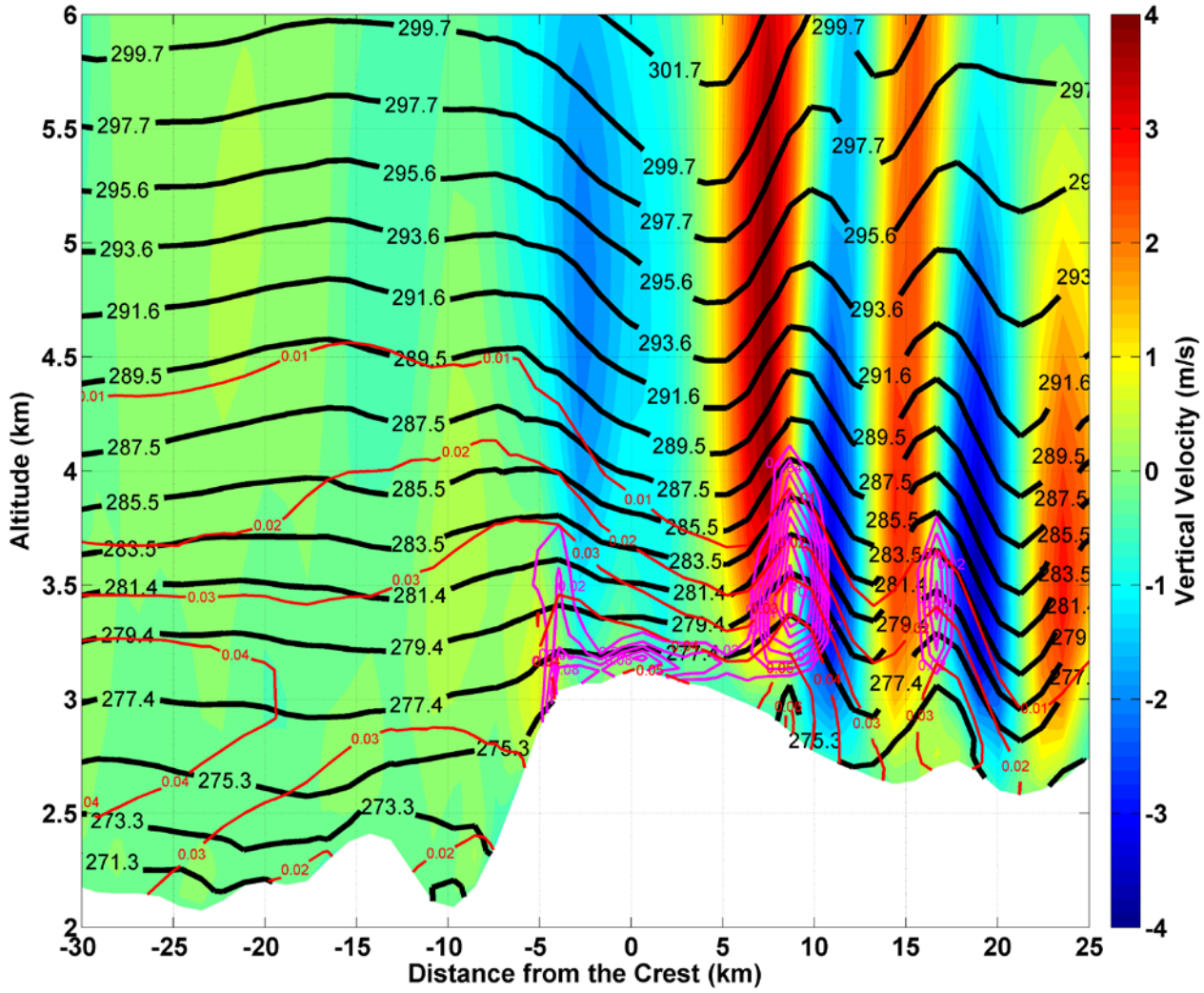

Figure 37. Model-derived vertical cross-section of theta (black contours), vertical velocity (color fill), LWC (magenta contours) and IWC (red contours) during RF#3 over the Park Range at the latitude of SPL.

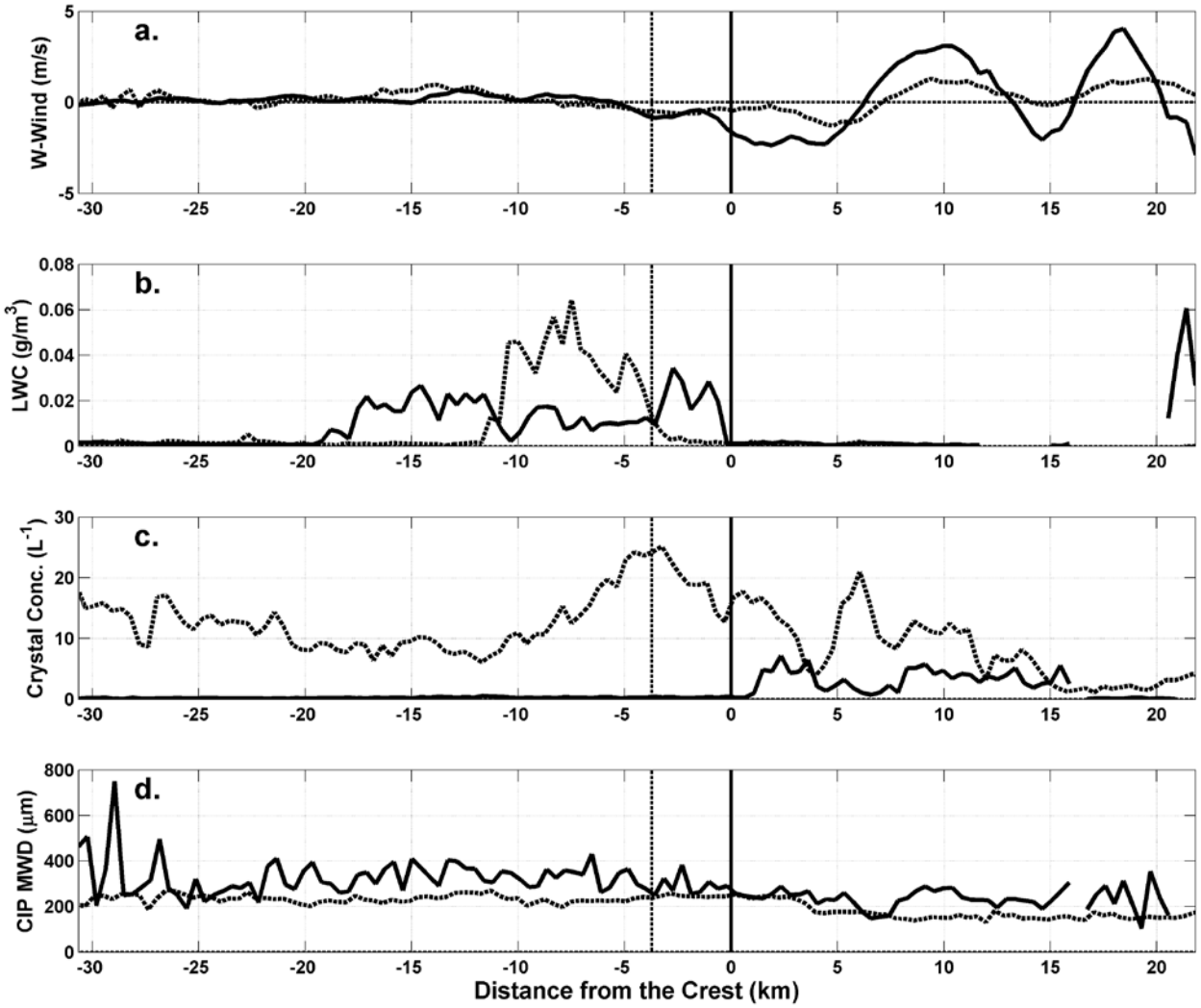

Figure 38. Profiles of vertical velocity (a.), liquid water content in g/m3,(b.), crystal concentration (75-1550 microns) (L-1) (c.), and mean weighted diameter for crystals (75-1550 microns) in microns (d.) from RF#3 (solid black line) and RF#5 (dotted black line) over the Park Range. The black vertical line represents the crest and the black dotted line represents the location of SPL.

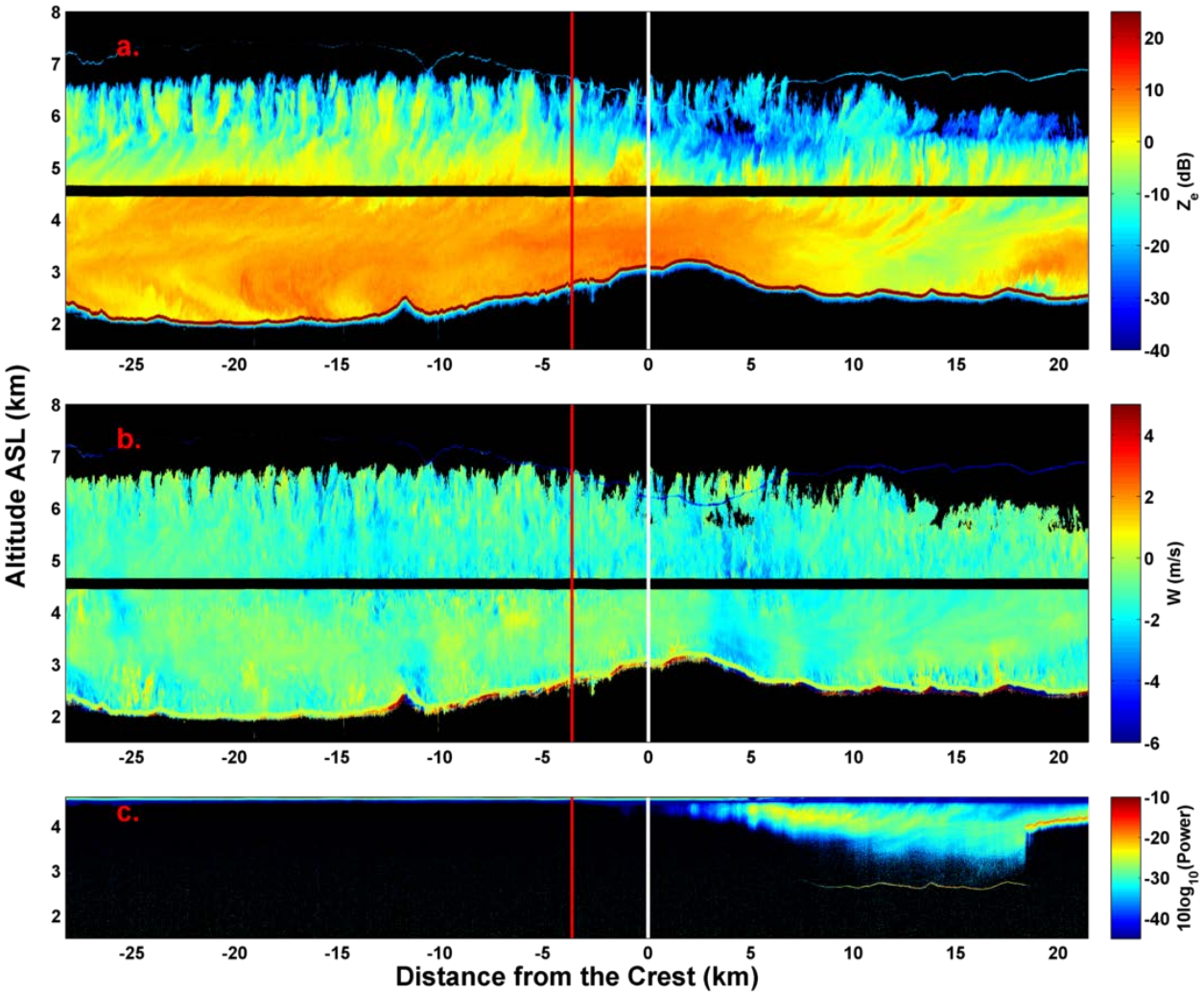

Figure 39. WCR-derived reflectivity (a.) vertical velocity (b.) and WCL power (c.) during RF#1. The white line represents the location of the crest and the red line is SPL.

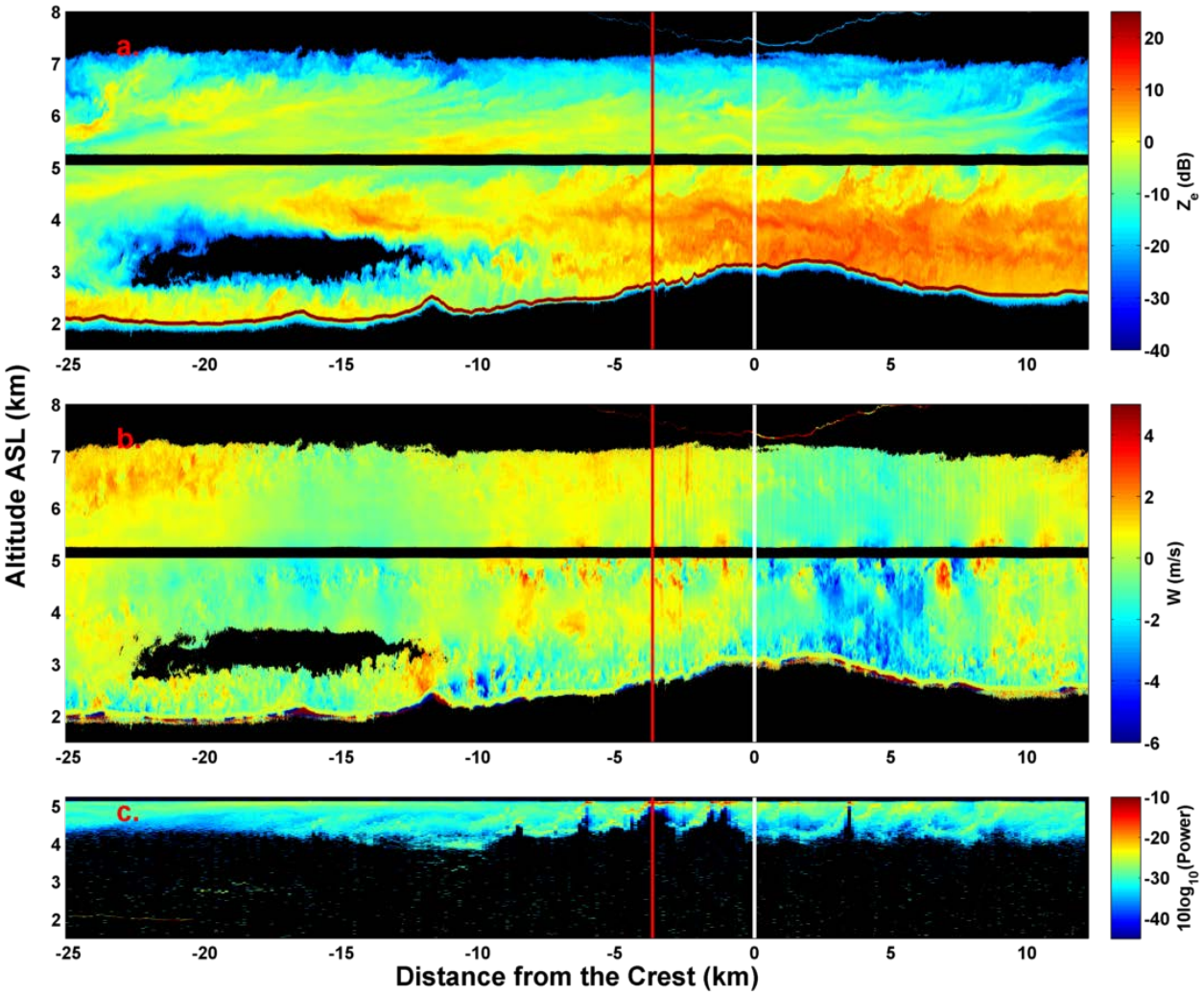

Figure 40. Same as Figure 39 except for during RF#9.

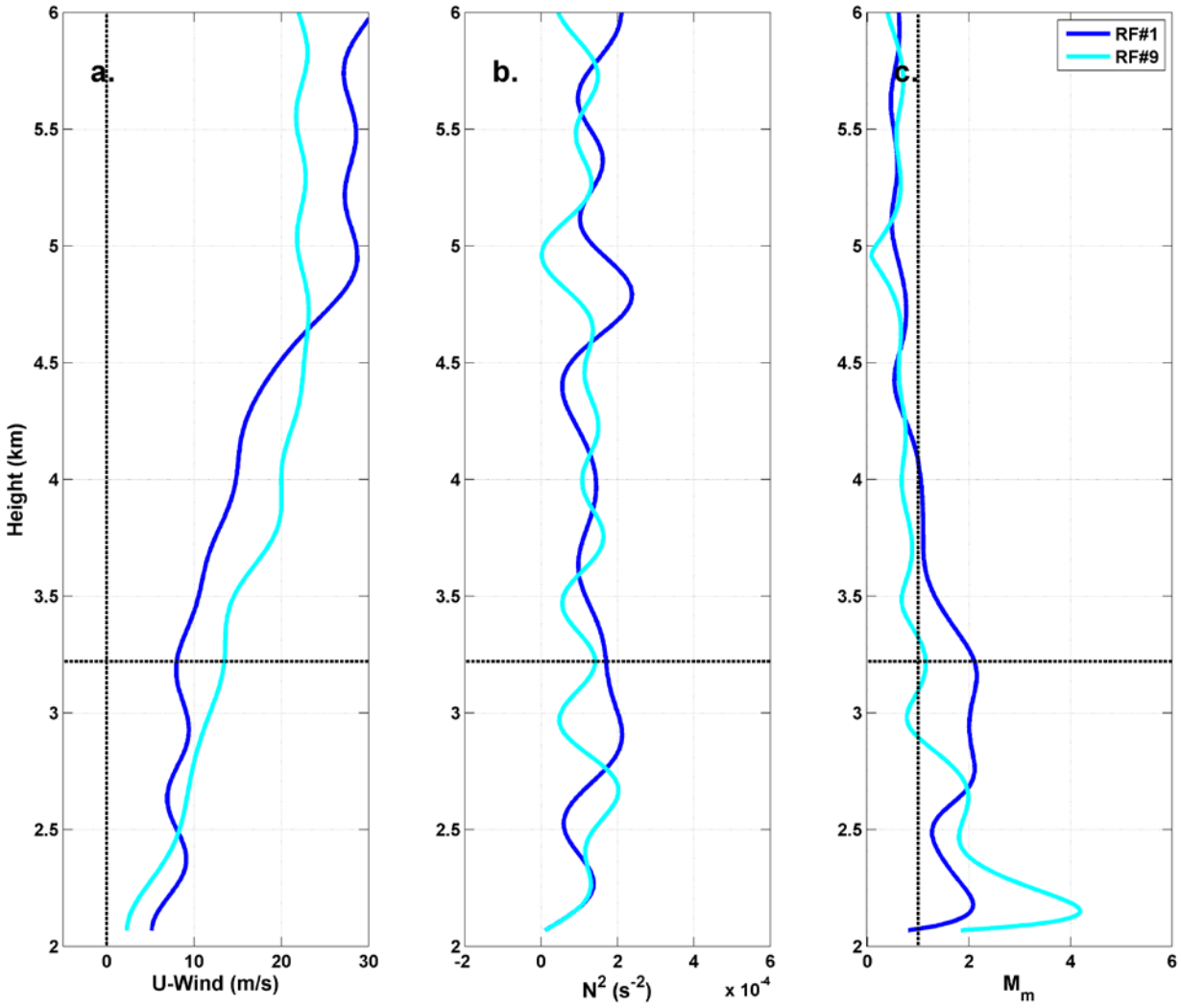

Figure 41. Sounding based profiles of U-Wind Speed in m/s (a.), Moist Static Stability (b.), M_m (c.) for RF#1 (blue) and RF#9 (cyan).

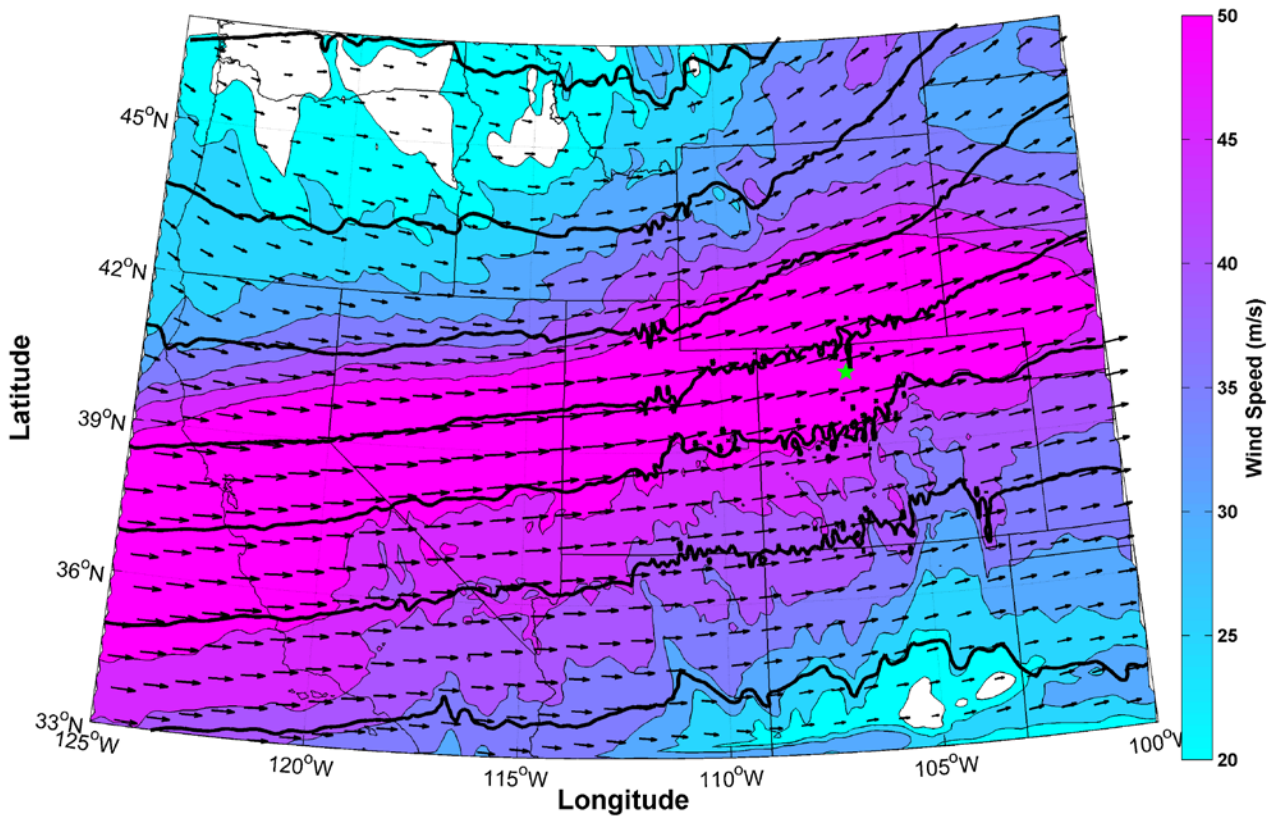

Figure 42. Model-derived 300 hPa wind speed (color fill), direction (arrows) and height (black contours) during RF#1. The green star represents the location of SPL.

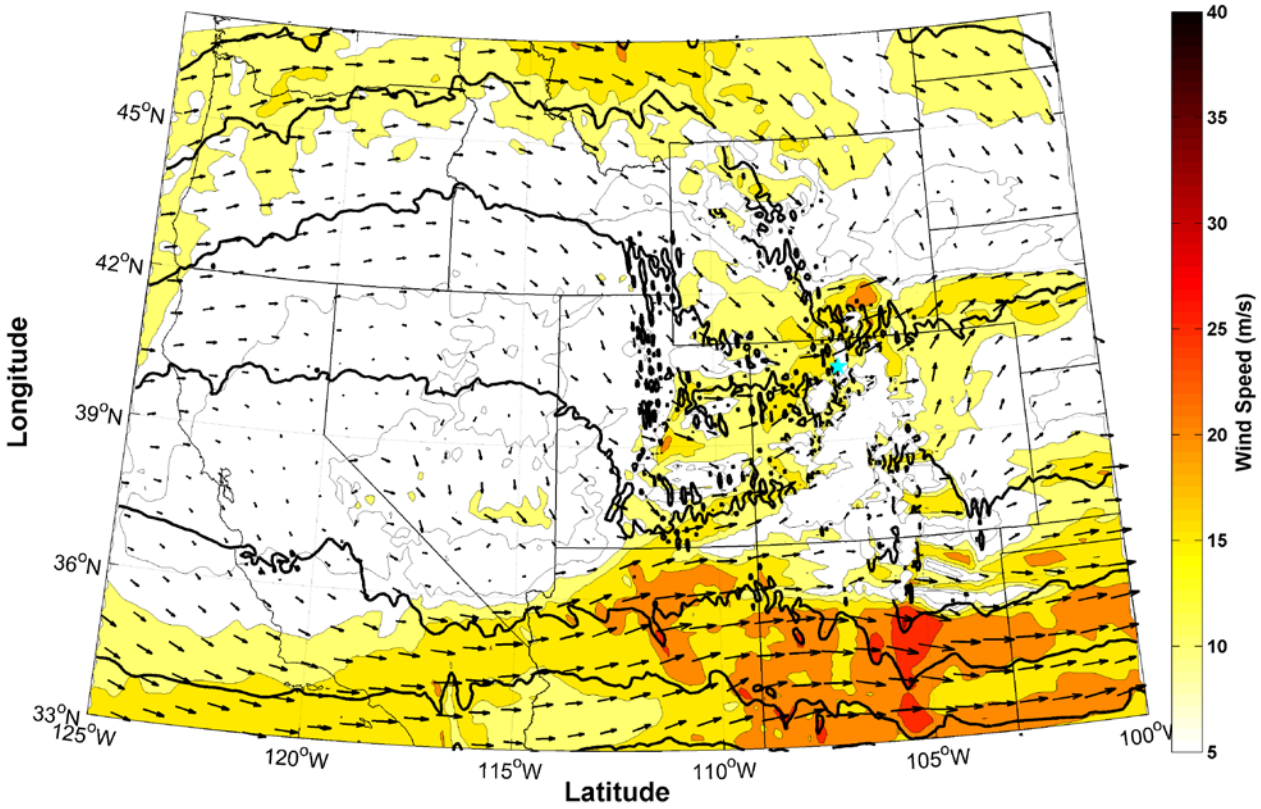

Figure 43. Same as Figure 42 except for at the 700 hPa layer.

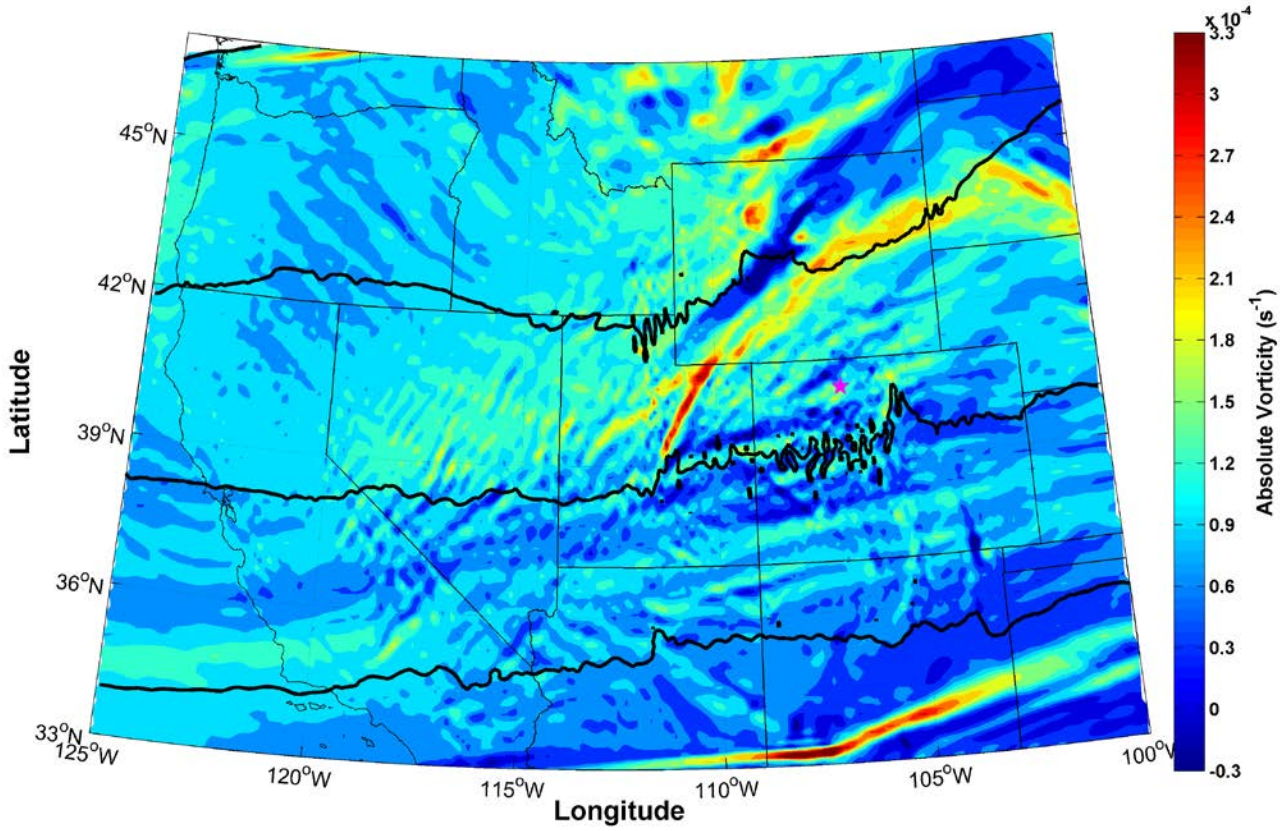

Figure 44. Model-derived 500 hPa absolute vorticity (color fill) and height (black contours) during RF#1. The red star represents the location of SPL.

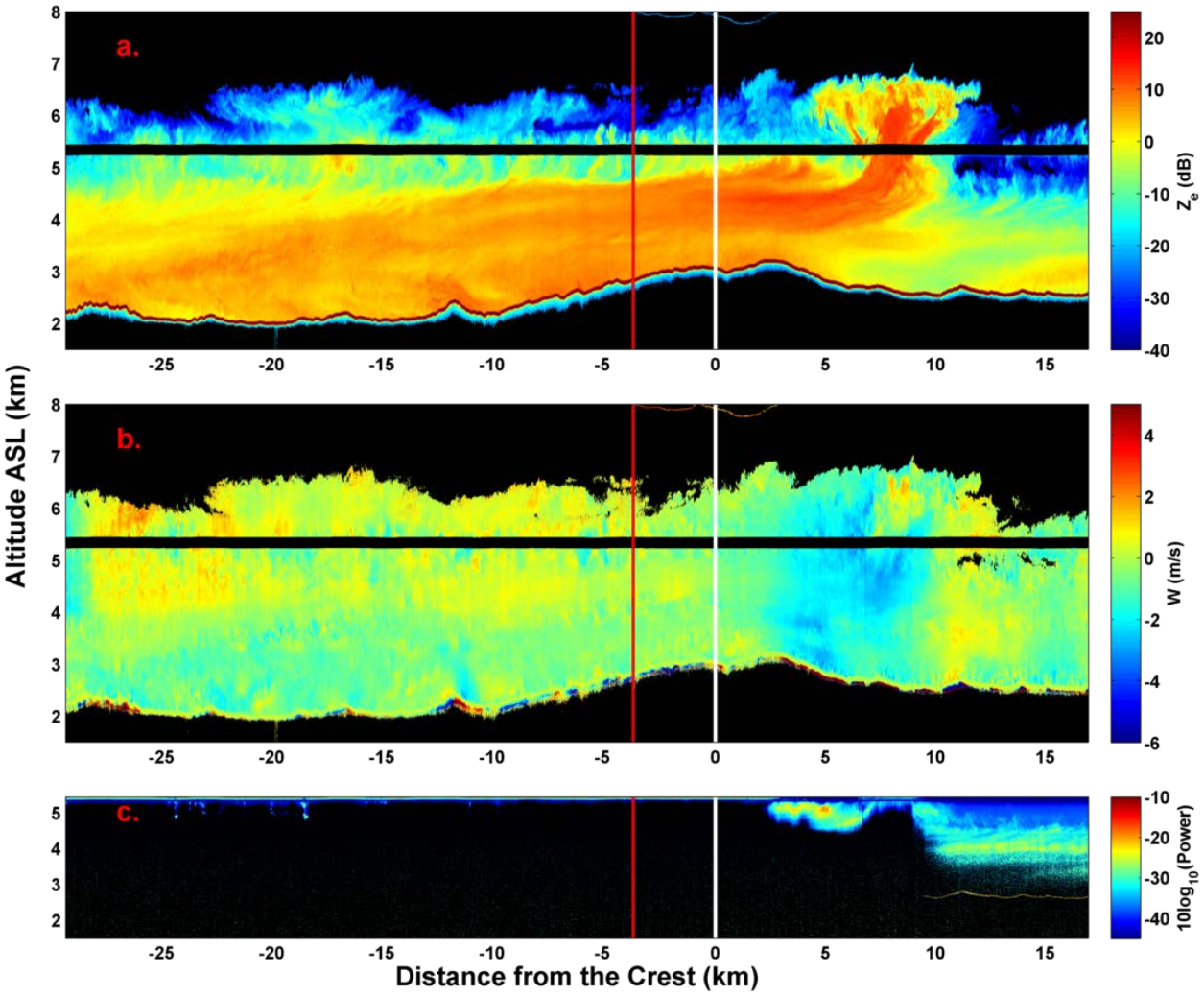

Figure 45. WCR-derived reflectivity (a.) vertical velocity (b.) and WCL power (c.) while the UWKA flew over an enhanced precipitation band during RF#1. The white line represents the location of the crest and the red line is SPL.

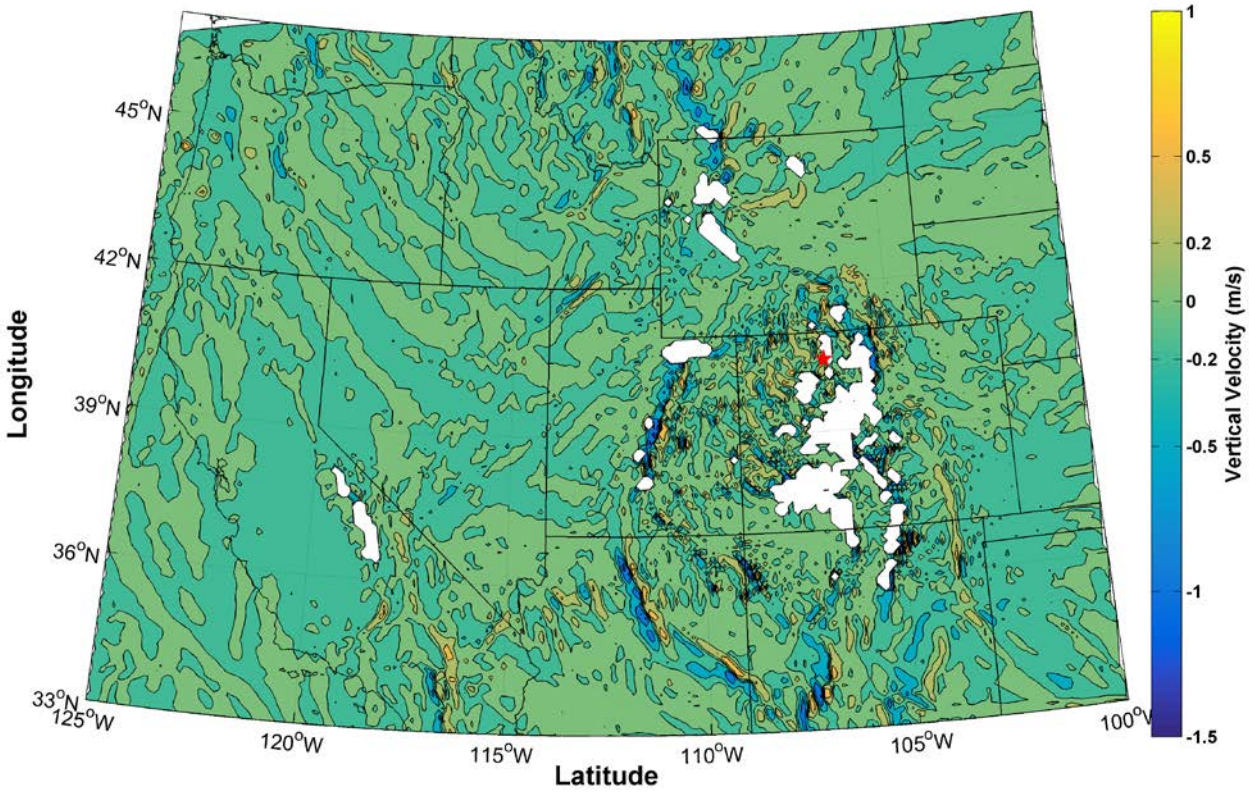

Figure 46. Model-derived 700 hPa vertical velocity (color fill). The red stare indicates the location of SPL.

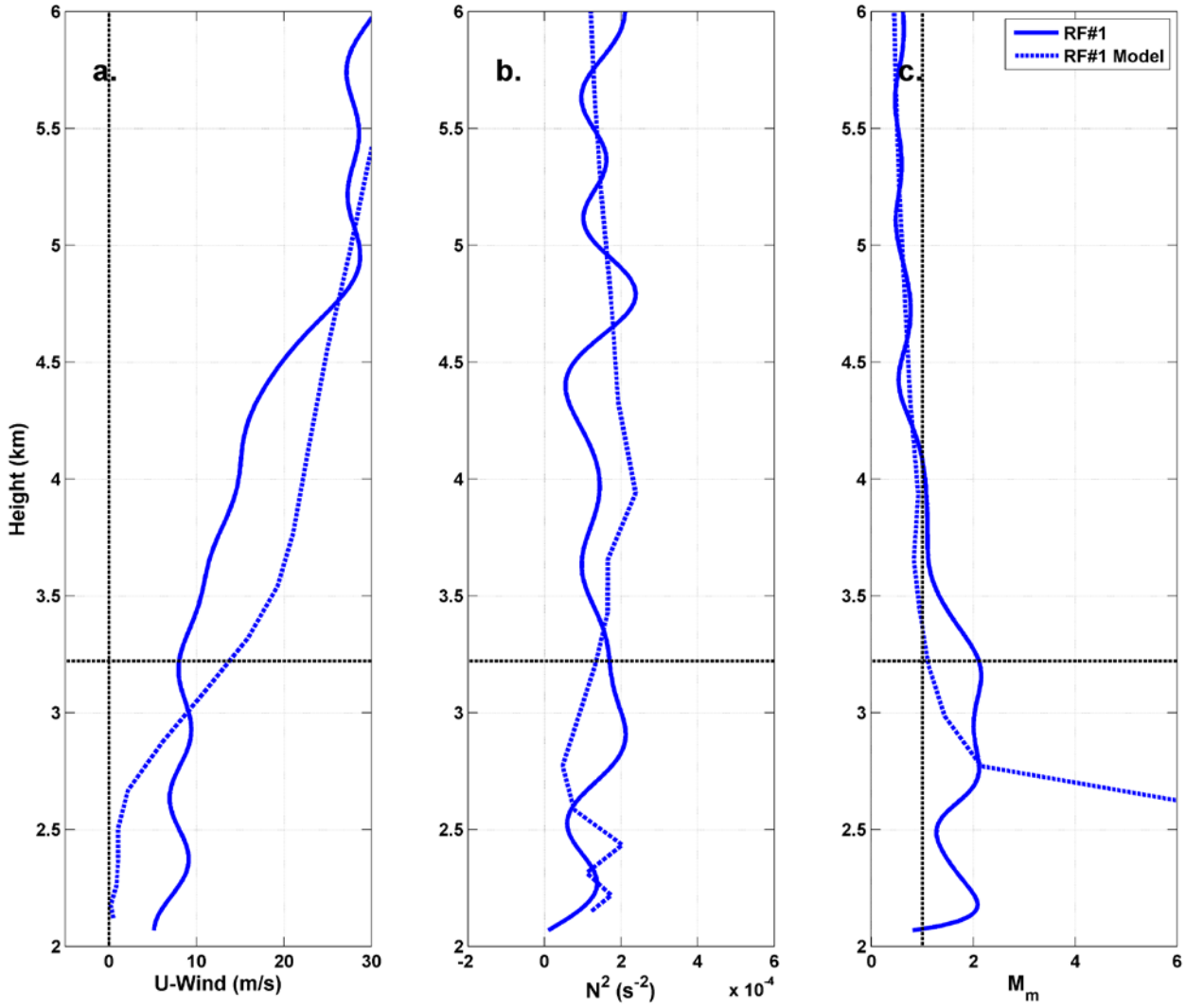

Figure 47. Model-derived (dotted blue line) and observed (solid blue line) vertical profiles of the u-component of the wind (a.), static stability (b.) and M_m (c.) right before RF#1. The dotted black horizontal line represents the elevation of SPL.

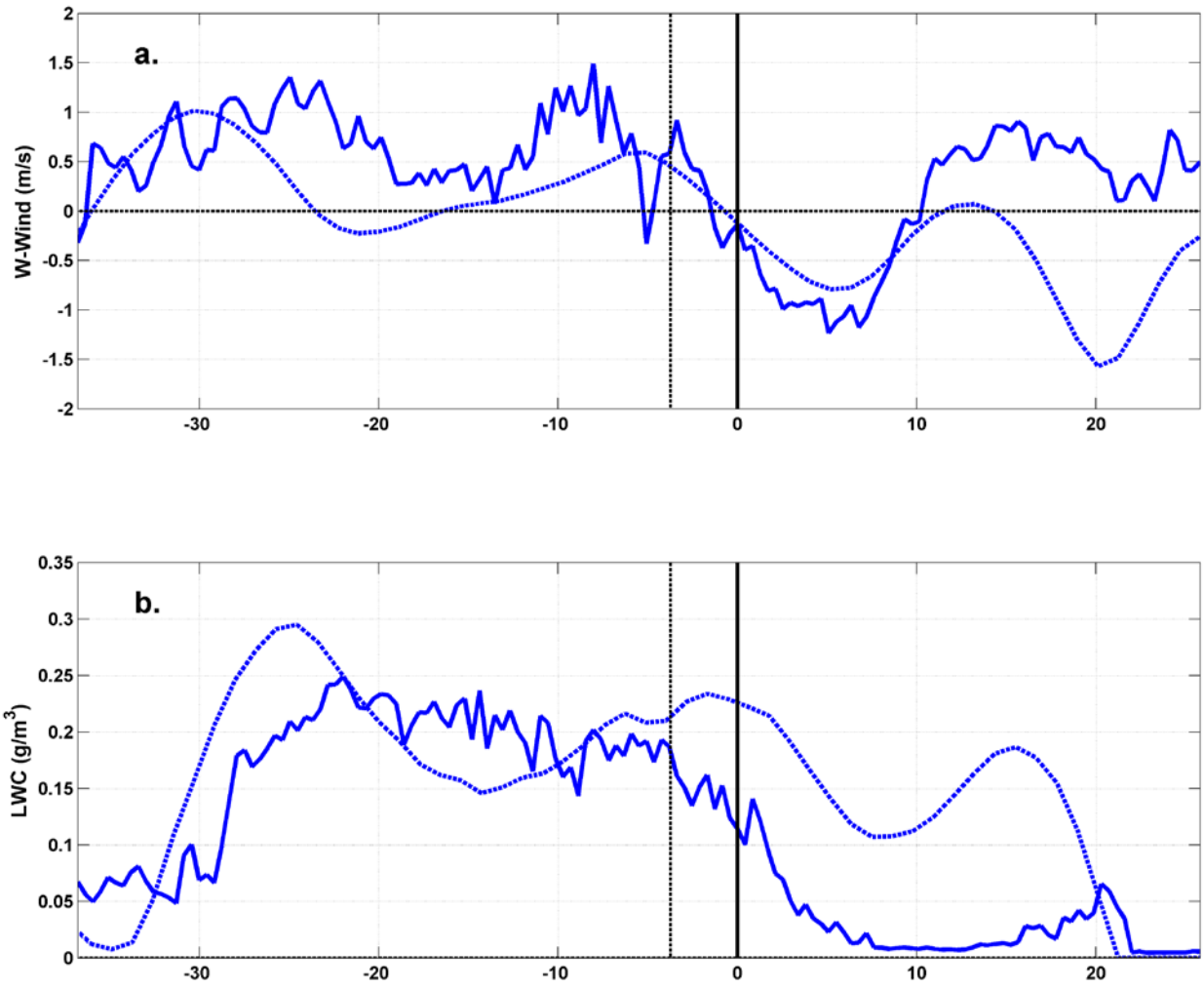

Figure 48. Model-derived (dotted blue line) and observed (solid blue line) cross-barrier profiles of vertical velocity (a.) and LWC (b.) during RF#1. The solid vertical line is the location of the crest and dotted vertical line is the location of SPL.

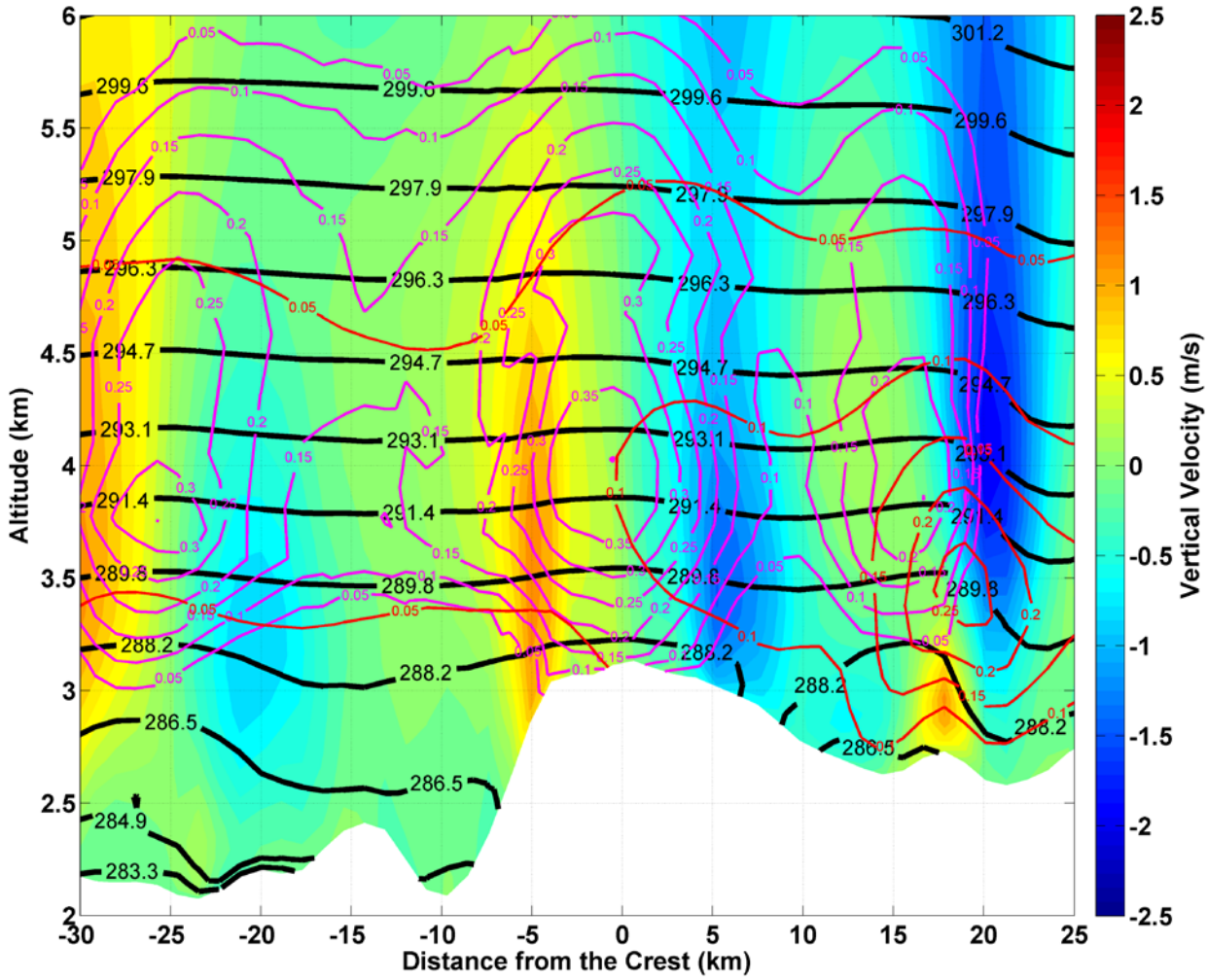

Figure 49. Model-derived vertical cross sections of theta (black contours), vertical velocity (color fill), LWC (magenta contours), and IWC (red contours) over the Park Range at the latitude of SPL.

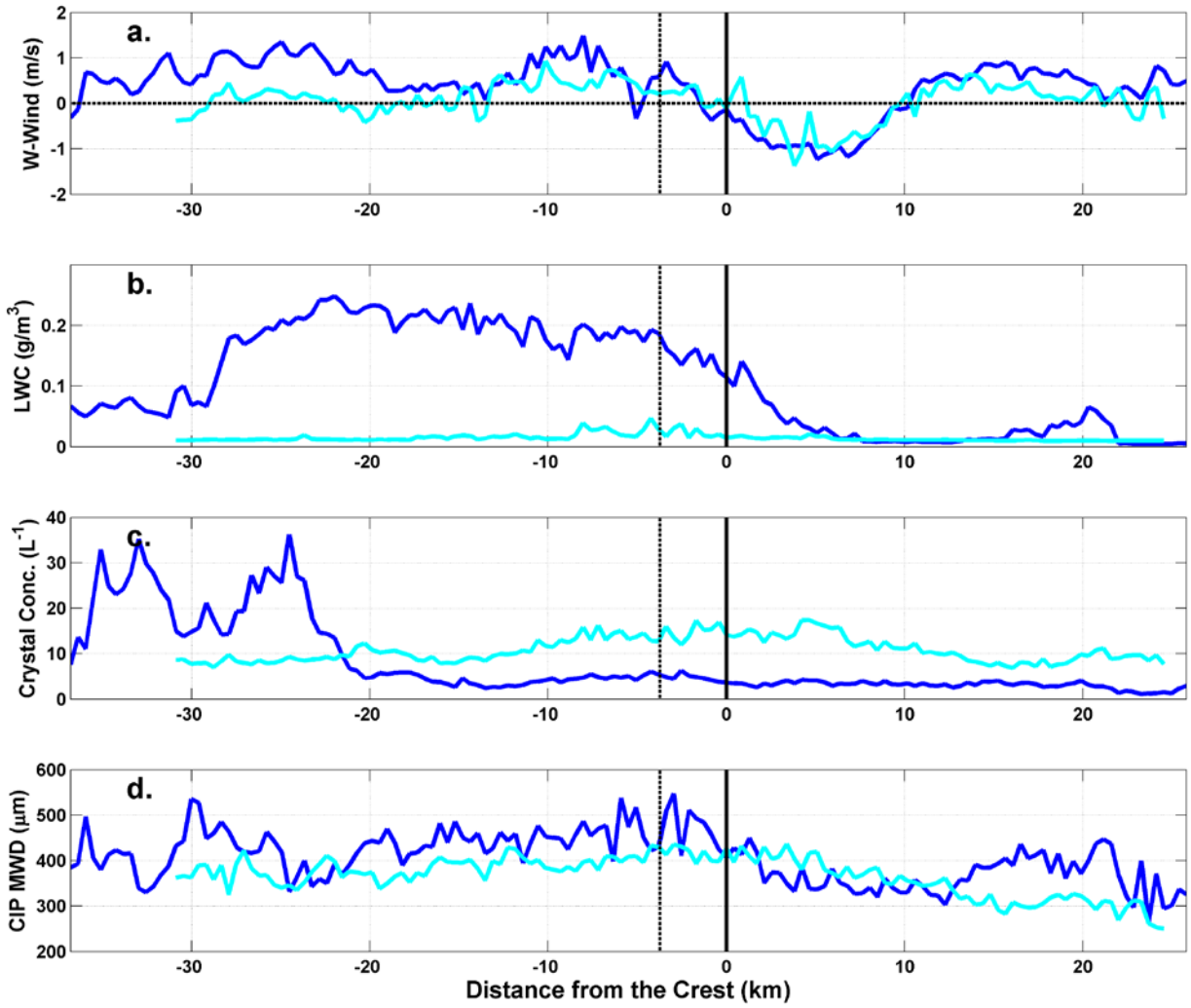

Figure 50. Average cross-barrier profiles of vertical velocity (a.), LWC (b.), crystal concentration for crystals between 75 and 1550 microns (c.), and mean weighted crystal diameter for crystals between 75 and 1550 microns (d.) for RF#1 (blue line) and RF#9 (cyan line) when the UWKA was below 4700 meters. The solid (dotted) black vertical line represents the location of the crest (SPL).

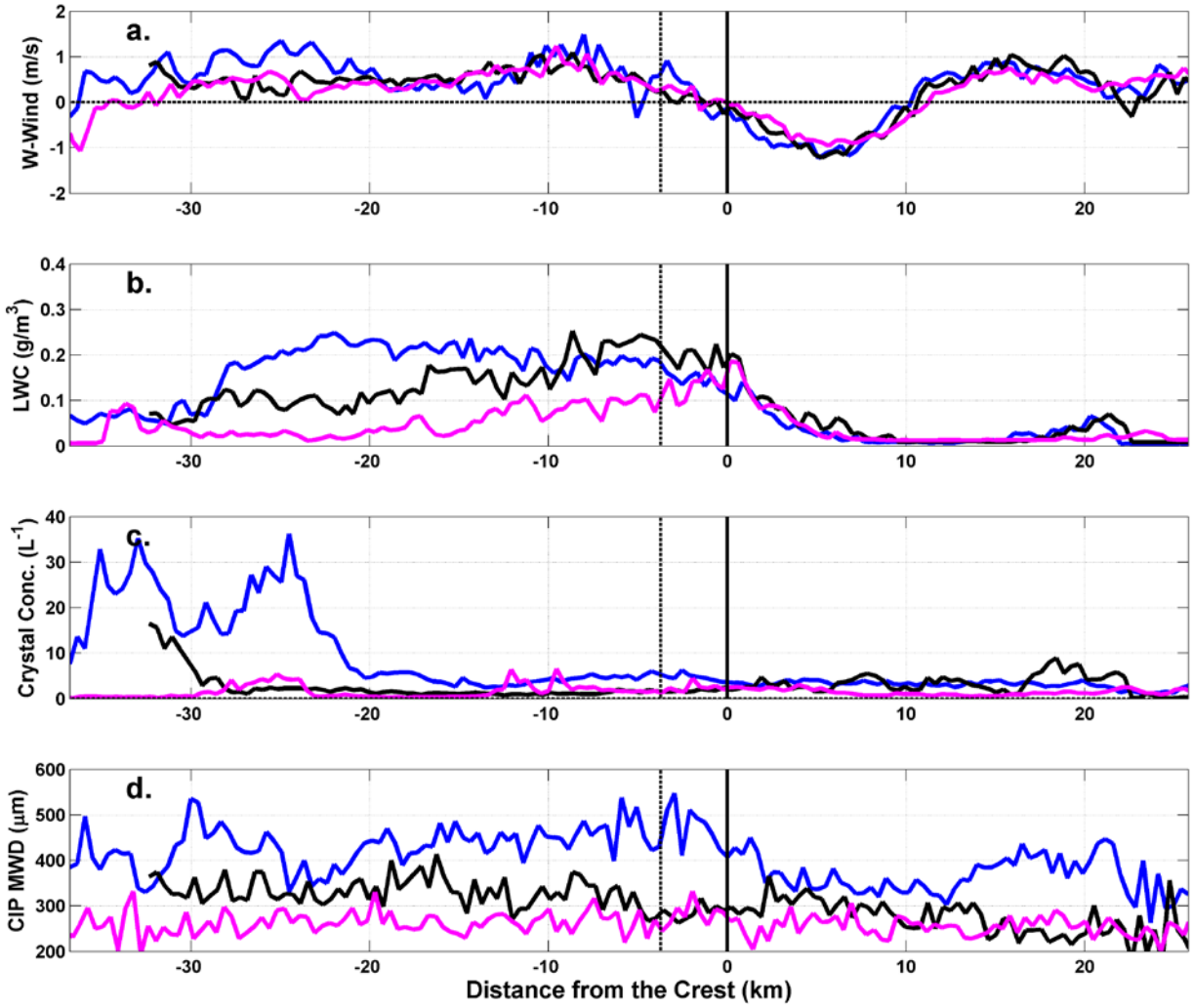

Figure 51. Profiles of vertical velocity (a.), liquid water content in g/m3,(b.), crystal concentration (75-1550 microns) (L-1) (c.), and mean weighted diameter for crystals (75-1550 microns) in microns (d.) from the crest of the Park Range for RF#1 at 4600 meters (blue line), 5200 meters (black line), and 6000 meters (magenta line).

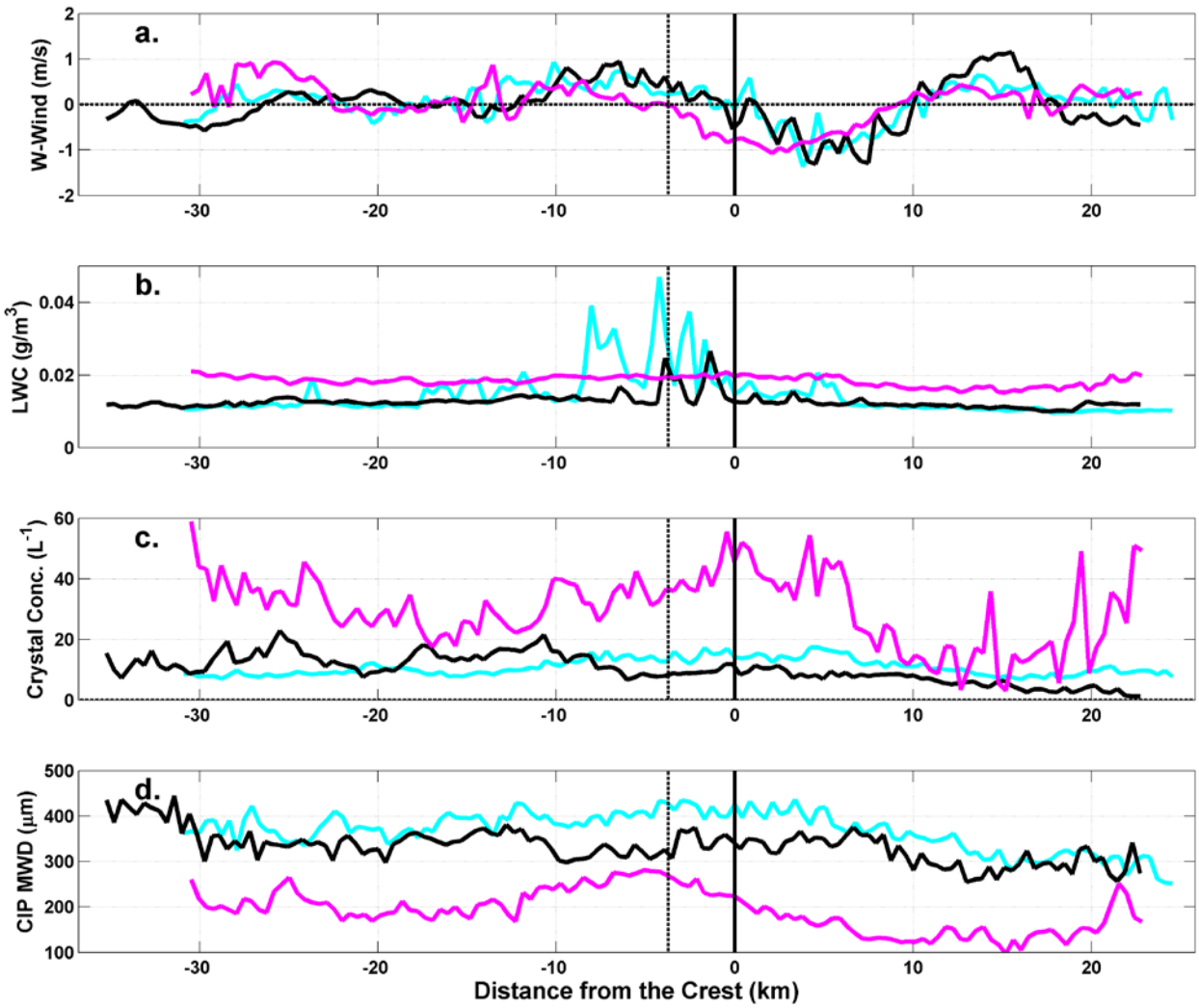

Figure 52. Profiles of vertical velocity (a.), liquid water content in g/m3,(b.), crystal concentration (75-1550 microns) (L-1) (c.), and mean weighted diameter for crystals (75-1550 microns) in microns (d.) from the crest of the Park Range for RF#9 at 4400 meters (cyan), 5200 meters (black) and 6000 meters (magenta).

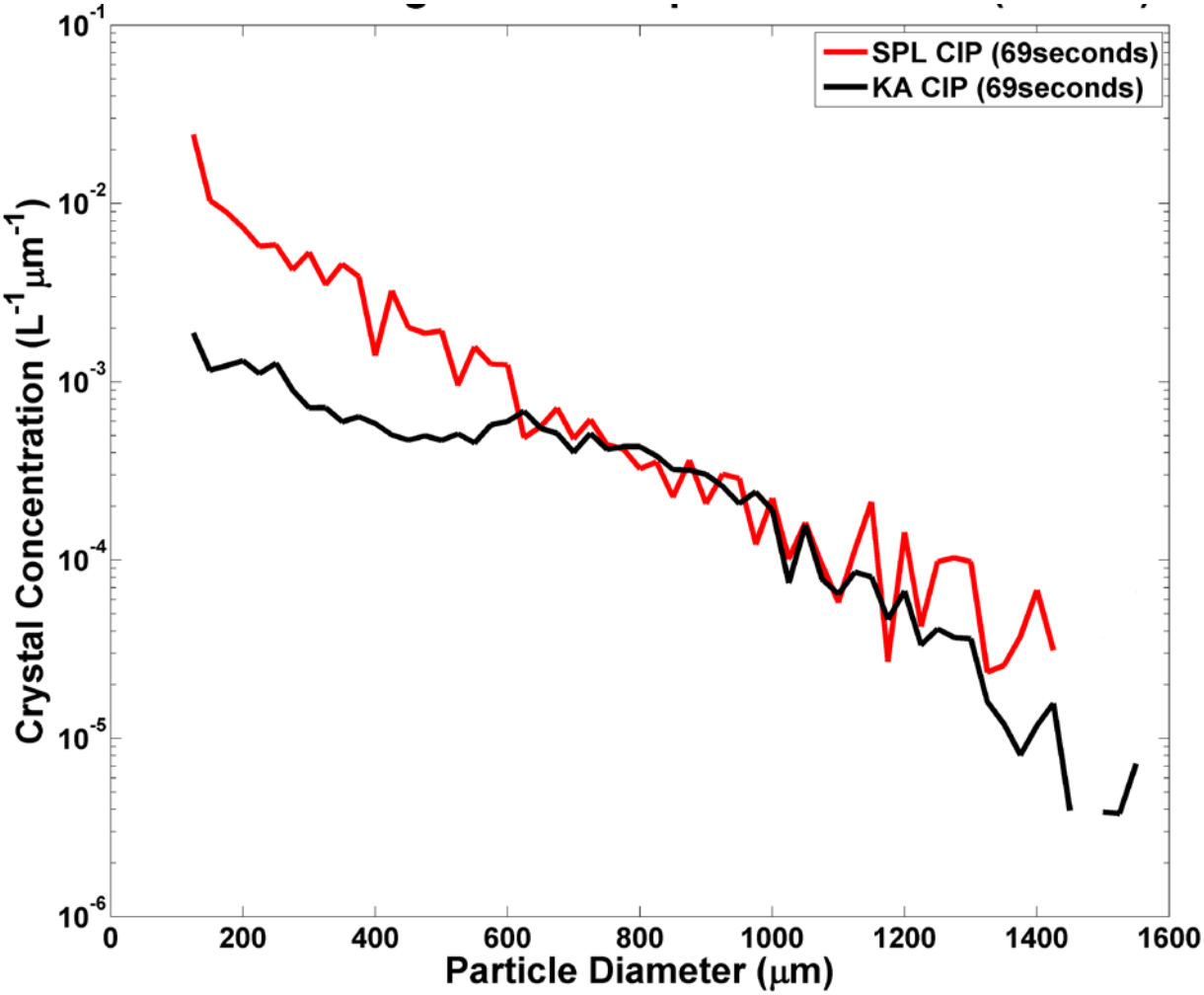

Figure 53. Comparison of the UWKA (black line) and SPL (red line) crystal size distribution based on the trajectory model for leg 7 of RF#9.

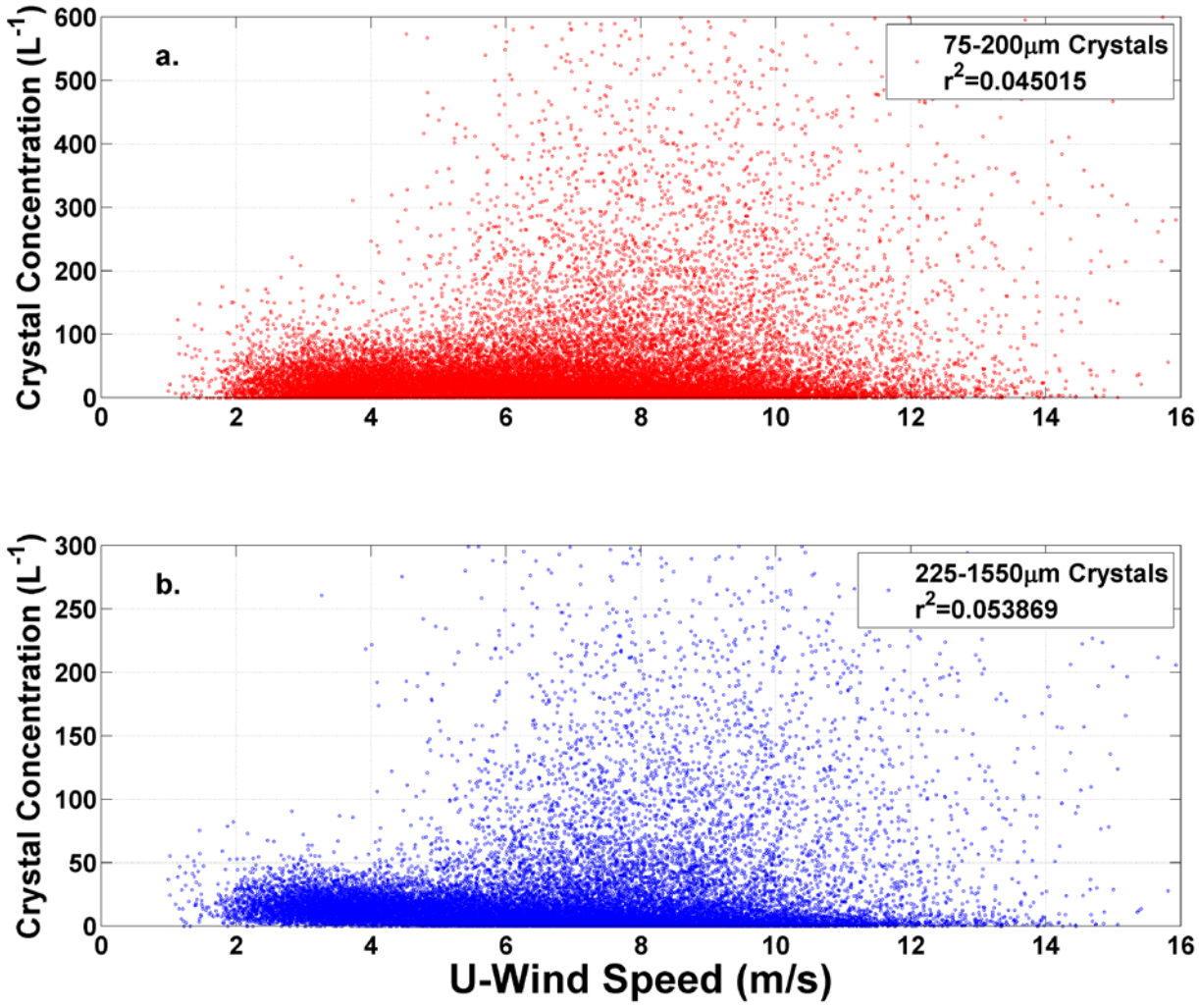

Figure 54. Comparison between crystal concentration and wind speed for crystals between 75 and 200 microns (a.) and crystals between 225 and 1550 microns (b).

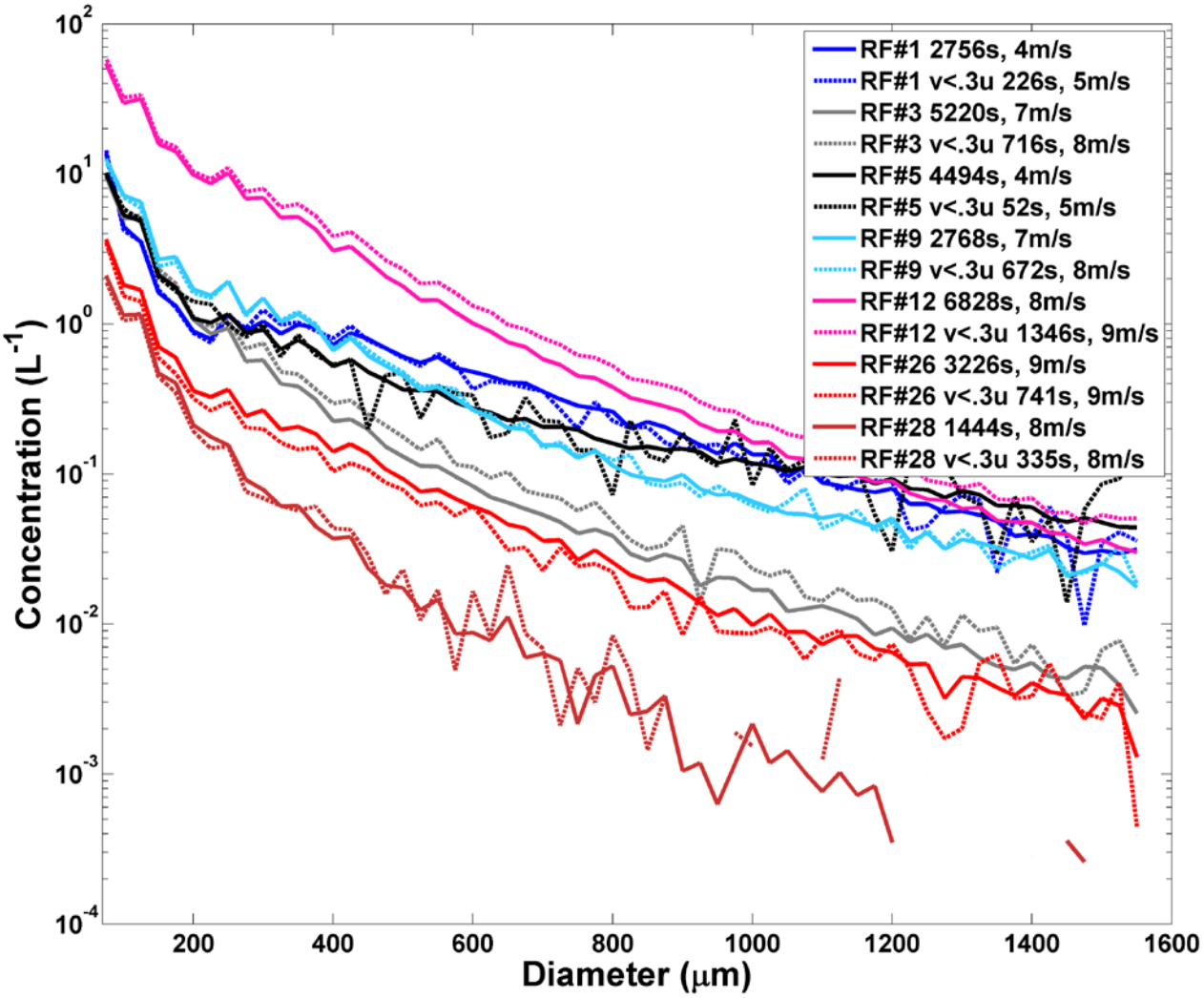

Figure 55. Impact of the swinging vane mount on the SPL crystal size distributions for each flight while the UWKA was near the lab. The solid lines include all seconds and the dashed lines are limited to seconds when the v-component of the wind is less than 30% of the u-component. The number of seconds and average wind speed are reported for each value.

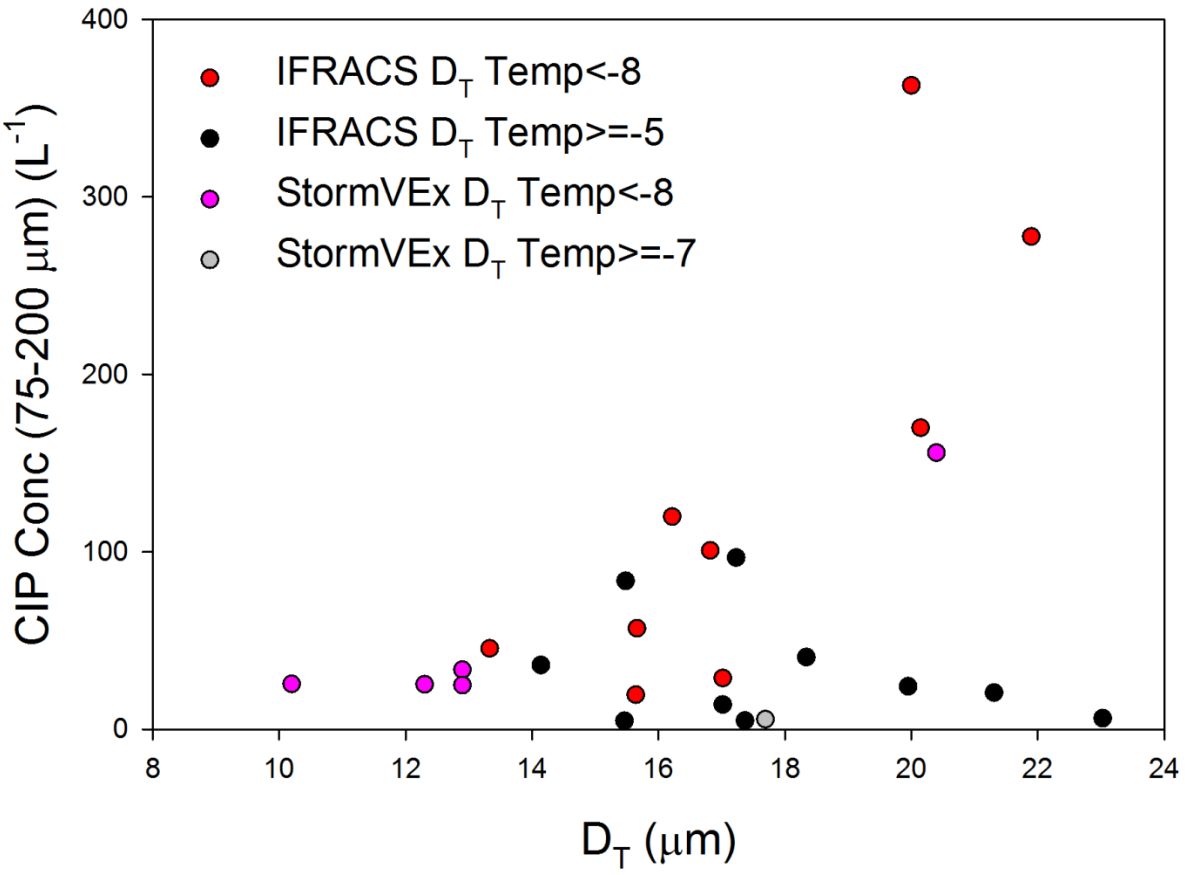

Figure 56. Comparison between average D_T and crystal concentration for crystals between 75 and 200 microns for IFRACS (red and black circles) and StormVEx (purple and grey circles).

Table 1. Description of cloud microphysical and remote sensing instruments used during CAMPS and StormVEx.

Instrument	Description	Range/Resolution	Location
DMT SPP-100 Forward Scattering Spectrometer Probe	Cloud droplet spectra	2-47 microns	UWKA and SPL
DMT Cloud Imaging Probe (CIP)	Small precipitation particle size, concentration and shape	25-1550/25 microns	UWKA and SPL
DMT Precipitation Imaging Probe (PIP)	Large precipitation particle size, concentration and shape	100-6200/100 microns	SPL
Gerber PVM-100	Liquid water content	3-50 microns, 0.002-10 g/m^3	UWKA
Colorado closed-path tunable –diode Laser Hygrometer (CLH)	Total water content	±3% (1σ)	UWKA
Balloon Borne Sounding System (BBSS)	Vertical profile of temperature, moisture and horizontal winds	Surface to 100 mb/5-20 meters	Steamboat Springs, CO
Wyoming Cloud Radar (WCR)	Reflectivity factor (Z_e) and Doppler velocity	100-10000 meters/~15 meters	UWKA
Wyoming Cloud Lidar (WCL)	Backscattering coefficient and linear depolarization ratio	+30 meters/3.75 meters	UWKA

Table 2. Information for cross-barrier flight leg averages

RF#	Case Type	Altitude (m)	# Legs	Altitude (m)	# Legs	Altitude (m)	# Legs
1	Hybrid	4550	4	5330	5	6040	6
3	Wave	4500	7	--	--	6140	5
5	Wave	4235	6	4310	2	--	--
9	Hybrid	4300	3	5150	3	6020	4
12	Convective	4300	5	4850	3	5160	3
26	Convective	4550	3	5120	4	--	--
28	Convective	4510	3	5720	5	--	--